Impacts of overtopping waves on buildings on coastal dikes

Chen, Xuexue

DOI
10.4233/uuid:e899b6e4-fcbe-4e05-b01f-116901eabfef

Publication date
2016

Document Version
Final published version

Citation (APA)
Chen, X. (2016). *Impacts of overtopping waves on buildings on coastal dikes*. [Dissertation (TU Delft), Delft University of Technology]. https://doi.org/10.4233/uuid:e899b6e4-fcbe-4e05-b01f-116901eabfef

IMPACTS OF OVERTOPPING WAVES ON BUILDINGS ON COASTAL DIKES

IMPACTS OF OVERTOPPING WAVES ON BUILDINGS ON COASTAL DIKES

Proefschrift

ter verkrijging van de graad van doctor
aan de Technische Universiteit Delft,
op gezag van de Rector Magnificus prof. ir. K.C.A.M. Luyben,
voorzitter van het College voor Promoties,
in het openbaar te verdedigen op woensdag 2 november 2016 om 10:00 uur

door

Xuexue CHEN

civiel ingenieur, Technische Universiteit Delft
geboren te Jinzhou, China

Dit proefschrift is goedgekeurd door de

promotor: Prof. dr. ir. W.S.J. Uijttewaal
promotor: Prof. dr. ir. S.N. Jonkman
copromotor: Dr. ir. B. Hofland

Samenstelling promotiecommissie:

Rector Magnificus,	voorzitter
Prof. dr. ir. W.S.J. Uijttewaal,	Technische Universiteit Delft, promotor
Prof. dr. ir. S.N. Jonkman,	Technische Universiteit Delft, promotor
Dr. ir. B. Hofland,	Technische Universiteit Delft, copromotor
Onafhankelijke leden:	
Prof. dr. I. Nistor,	University of Ottawa
Prof. dr. ir. P. Troch,	Universiteit Gent
Prof. dr. F. Mostaert,	Universiteit Hasselt/Flanders Hydraulics Research
Prof. dr. ir. M. Kok,	Technische Universiteit Delft
Prof. dr. ir. S.G.J. Aarninkhof,	Technische Universiteit Delft, reservelid

Dr. Tomohiro Suzuki and Dr. Corrado Altomare hebben in belangrijke mate aan de totstandkoming van het proefschrift bijgedragen.

Printed by: Gildeprint

Cover image: Katsushika Hokusai (1829–1832)

Cover design: Xuexue Chen

ISBN 978-94-6186-738-4

An electronic version of this dissertation is available at
http://repository.tudelft.nl/.

CONTENTS

SUMMARY

Due to climate change, sea level rise, increasing frequency and intensity of storms, and growing population in low-lying coastal regions, the risk of flooding is expected to increase. Owing to these developments, maintenance and adaption of the existing coastal flood defence is often required. To meet this dilemma, the concept of multifunctional flood defence (MFFDs) is promoted. It aims at integrating urban functions with flood defence structures. Considering the threat from possible wave overtopping to the buildings on the top of coastal dikes in the low-lying highly populated regions like Belgium, this thesis focuses on advancing the understanding of the hydraulic impact of wave overtopping and developing a practical approach to assess the vulnerability of coastal buildings on the dike. The results can be used for the design and assessment of coastal MFFDs. Two-dimensional physical model tests were used to study wave overtopping and overtopping wave impact for the situation of coastal dikes where a shallow foreshore affects the wave overtopping.

In Chapter 2, the impact mechanism of overtopping waves was studied. An overtopping wave is characterized as a turbulent bore. The impact process and impact mechanisms of a single overtopping wave on a vertical wall were examined by detailed measurement of force distribution and overtopping wave velocity field. A double-peaked force was recognized in the impact time series including a dynamic impact peak and a quasi-static force peak. The latter was found similar to that of a tsunami impact. Due to the presence of the vertical wall on the dike and the interaction motions between multiple overtopping waves, the eventual overtopping wave impact was found to be different than the single impact. "Collision" and "catch-up" interaction patterns may alter the impact mechanisms of the overtopping waves, when compared to regular wave impacts. Impulsive impact with a violent dynamic pressure can be expected at a high elevation of the vertical wall, which might be governed by the collision type interaction.

In Chapter 3, an empirical formula for a single overtopping wave impact load was developed. To characterize the overtopping wave impact load on a vertical wall, a new descriptor (overtopping momentum flux) to describe the impact loads empirically was proposed. To validate the proposed empirical function, a series of physical scale model tests were conducted with regular waves. In these experiments, the overtopping wave loads on a vertical wall were measured at different locations on a dike. A correction coefficient for the wall effect on the initial flow depth, and an empirical initial flow depth coefficient for an overtopping wave were determined. These empirical coefficients allowed for an interpretation of the overtopping process of an incident wave from dike toe up to the front of the wall on the dike.

In Chapter 4, statistical analysis was carried out for the prediction of the maximum overtopping wave impact within a known storm peak. In order to extend the knowledge of the overtopping wave impact loads and provide a predictive method practically, a series of physical model experiments with irregular waves were conducted. The results

show that the Generalized Pareto (GP) distribution gives a suitable fit among commonly used distributions for the extreme overtopping forces. Three parameters of the GP distribution (i.e., threshold parameter, scale parameter and shape parameter), are empirically determined by the incident wave conditions at the toe and the dike freeboard and the dike crest width. Then a new 7-step procedure is suggested as a simple tool for predicting the maximum force occurring during a certain storm peak, which shows an overall satisfactory performance.

In Chapter 5, the vulnerability of buildings on coastal dikes caused by overtopping wave impacts was assessed. A method is developed to quantify the vulnerability of masonry buildings on a coastal dike exposed to wave overtopping. The impact load from overtopping waves is assumed to be an accidental loading. The partial factor method as described in the Eurocode 6 is applied for both the load on and the resistance or strength of a structure. Results from a case study in Belgium show that masonry buildings located at 10-15 meters away from the seafront would suffer from localized damage under a 1000 year storm due to breaking windows, and would collapse under a 10,000 year storm. The method can be used to assess the existing buildings on coastal dikes, and design new buildings.

This thesis presents a series of findings on the propagation of overtopping waves on the dike, characteristics of the resulting impact load on a vertical wall. The proposed practical approach can be used to estimate the occurrence of the maximum impact load of overtopping waves of a given storm peak. For low-lying coastal regions, it can serve as the input for the further vulnerability assessment of the existing and newly designed buildings on the dike which are exposed to the impact of overtopping waves. It is recommended to extend the current study of the overtopping wave impact on the wall with other failure mechanisms, such as the erosion and breaching of the dike.

SAMENVATTING

Door klimaatverandering, zeespiegelstijging, een toename in de frequentie en intensiteit van stormen, en de bevolkingsgroei in laaggelegen kustgebieden is het de verwachting dat het overstromingsrisico zal toenemen. Deze ontwikkelingen zorgen ervoor dat onderhoud en aanpassingen aan bestaande kustverdedigingskunstwerken noodzakelijk zijn. Om aan dit probleem tegemoet te komen wordt het concept van een multifunctionele vloedkering voorgesteld. Dit concept omvat de integratie van stedelijke functies met de waterkerende functie. Gegeven de dreiging van golfoverslag voor gebouwen op de kruin van een zeedijk in laaggelegen dichtbevolkte gebieden stelt dit onderzoek zich ten doel om ons begrip van de hydraulische impact van overslaande golven te verbeteren en om een praktische aanpak te ontwikkelen om de kwetsbaarheid van dergelijke gebouwen te kunnen beoordelen. De resultaten kunnen worden gebruikt voor het ontwerp en de beoordeling van multifunctionele vloedkeringen. In dit proefschrift is met behulp van tweedimensionale schaalproeven zowel de golfoverslag zelf als de impact van deze golven bestudeerd voor de situatie waarin een ondiepe vooroever de golfoverslag over de zeedijk beïnvloedt.

Hoofdstuk 2 behandelt de impact mechanismes van overslaande golven. Dergelijke golven kunnen worden gekarakteriseerd als een turbulente watersprong. Het impactproces en mechanisme van een enkele overslaande golf tegen een verticale muur werden bestudeerd aan de hand van gedetailleerde metingen van het snelheidsveld van de overslaande golf en de krachtsverdeling op de muur. Het meetsignaal toonde een dubbel gepiekte kracht: een dynamische impact piek en een quasi-statische krachtspiek. Laatstgenoemde toont sterke overeenkomsten met de impact van een tsunami. Door de aanwezigheid van de reflecterende verticale wand en de interacties tussen meerdere overslaande golven was de impact van deze golven verschillend ten opzichte van de impact van een enkele golf. In vergelijk met regelmatige golfklappen wordt het impact mechanisme van overslaande golven beïnvloed door zogenaamde “collision” en “catch-up” interactie patronen. Impulsieve impacts met intense dynamische drukken kunnen worden verwacht ter plaatse van de bovenkant van de verticale muur, welke kunnen worden gedomineerd door het collision type interactie.

In hoofdstuk 3 is er een empirische formule ontwikkeld voor de belasting van een enkele overslaande golf. Om de belasting van de overslaande golf te karakteriseren is er een nieuwe descriptor (de overslag momentum flux) voorgesteld om de impact belasting empirisch te beschrijven. Om de voorgestelde empirische formule te valideren is er een serie aan fysische modelproeven met regelmatige golven uitgevoerd. In deze experimenten werd de belasting van overslaande golven op een verticale wand gemeten voor verschillende posities op de dijk.

In hoofdstuk 4 zijn statistische analyses uitgevoerd om de maximale impact van een overslaande golf te bepalen binnen een vooraf bekende stormpiek. Om onze kennis over de golfoverslagbelasting te vergroten en om een praktische voorspellingsmethode te le-

veren is er een serie van schaalproeven met onregelmatige golven uitgevoerd. De resultaten tonen aan dat de gegeneraliseerde Pareto verdeling de meest geschikte overeenkomst geeft in vergelijking met andere verdelingen die veel gebruikt worden voor extreme overslagkrachten. Drie parameters van de pareto distributie, de drempelwaarde, de schaal parameter en de vorm parameter, zijn empirisch vastgesteld aan de hand van de inkomende golfcondities aan de voet van de dijk, de waakhoogte, en de kruinbreedte. Vervolgens is er een 7-staps procedure voorgesteld als een simpele techniek om de maximale kracht tijdens een willekeurige storm te kunnen voorspellen. Deze procedure blijkt toereikend om de maximale kracht te voorspellen.

In hoofstuk 5 is vervolgens de kwetsbaarheid van gebouwen op een dijk voor overslaande golven bepaald. Er is een methode ontwikkeld om de kwetsbaarheid van gemetselde gebouwen te bepalen. Hierin is aangenomen dat de overslaande golven een toevallige belasting zijn. De partiële factor methode, zoals beschreven in de Eurocode 6, is toegepast voor zowel de belasting op het gebouw, als de weerstand of sterkte van het gebouw. De resultaten van een casus in België tonen aan dat gemetselde gebouwen die zich binnen 10-15 meter van de kust bevinden lokale schade zullen ondervinden voor een 1000 jaar storm, door brekende ramen, en zullen instorten voor een 10.000 jaar storm. De methode kan worden toegepast voor de toetsing van bestaande gebouwen, en in het ontwerp van nieuwe gebouwen.

Dit proefschrift presenteert een reeks aan resultaten over de propagatie van overslaande golven op een dijk, en karakteristieken van de resulterende belasting op een verticale muur. De voorgestelde praktische methode kan worden toegepast om de maximale belasting van overslaande golven voor een gegeven storm te bepalen. Het kan als invoer dienen voor een verdere kwetsbaarheidstoetsing van bestaande en nieuw te ontwerpen gebouwen op een dijk welke blootgesteld worden aan overslaande golven. Het is aangeraden om de huidige studie uit te breiden naar andere faalmechanismen van een muur ten tijde van overslaande golven, zoals erosie, ontgronding en het doorbreken van een dijk.

1

INTRODUCTION

1

1.1. COASTAL FLOODING AND OVERTOPPING HAZARDS

Human settlement has a long history on the coast, especially in the low-lying areas. These regions take up about 2% of the world's land, but accommodate about 13% of the urban population (McGranahan et al., 2007). The densely populated coastal regions are vulnerable to coastal flooding. However, these areas are still becoming increasingly attractive for economic, environmental, and social development (Aerts and Botzen, 2011). Particularly in the developed environments, urbanization near the coast results in the presence of buildings and infrastructures quite close to coastal defences or even on their crests.

Coastal flooding includes large scale direct inundation, overtopping, and breaching of a flood defence. Direct inundation may be caused by the inundation of storm surges. Overtopping occurs when the wave height exceeds the crest of a flood defence. When assessing the flood risk for the highly developed coastal sites, coastal inundation caused by high water levels and breaching of the flood defence are the main concerns (Allsop et al., 2008). Nevertheless, the hazard of overtopping will be important for the design of property on the coast (Allsop et al., 2008; Verwaest et al., 2010). Allsop et al. (2008) pointed out that the direct hazard from overtopping on coastal buildings and humans nearby is often being ignored. Thus more attention could be paid. Wave overtopping and its resulting hazards are addressed in this thesis.

One of the main overtopping hazards is the damage to waterfornt properties. The buildings and infrastructures located close to the flood defence along the low-lying developed coasts can be frequently exposed to wave overtopping. In the UK, steep or vertical seawalls are frequently used as flood defence structures. The incident waves break at the face of the seawall, resulting in splash overtopping. Afterwards, the overtopped waves may directly impact on the properties behind the seawall. These properties are normally designed and constructed for residential or commercial purpose without the consideration of the potential impact load from overtopping. Earlier site model tests by HR Wallingford suggested that the overtopping load on the facades of buildings is beyond the structural design load in the UK (Allsop et al., 2008). Thus a failure of the external wall due to overtopping is expected. Fig. 1.1 shows some examples of the damages of rail ways, roads and houses caused by overtopping during the winter storm in the year 2015 in the UK. Another main overtopping hazard is the direct injury and death of people. Allsop et al. (2008) stated that on average 2-5 people are killed on the seawalls and similar structures each year in the UK through overtopping waves. Fig.1.2 shows a moment that a family is soaked by overtopping waves in Cornwall, England. Direct injury and death of people caused by overtopping waves could be avoided if they were encouraged to stay away from the defence structure. However, people often tend to ignore the overtopping risk when they stand too close to the defence. Based on the reports of the direct damage or loss of life caused by wave overtopping, overtopping effect on the steep or seawall has been attracting more attention. However, little is known of wave overtopping effects on coastal dikes with (gentle) slopes.

Figure 1.1: Direct hazards from wave overtopping to coastal infrastructures and buildings in UK, 2015 (source:): (a) Waves undermine the main London to Cornwall rail line, used by thousands of travelers; (b) The road in Amroth destroyed by the overtopping wave impact; (c) Blackpool main promenade under flood water following high tide and a tidal surge as severe gale force winds hit many parts of the UK (d) The sea wall at Dawlish, Devon, has been broken by ferocious waves while a Devon ice cream stand has been damaged and swept away.

Figure 1.2: A man and woman with two young children drenched in water after being blasted by overtopping waves at Mullion Cove (Duell and Thomas, 2014)

.

1.2. MULTIFUNCTIONAL FLOOD DEFENCES

Considering the climate change, sea level rise, the increasing flood frequency and severity, and the growing population exposed to flooding, the risk of flooding is expected to

increase (Nicholls, 2004). Therefore, the management strategies of flood defences need to be adapted to the upcoming changes. The adaption of the existing flood defences requires the widening of the defence structure and elevation of the defence crest, which requires space. However, the competing needs of housing, commerce, transportation, and agriculture have to fit in the scarce, developed coastal space as well (Anvarifara et al., 2016). Meanwhile, the existing living environment and the quality of the coastal landscape have to be preserved (Ligtvoet et al., 2009). Therefore, there is a conflict between the flood defence adaption and the urban development needs. In order to cope with this dilemma, a new solution is required. One strategy is to integrate urban functions into the flood defences. so that multifunctional flood defences (MFFDs) will be developed (van Loon-Steensma and Vellinga, 2014). MFFDs are flood defense structures that also provides secondary functions. Examples of these functions are transport, housing, shopping, agriculture, nature, recreation and so on. The promotion of MFFDs can contribute to the sufficient safety of a flood defence system by enhancing the quality of the living environment of the urbanization with a lower cost of land use (Stalenberg, 2010).

In 2011, a research program on sustainable design of MFFDs was set up. The general objective of the MFFDs program is to gain the scientific knowledge necessary to meet the requirements from the upcoming challenges for flood mitigation in urban areas brought by economic and climate changes. As one of the projects of the MFFDs program, the current study is associated with the task of hydraulic impact of overtopping waves on a multifunctional dike. Other projects can be found in the same MFFD program: http://www.flooddefences.nl.

In the low-lying coastal countries like The Netherlands, Belgium and elsewhere, the configuration shown in Fig. 1.3 (top panel) is commonly seen. The crest of a coastal dike is often used as a promenade or building frontage[1]. Thus, a building placed on the dike is selected as a specific case of a multifunctional dike. Considering the location of the building, the physical damage or failure of buildings caused by the overtopping waves would not only dependent on the properties of buildings and overtopping wave characteristics, but also the state of the dike.

Due to the potential impact from wave overtopping, three types of failures of the building are recognized with inclusion of the physical damage of the dike itself (mode A), foundation of buildings (mode B) and structural failure of building components (mode C). If no overtopping occurs, the main damage is scouring of the toe (A1) and the wave impact on the dike slope (A2). These damage patterns may be indirectly related to the failure of buildings. When overtopping occurs, two consequences of overtopping are expected, including infiltration and the propagation wave on the dike. The former may result in the settlement of the subsoil under the foundation (B1), which may undermine the stability of the building (C1). Based on the fact that most of the buildings on the dike are supported by pile foundations, the probability of this concern is comparably low. While for the latter overtopping propagation, heavy erosion of the dike crest (A3) may cause the loss of the stability of the foundation (B2). When a large overtopping wave strikes on a building, the consequence of this impact includes: failure of non-structural component (C2) or structural failure of the building (C3), and scour of the corner of the building (A4). When the overtopping water is flowing over the dike through the space

[1] Frontage is the extent of the front of a building along a street, river, etc

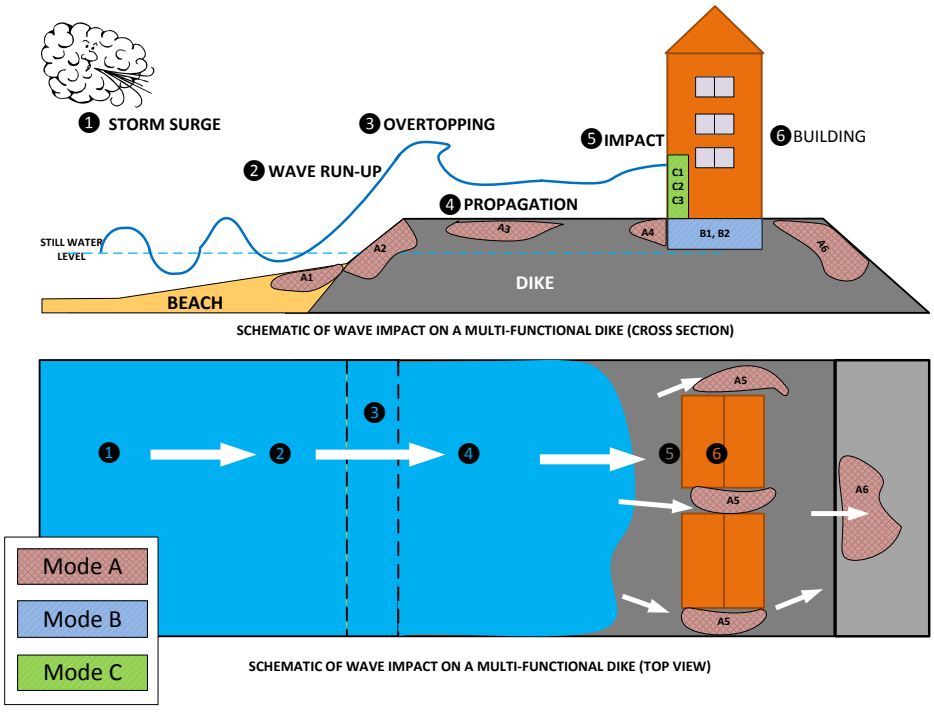

Figure 1.3: Schematic of the overtopping wave impact on the buildings and dikes.

between buildings, it could lead to scour around the building (A5), and erosion of the inner slope of the dike (A6).

Overtopping induced erosion (scour) is one of the basic failure mechanisms of dike (e.g., Mode A), but few studies investigated the failure of a dike caused by the overtopping impact on large structures on the dike. These mode B (foundation failing) and C (building failing) may lead to the dike failure as well. Due to the lack of relevant records of the direct damage from wave overtopping on buildings which are on the dike, the users and owners of the properties may be unaware of the possible effects of wave overtopping. Thus, to evaluate the potential damage of buildings on the dike caused by wave overtopping is necessary for the design and evaluation of a multifunctional dike. The current research is focused on the overtopping wave impact on the building (C3) and its non-structural element (C2).

1.3. PROBLEM STATEMENT AND RESEARCH QUESTIONS

There is plenty of literature on wave overtopping of a dike (e.g., Van der Meer and Janssen, 1995; Pullen et al., 2007; Schüttrumpf, 2001; Van Gent, 2002; Schüttrumpf and Oumeraci, 2005; Van der Meer et al., 2010; Van Doorslaer et al., 2015), but few studies address the overtopping wave loads on buildings on the dike and its consequence. Therefore, it is not only required to understand the overtopping wave characteristics and their impact

mechanisms, but also the failure mechanisms and potential damage of buildings on the dike due to overtopping wave actions. Specific research topics and questions that follow from this observation are explored in this thesis, and are briefly discussed below.

(1) Impact process and mechanism of overtopping waves
The most relevant research about the wave impact on coastal buildings placed on the seaside has been done for tsunamis (e.g., Nistor et al., 2009) and storm surges (e.g., Ramsden, 1996; Hatzikyriakou et al., 2015). Although there is a certain similarity between a single overtopping wave and a tsunami wave, there is limited understanding of the interactions of the overtopping waves due to their stochastic nature, and the role of the interaction on the resulting overtopping wave impact. To address these questions, a series of physical model experiments is needed with special interests in the overtopping wave interactions and wave impact processes. Based on the physical model experiments, the impact force distribution and the velocity field of overtopping waves addressing the aforementioned concerns will be investigated.

(2) Impact force characterization
Recent research shows that overtopping caused by the waves with long period is expected to lead to extreme impact on the buildings on coastal sites with a shallow foreshore in the front (e,g., Suzuki et al., 2012; Shimozono et al., 2015; Roeber and Bricker, 2015). To deepen the existing understanding and characterize the overtopping wave impact induced by long wave period waves in a shallow water environment as occurring in Belgium and The Netherlands, physical model experiments can provide the necessary data when performed with regular waves with a long period. These can subsequently be used to develop empirical formulas for the overtopping wave impact force as a function of wave height, wave period and dike geometry parameters.

(3) Prediction of extreme overtopping wave forces during a known storm peak
Wave overtopping can be interpreted as a stochastic process. Thus a statistical description of forces is needed. A series of physical model experiments with irregular waves can provide the data to make this feasible. In order to extend the knowledge of the overtopping wave impact loads and provide a predictive method, statistical analysis for the occurrence of maximum overtopping wave impact within a known storm peak needs to be carried out.

(4) Vulnerability of buildings on the coastal dike
Since the Belgian coast is characterized by a shallow foreshore, overtopping waves can lead to significant impact to the buildings on coastal dikes (Verwaest et al., 2010; Suzuki et al., 2012). Based on historical flood events, structural and non-structural failures of buildings under different types of hydraulic load have been studied by several researchers (e.g., Kelman and Spence, 2004; Nistor et al., 2009; Matsutomi and Okamoto, 2010; Pistrika and Jonkman, 2010; Chock et al., 2011), but not for the typical configuration considered in this study (Fig. 1.3). In order to assess the vulnerability of buildings on coastal dikes, a practical method for this

evaluation especially concerning the overtopping wave impacts with the existing design code is needed.

1.4. OUTLINE

Following the above objectives, this thesis is organized as follows. Chapter 2 introduces the wave overtopping process and the impact mechanisms of overtopping waves on a vertical wall. An empirical formula for the impact loads as a function of the properties of the incoming regular, long waves and dike geometry characteristics is developed in Chapter 3. A method to estimate the maximum forces on the wall during a known storm peak is presented in Chapter 4. Subsequently, a method for evaluating the vulnerability of buildings on coastal dikes exposure to wave overtopping is developed, and is applied to a Belgian case in Chapter 5. In Chapter 6, conclusions and recommendations are presented. More schematically, the thesis is organized as follows:

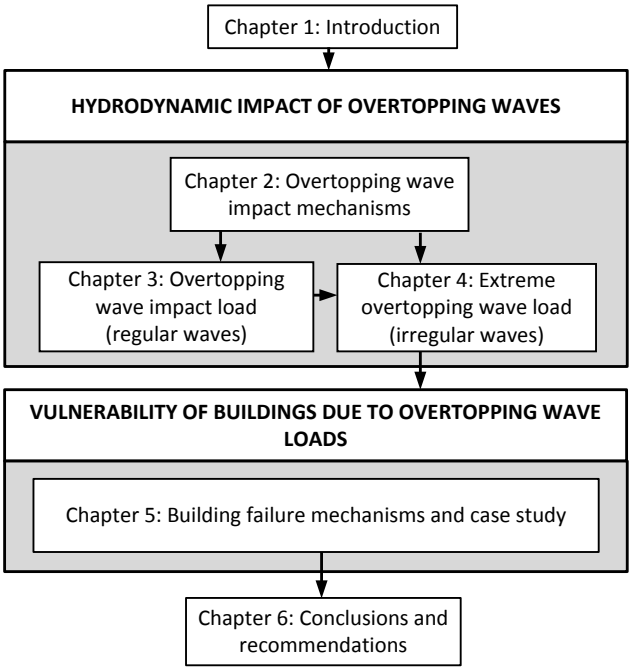

Figure 1.4: Structure of the thesis

2

IMPACT MECHANISMS OF OVERTOPPING WAVES

In this chapter, the impact mechanism of overtopping waves on a vertical wall is investigated. A double-peaked force can be recognized in the time series of an overtopping wave. Four stages were summarized for the whole overtopping wave impact process. “Collision” and “catch-up” interaction patterns may alter the impact mechanisms of the overtopping waves on the wall, when compared to regular wave impacts. Impulsive impact with a violent dynamic pressure can be expected at a high elevation of the vertical wall, which might be governed by the “collision” type interaction. “Catch-up" near the wall can also induce impulsive impact on the wall, but close to the bottom part.

Parts of this chapter has been published in: Chen, X., Hofland, B., Altomare, C., Uijttewaal, W. (2014). Overtopping flow impact on a vertical wall on a dike crest. In proc. Int. Conf. on Coastal Engineering, ICCE (Vol. 1, p. structures.4).

2.1. INTRODUCTION

A wave that overtops a coastal dike will experience several processes including wave propagation in deep water, shoaling in shallow water, breaking in the surf zone, run-up along the seaward slope of the dike, propagation along the dike crest, and overtopping. When the overtopping wave impacts the vertical structure, the wave will be reflected back seaward. The overtopped wave on the dike crest will be referred to as overtopping wave in this thesis. Cox and Machemehl (1986) stated that when a wave overtops the seaward slope of dike, it could be considered as a breaking wave propagating across the flat seabed in the form of a spilling breaker. With spilling, the breaker's turbulence is qualitatively similar to the processes of a bore (Battjes, 1974). Therefore, the propagation and energy dissipation process of the overtopping wave on the dike crest can be related to those of a bore.

2.2. LITERATURE

In this section, a literature review about the impact of waves in deep water and of bores on vertical structures are presented.

2.2.1. DEEP-WATER WAVE IMPACT ON STRUCTURES

A wave impact on a vertical structure in the sea depends on the wave breaker shape, which can be identified by wave and geometry parameters (Oumeraci et al., 1993). A typical force history of a wave impact consisting of two peaks, the first one is dynamic force peak F_{dy} and the second one is quasi-static force peak F_{qs+}. Four types of breaking waves include: quasi-standing, slightly breaking, impact or breaking, and broken wave, which are classified by their typical force history showing their characteristics (Kortenhaus and Oumeraci, 1998).

For a quasi-standing wave impact in front of vertical walls, the incident wave does not break. The typical force history does not show significant two-peak shape but slowly varying over time, see Fig. 2.1(a). This impact is induced by a non-breaking wave which is not relevant to the overtopping wave. Thus, it is not treated herein.

For a slightly breaking wave impact, the incident wave starts to break in front of the vertical wall or just at the wall. The first peak in the force time series is higher than the second quasi-static peak with a ratio between 1 to 2.5 (Kortenhaus and Oumeraci, 1998), see Fig. 2.1(b).

For a breaking wave impact, the incident wave just breaks in front of the wall, generally induced by the berm in front of the structure (Kortenhaus and Oumeraci, 1998). The force history of this impact wave is characterized by a clearly sharp dynamic peak followed by the quasi-static peak with a longer duration. This two-peak shape of force history is also well-known as a "church-roof", see Fig. 2.1(c).

A broken wave impact occurs when the breaking point of the incident wave is far from the wall. It is a general case of a wide berm or extremely shallow water presented in front of the wall. The force history is characterized by high frequency oscillations due to a turbulent broken wave front. The order of magnitude of the force is the same as for slightly breaking waves (Kortenhaus and Oumeraci, 1998), see Fig. 2.1(d). The broken wave is similar to a bore. This type impact will be reviewed in the Section. 2.2.2.

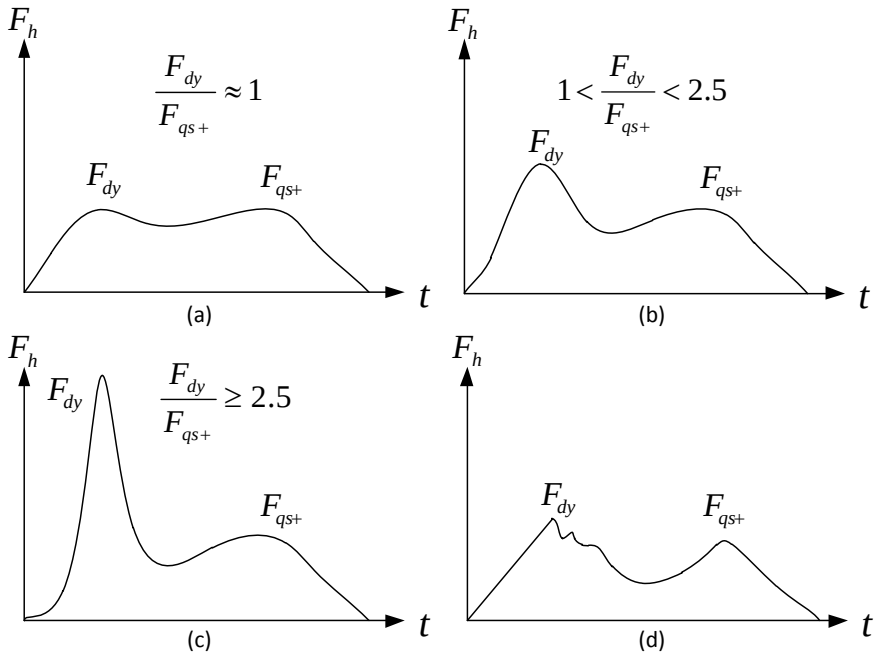

Figure 2.1: Force histories various types of wave impact on a vertical wall. (a) quasi-standing wave; (b) slightly breaking wave; (c) breaking wave impact; (d) broken wave. Adapted from Oumeraci et al. (1993) and Kortenhaus and Oumeraci (1998).

Among the four types of wave impacts, the breaking wave will provide a violent impingement, which can lead to damage or collapse of coastal structures (Lugni et al., 2006). Recent field and laboratory observations suggest that this type of violent impact is also expected to occur when a wide berm or extremely shallow water is present in front of the wall (Nørgaard and Andersen, 2014). Thus it is necessary to treat this type of impact in this study. The qualitative and quantitative experimental determinations of the breaking wave impact load on vertical structures has been examined widely in the past decades (e.g., Chan and Melville, 1988; Oumeraci et al., 1993, 2001; Cuomo et al., 2010b; Kisacik et al., 2012). However, due to the scale and model effects caused by laboratory experiments, the use of the empirical results for predicting impact load is restricted.

Cooker and Peregrine (1990, 1995) provided a mathematical model by using the concept of pressure-impulse, as shown in Fig. 2.2 including a schematic impact pressure history (a) and boundary values of an ideal breaking wave (b). The pressure-impulse (P_z) close to the impact zone depends on the normal component of the impact velocity U_0. The impact velocity is assumed uniformly distributed along the impact zone. The distance from the sea bed to the wave crest in front of the wall is H. The wave impact zone is a fraction μ of this height. The fluid domain has been idealized to a rectangle with free surfaces at the upper and left hand edges ($y = 0$, $X = H$). The other bound-

aries are the bed ($y = -H$), the lower part of the wall ($-H < y < -\mu H$) and the impact zone ($-\mu H < y < 0$). By using the mentioned boundary values and Cooker and Peregrine (1995)'s solution, the pressure-impulse of the breaking wave impact can be calculated. Then the impact pressure p_{pk} at the location y can be simply expressed as:

$$p_{pk} = \frac{2P_z}{\Delta t} \tag{2.1}$$

where P_z is the pressure-impulse and Δt is the impact duration. Afterwards, the pressure distribution along the wall ($-H < y < 0$) can be obtained.

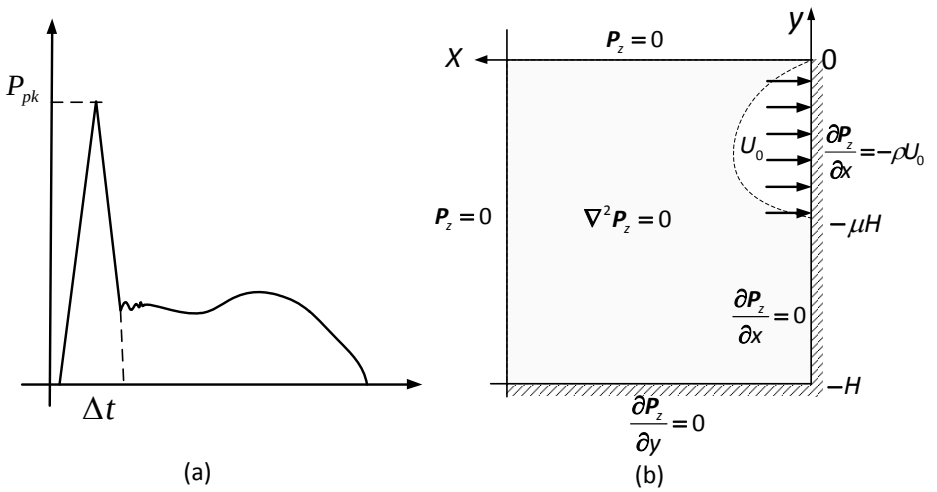

Figure 2.2: (a) Schematic sketch of impact pressure time history; (b) The impact of a rectangle of fluid on a vertical wall at $X = 0$. The impact zone is from the top free surface ($y = 0$) till the part-way down the wall (μH). The back free surface of the wave is at $X = H$ with $P_z = 0$, adapted from (Cooker and Peregrine, 1995).

2.2.2. BORE IMPACT

When a bore approaches a vertical wall, its impact process includes three stages, as shown in Fig. 2.3:

(a) The bore approaches the wall with a constant thickness and front velocity;

(b) The bore front suddenly changes its direction due to the vertical wall and is deflected upwards till the maximum point;

(c) After the wave run-up to the maximum point, the deflected column of water mass falls back on the water and a reflected bore forms.

Some pioneering analytical and experimental research of the impact of a bore on a vertical wall can be dated back to Stoker (1957), Cumberbatch (1960), Fukui (1963) and Cross (1967). Stoker (1957) investigated the reflection of a bore from a rigid vertical wall and gave an analytical equation for the force exerted on the wall (Nouri et al., 2010). Cumberbatch (1960) developed a mathematical model of a two-dimensional inviscid water

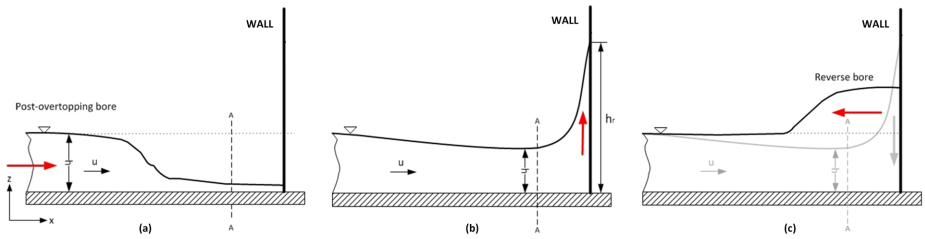

Figure 2.3: Sketch of overtopping bore striking a wall, adapted from Cross (1967) and Robertson (2011)

wedge impact on a vertical wall. The author assumed that the wedge keeps a constant shape and velocity before its impingement. The impact horizontal force peak per unit length F_h is calculated as:

$$F_h = C_F \rho h u^2 b, \tag{2.2}$$

where C_F is the force coefficient, ρ is the fluid density, h is the water level at the wall location and u is the incoming flow velocity. All the parameters used in Eq. (2.2) are defined as if the wall was not present. The meaning of these parameters can be found in Fig.2.3. Because gravity is neglected, Eq. (2.2) can only be used to model the process just after the impact and before the gravitational acceleration starts to influence the flow along the wall (Arnason, 2005). Cross (1967) improved Cumberbatch (1960)'s model by adding the gravity term into Eq. (2.2), which yields:

$$F_h = \frac{1}{2}\rho g h^2 + C_F \rho h u^2. \tag{2.3}$$

The coefficient C_F is empirically determined as (Cross, 1967):

$$C_F = (\tan\theta_0)^{1.2} + 1, \tag{2.4}$$

where θ_0 is the incident water wedge angle. Ramsden (1996) investigated the impact of solitary waves, bores and surges on a vertical wall. The author observed that the measured maximum force F_h is less than that computed by using the measured maximum run-up height, h_r (see Fig. 2.3(b)). Robertson (2011) proposed a new formula for F_h on the vertical wall caused by tsunami bores with different magnitudes in large scale experiments.

2.2.3. OVERTOPPING WAVE IMPACT

Since a single overtopping wave can be seen as a bore, the impact of an overtopping wave on a vertical structure resembles Cross (1967)'s description, see Fig. 2.3. The process of bore impact can give a basic impression of overtopping wave impact on a wall. Chen et al. (2012), De Rouck et al. (2012) and Ramachandran et al. (2012) reported their laboratory work of overtopping wave loads on vertical structures on dikes by using physical models with different scales. The common findings of these works suggested that the observed impact force of an overtopping wave has a double-peak time series including

a dynamic peak and a quasi-static peak. This shape is similar to that of the "church-roof" wave impact force on caissons and composite structures in deep water proposed by Oumeraci et al. (1993), but without significant difference on the magnitudes of the two peaks. Based on the literature review, there is limited work related to the impact load of overtopping waves on a vertical wall. Also the initial impact will give large pressures at the based of the wall.

There are some other studies about wave loads on crown walls of monolithic rubble mound breakwaters (e.g., Hamilton and Hall, 1992; Pedersen, 1996; Martin et al., 1999; Nørgaard and Andersen, 2014). Nørgaard and Andersen (2014) provided a tool for predicting the impulsive wave loads on crown walls.

Overtopping wave impact may initiate scour in front of the wall. During the impact process of an overtopping wave on the wall, a downward vertical jet may be generated. The impingement of the vertical jet may destruct the top layer of the dike (e.g., pavement) in front of the wall. When dynamic pressures enter the cracks of the top layer, the development of the pressure inside quickly lift up the top layer and the underneath soil. There is limited studies on the scour of dike due to the wave impact on a wall. But the destruction of concrete slabs caused by water jets is similar to the present concern. Fiorotto and Rinaldo (1992) investigated the plunging jet impact on concrete slabs (Bollaert and Schleiss, 2005) and stated that the uplift forces under the slabs are completely determined by the pressures at the concrete crack entrances. They suggested a design criterion for the thickness of the slab to avoid the destruction from the impact:

$$s = \Omega \cdot C_p \cdot \frac{V_j^2}{2g} \cdot \frac{\gamma}{\gamma_s - \gamma}. \tag{2.5}$$

where s is the equivalent slab thickness in [m]; Ω is dimensionless reduction factor [-]; C_p is pressure coefficient [-], which equals to $\Delta p_{max}/(\gamma \cdot V_j^2/2g)$; Δp_{max} is the maximum pressure difference [N/m^2]; V_j is the vertical jet velocity, γ and γ_s are the specific weight of water and slab. If Ω, C_p and V_j are determined from the overtopping wave impact, then the limit state of the destruction of top layer of the dike or pavements can be set as the initiation of scour.

The objective of this chapter is to examine the impact mechanism of overtopping waves by detailed measurement of the interaction process between the overtopping wave and a vertical wall. This understanding will help to develop empirical formulas for the overtopping wave impact load in Chapters 3 and 4. The initiation of scour due to overtopping wave impacts is not further considered in this thesis.

This chapter is organized as follows. The experimental set-up is described in Section 2.3. Afterwards, the impact process and mechanisms of the individual overtopping wave and multiple overtopping waves are presented in Section 2.4 and Section 2.5 respectively. Finally a conclusion is given in Section 2.6.

2.3. EXPERIMENT SET-UP

2.3.1. FACILITIES AND WALL MODEL

Physical model tests were performed in a 4 m wide, 1.4 m deep and 70 m long wave flume at Flanders Hydraulic Research, Antwerp, Belgium. A piston-type wave generator with a stroke length of 0.6 m was used to generate monochromatic, multi-chromatic and random waves. The wave flume was split into four sections (about 1 m for each) of which two were used for passive wave absorption, as shown in Figure 2.4. The dike model height was 0.1 m with the seaward slope 1:3. The foreshore slope was 1:35. A wall model was placed on the top of a model dike in one of the sections. The wall was consisted of two parts: an aluminium force-measuring portion and a fixed wall (PVC board). The aluminium plate was mounted to two load cells of model series Tedea-Huntleigh 614, which were used to determine the total overtopping wave force with a sampling rate of 1000 Hz. Next to the force-measuring portion, four point pressure sensors were mounted flush in the face of the wall, see Figure 2.5. They were sampled at a rate of 1000 Hz in order to study in the evolution of local pressures.

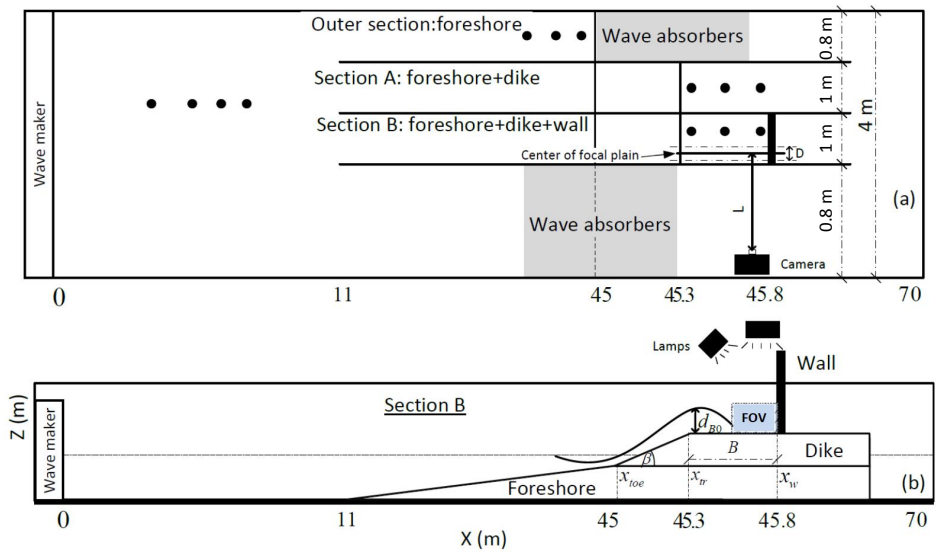

Figure 2.4: Wave flume in Flanders Hydraulic Research (Antwerp, Belgium): (a) a top view of the flume (not in scale), (b) the respective section B to measure impact forces and velocity field.

2.3.2. BUBBLE IMAGE VELOCIMETRY

Overtopping wave features (e.g., overtopping flow layer thickness and velocity field) are believed to be directly related to the wave impact. Due to the breaking of waves on the foreshore or dike slopes, the overtopped waves on the dike are highly aerated and turbulent. This complexity limits the accuracy of the measurement of the overtopping wave (De Rouck et al., 2012). Thus, choosing a proper technique is necessary.

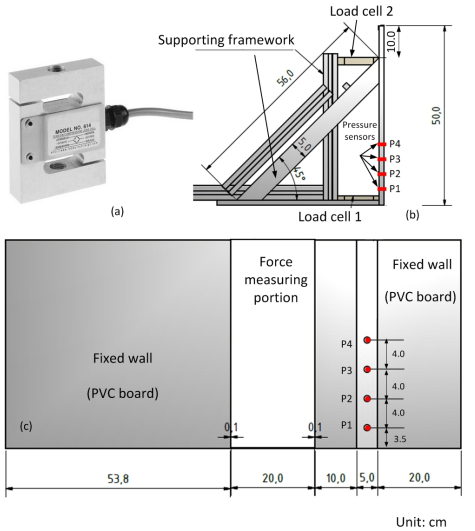

Figure 2.5: Wall model and force measuring system including (a) load cell, (b) positioning of load cells and support frame, and (c) front view of wall model and locations of pressure sensors

Bubble Image Velocimetry (BIV) as used by Ryu et al. (2005) was applied to measure the overtopping wave velocity field. This technique has been proven sufficient to measure turbulent flow (e.g., Ryu et al., 2007; Pedrozo-Acuña et al., 2011; Lin et al., 2012; Ariyarathne et al., 2012; Song et al., 2013). The set-up of BIV in this study was placed above the domain of interest with a top lighting provided by two Fresnel lights (500 Watt and 1000 Watt), as shown in Fig. 2.4(b). A high speed camera (SpeedCam MiniVis e2) with a 512×512 CMOS sensor record images. The field of view (FOV) covered the main part of the overtopping waves in front of the wall, as shown in Figure 2.4(b). The centre of the focal plane was located at 0.05 m behind the glass wall, see Fig. 2.4(a); The depth of field (D) is $0.055 - 0.08$ m, which is calculated by using focal distance $L = 0.95$ m; the value for the circle of confusion $c = 0.008$ m, focal length $f = 25$ mm and focal length number $N = 2 - 2.8$. Details of the calculation and definition of each parameter used for the BIV set-up can be found in Ryu et al. (2005). The high speed camera was sampling at 1000 frames per second throughout the impact of one or two waves. The overtopping wave surface in each image was detected, color inverted and then cross-correlated to obtain the instantaneous velocities using PIVlab developed by Thielicke and Stamhuis (2014). The velocity determination was performed with a 32×32 pixel interrogation area with a 50% overlap between the adjacent areas.

2.3.3. TESTS AND DATA PROCESSING

The tests were conducted with three type of waves: regular waves, bichromatic waves and irregular waves. The aim of using regular waves is to provide a good experimental repeatability to investigate the individual wave impact (see Appendix 2.A, in which the repeatability of the regular wave tests can be found). Whereas using bichromatic (Bi.)

and irregular (Irreg.) waves are to investigate the influence of the interactions between two (or more) overtopping waves on the impact. Bichromatic waves also have a good repeatability. The tests that are tested in this chapter are shown in Table 2.1, in which the wave period and wave height for the irregular waves are spectrum wave height, H_{m0}, and period, $T_{m-1,0}$ respectively.

Table 2.1: Tests used in this chapter

Wave	Test ID	T_{deep} (s)			H_{deep} (m)		T_{toe} (s)	H_{toe} (m)	B (m)	h_{toe} (m)
Reg.	S028026	4.0			0.2		4.2	0.07	0.5	0.09
Irreg.	Jon001(4)	1.8			0.2		6.35	0.08	0.5	0.09
Irreg.	Jon003(1)	2.42			0.2		8.83	0.10	0.5	0.09
		T_1 (s)	T_2 (s)	$1/\Delta f$ (s)	H_1 (m)	H_2 (m)				
Bi.	Bi-B352	1.98	2.47	10	0.26	0.1			0.25	0.09
Bi.	Bi-C532	2.04	2.38	14.29	0.26	0.16			0.5	0.05

2.4. INDIVIDUAL OVERTOPPING WAVE IMPACT

The impact pressure from each overtopping event is different because of the air entrainment and the turbulence within the overtopping wave. Even though the tests were conducted with regular waves, the individual impact of the subsequent incoming waves still shows irregularity in magnitude, and double-peak shape of the time series. Fig. 2.6 provides an example of the impact force signal from an overtopping event. The red line indicates the total horizontal force measured by load cells and the other four lines (P1 to P4) illustrate the time series of pressure sensors. The locations of the pressure sensors are depicted in Fig. 2.5. From the time series of P1, we can recognize the initial impact peak with short duration and a quasi-static peak with long duration. It is interesting to see that the ratio of impact duration (Δt) and wave period at the dike toe T is 0.0075. It is the same order of magnitude duration as observed by Oumeraci et al. (2001) $\Delta t/T \approx 0.001 \sim 0.01$. However, the ratio of initial impact force peak (F_{dy}) to quasi-static impact peak (F_{qs+}) is less than 1, which is outside the range of impact loading defined by Kortenhaus and Oumeraci (1998) as $F_{dy}/F_{qs+} > 2.5$.

2.4.1. IMPACT PROCESSES

Based on the different dominant physical mechanisms, a whole impact process can be divided into four stages: pre-impact, Fig. 2.7 (a); initial impact, Fig. 2.7 (b); deflection, Fig. 2.7 (c), and reflection in Fig. 2.7 (d). The instantaneous pressure distributions of the same snapshot moments and the four pressure sensors are shown in Fig. 2.7 (e)-(h). From Fig. 2.6, two distinct peaks can be seen in the pressure signal of P1 (black line), whereas a tiny peak is shown before the initial impact peak and a terrace shape pressure evolution after the quasi-static impact peak can also be recognized. Due to a lack of

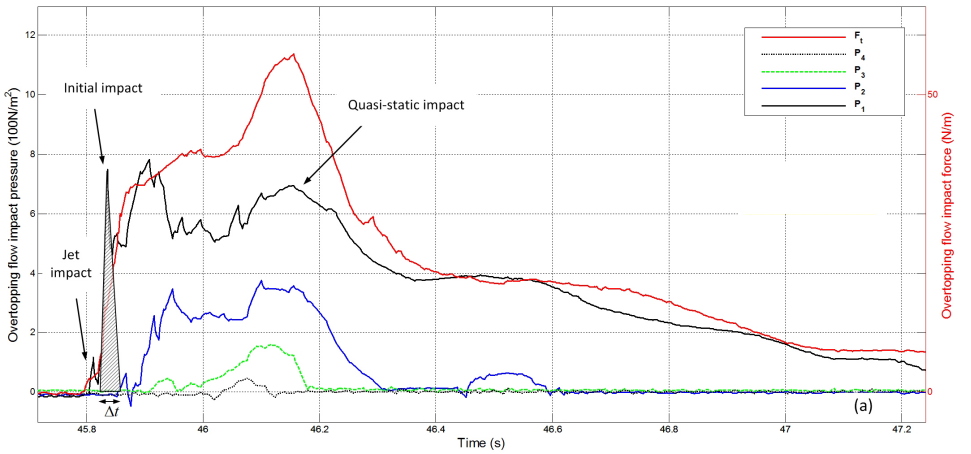

Figure 2.6: Example of the time series signals of total force from load cell and pressure sensors of test S028026. Δt is the approximate impact duration.

pressure information just at the bottom of the wall, it is expected that the tiny peak and the initial impact peak would be larger at the base of the wall. Details of each stage are described below:

- Pre-impact stage

After passing the outer dike crest line, the overtopping wave approaches the wall with a wedge shaped leading edge from left to right, see Fig. 2.7 (a). The bore front, moving over the thin residual water layer, is at the front of the wedge. The turbulent fluctuations in the flow front are expected to generate local pressure fluctuations.

- Initial impact stage:

Fig. 2.7 (b) shows the initial impact process. When the irregular bore front touches the wall face, a rapidly rising tip forms a vertical jet earlier than the initial impact of the main wedge. From Figure 2.6, we can observe this initial jet impact from the time history of P1. The tiny peak before the main initial impact peak indicates this jet impact. It is assumed that the vertical jet dampens the main impact during the initial impact stage. Oumeraci et al. (1993) gave a similar description for a bore impact process. They stated that a bore consists of two parts, including a steep turbulent front and a rear of the water mass. The foamy front part strikes the wall first, then is squeezed by the following impacting "pure" water. This "pure" water impact is significantly dampened by the earlier foamy mass which is then deflected upwards. In the current situation, the jet impact of the overtopping wave is equivalent to direct impact of a turbulent bore front on the wall.

When the main wedge touches the wall, the wave front changes its direction suddenly (Fig. 2.7 (b)) and results in a sharp dynamic impact pressure at P1 (Fig. 2.7 (f)). Because P1 was mounted at 4 cm above the dike crest, the largest pressure of the jet impact was probably not measured. This is the 1^{st} main peak shown in Fig. 2.6 named as

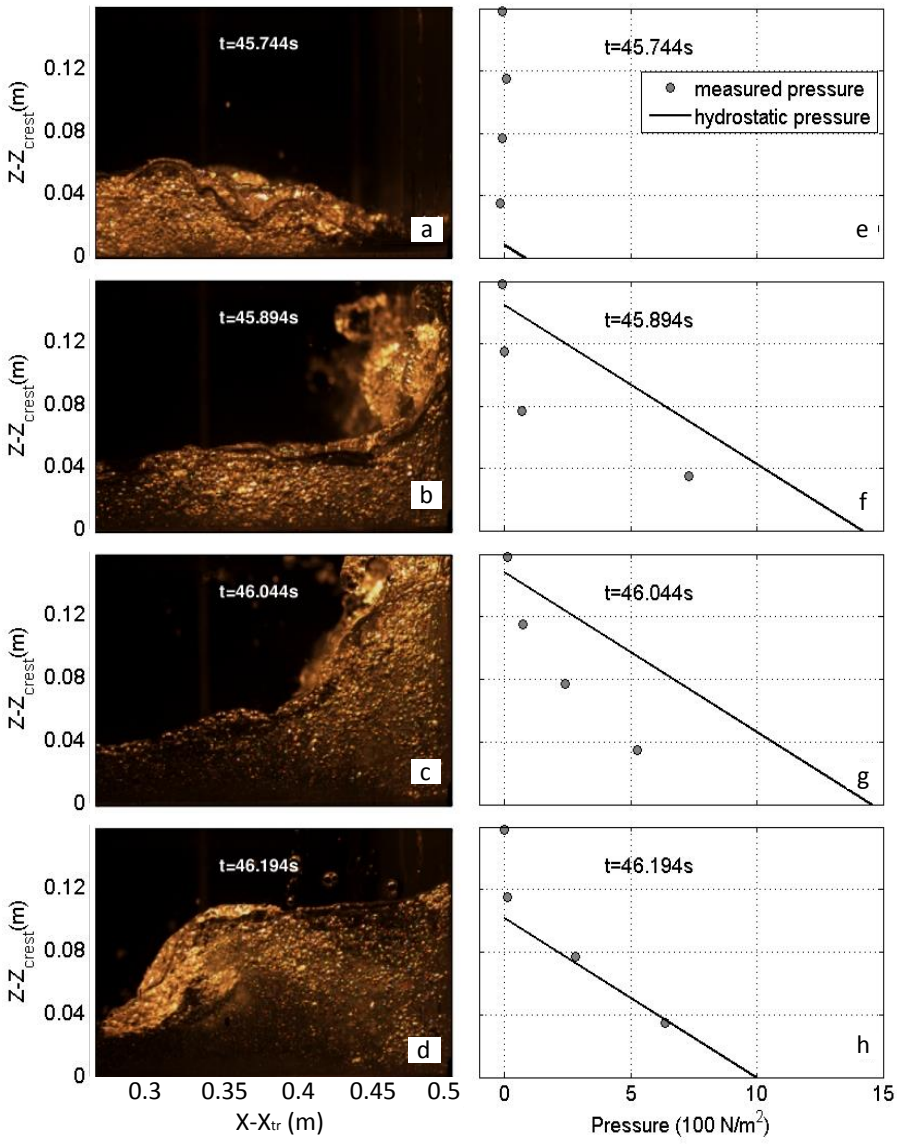

Figure 2.7: An example of the overtopping flow impact process of the second wave of test S028026;(a)-(d) side view of bore impact at wall; (e)-(h) instantaneous measured pressure profile (circle marker) and computed hydrostatic pressure (= $\rho g h_r$) (solid line), h_r is the highest water surface elevation at x_w extracted from raw image. Note that $x - x_{tr}$ and $z - z_{crest}$ are the horizontal and vertical coordinates of the dike crest. The wall is located at $x - x_{tr} = 0.5$ m.

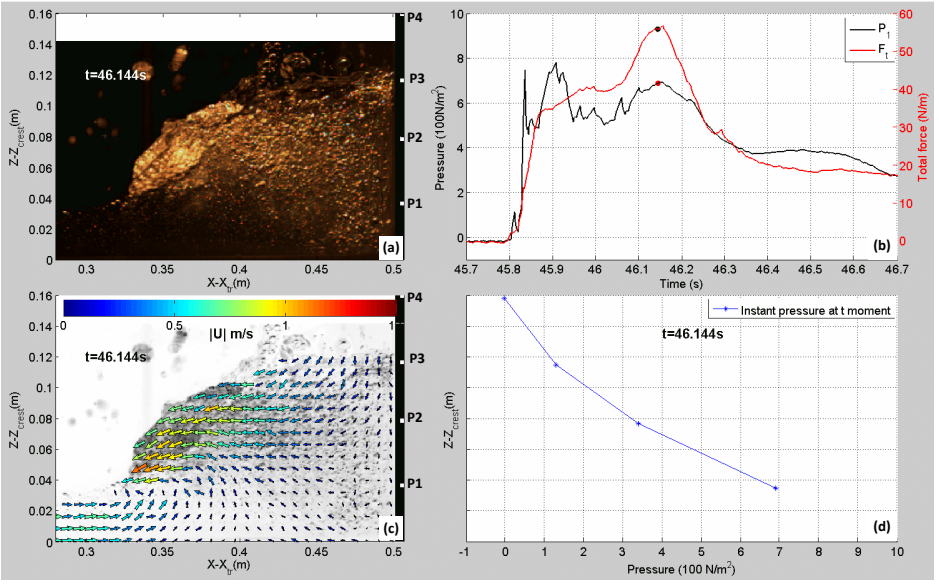

Figure 2.8: An example of the measured flow field at the moment of the 2^{nd} impact force peak of test S028026. (a) raw high speed image at t=46.144 s; (b) impact time series of P1 (black) and total force obtained from load cell (red); (c) velocity field at t=46.144 s; and (d) instantaneous measured pressure distribution at the same moment.

initial impact. During this process, the kinetic energy is changing into potential energy. The short duration of the initial impact pressure could only influence local structural elements with a high natural frequency.

- Deflection stage :

After the initial impact, the following wedge continues rising up the face of the wall until it reaches the maximum run-up height. During this stage, the kinetic energy is totally converted into potential energy. Fig. 2.7 (c) shows the snapshot of run-up of the deflected water. The corresponding instantaneous pressure distribution along the wall is shown in Fig. 2.7 (g), in which the solid line indicates the computed hydrostatic pressure distribution using the run-up surface elevation from the image taken by the high speed camera and the markers indicate the measured pressures. The linear distribution of pressure shows the quasi-static nature of the pressure in this stage, which is smaller than computed hydrostatic pressure.

- Reflection stage:

When the deflected water approaches the maximum run-up level, it starts falling onto the remaining unsplashed part of the incident wave and is advancing seawards (Fig. 2.7 (d)). The quasi-static peak (2^{nd} peak shown in Fig. 2.6) is generated during this stage. Fig. 2.8 shows a group of figures of the overtopping wave features at this maximum force: (a)

raw high speed image, (b) time series of P1 and force, (c) velocity field and (d) instant pressure distribution at the moment of t=46.144 s. The zero velocity vectors close to the wall in Fig. 2.8 (c) and almost linearly distributed instantaneous pressures in Fig. 2.8 (d) indicate the quasi-static nature of 2^{nd} force peak shown in Fig. 2.8 (b). This quasi-static pressure is governed by gravity. Fig. 2.7 (d) shows the reflected bore. When the reflected bore is fully developed, the instantaneous pressure is hydrostatic, see Fig. 2.7 (h).

2.5. IMPACTS OF MULTIPLE OVERTOPPING WAVES

2.5.1. GENERAL OBSERVATIONS

On a shallow foreshore, forced long waves are released from the short-wave groups when they are in shoaling and breaking processes (Van Dongeren et al., 2007). This wave group propagation is observed in the irregular wave tests. The shallow water condition present seaward of the dike causes a wave energy transfer to low frequencies (Van Gent, 2001). Fig. 2.9 shows an example of the time series of overtopping wave measured at different locations in the flume from test JON003(1). Fig. 2.9(a) indicates the total measured time series of the water surface elevation at the toe of the dike. The low frequency waves at the time scale of the wave groups can be recognized. During overtopping, the short waves within each group break on the dike successively in the form of bore. Fig. 2.9(b) shows the time series of the overtopping flow layer thickness measured on the dike crest without (Section A), and with a wall (Section B). As shown in the figure, the overtopping waves on the dike are still grouped. Fig. 2.9(c) shows the time series of overtopping wave forces, which is filtered by a low pass filter at 50 Hz[1]. The number of force peaks is obviously less than that of the incoming waves at the outer crest line ($d_{A0(t)}$) in Fig. 2.9(b). It suggests that some of the overtopping waves within groups have converged or damped before giving an impact.

2.5.2. INTERACTION BETWEEN SUBSEQUENT OVERTOPPING WAVES

Erikson et al. (2005) state that wave motions in the swash zone are driven by the propagation of wave groups and their associated long wave motion. Wave 3 and 4, as shown in Fig. 2.10, indicate the parabolic swash motion along the dike seaward slope, with the inclusion of "catch-up" (Fig. 2.10(a)) and "collision" (Fig. 2.10(b)). The "catch-up" motion addresses the interaction between the two subsequent waves in the same direction. Whereas the "collision" addresses the interaction between the two subsequent waves in an opposite direction. The overtopping wave motion within each group observed is similar to the swash described by Erikson et al. (2005), such as wave 1 and wave 2 in Fig. 2.10. The short waves within a wave group overtop the dike crest and result in a group of impacts. Due to the interaction between overtopping waves, the impact mechanism can be altered compared to the individual overtopping impact.

The upper panel of Fig. 2.11 shows schematic sketches of four interaction motions between wave 1 and wave 2, and the bottom panel shows the corresponding schematic time series of the traveling routes of the two waves on the dike crest. t_1 and t_2 are the

[1] The natural frequency of the entire low rise buildings is around 5-15 Hz in real scale (De Sortis et al., 2005). Thus the mean value 10 Hz of this range (or 50 Hz in model scale using a typical model scale of 1:25) was used as the cut-off frequency for the low-pass filter.

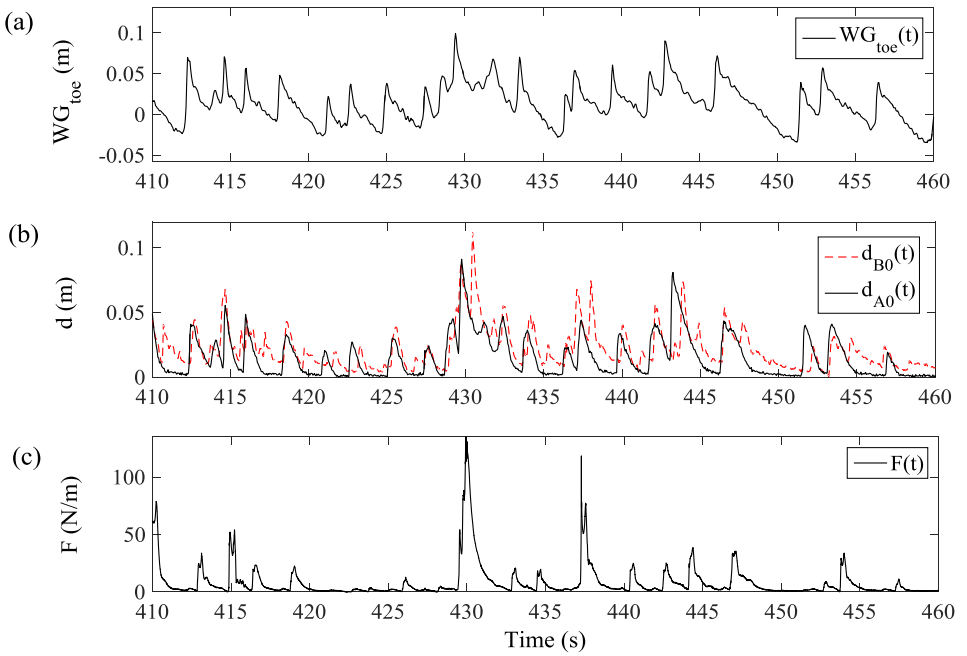

Figure 2.9: Sample of the surface elevation at the toe of the dike; (b). the overtopping wave time series d_{A0} (solid line) and d_{B0} (dashed line); (c). Sample of the overtopping wave force time series

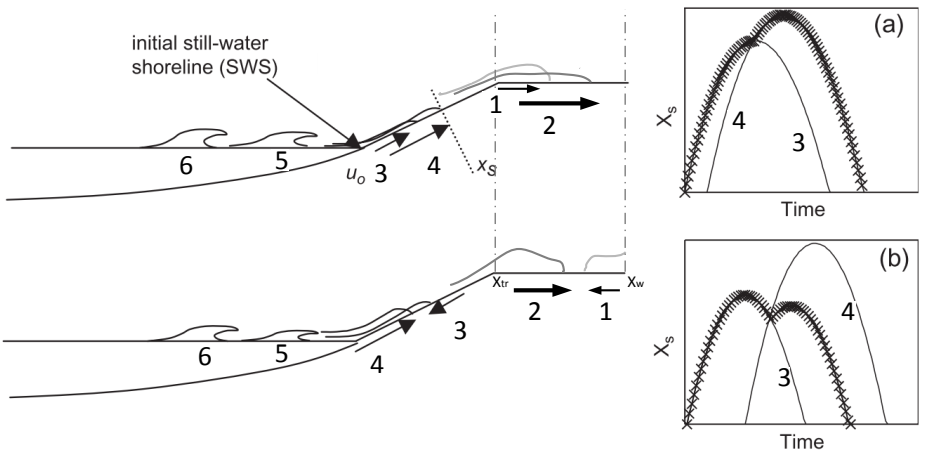

Figure 2.10: Swash motions of incident waves, adapted from Erikson et al. (2005): (a) catch-up motion between wave 3 and wave 4 on the seaward slope of the dike; (b) collision between the wave 3 and wave 4.

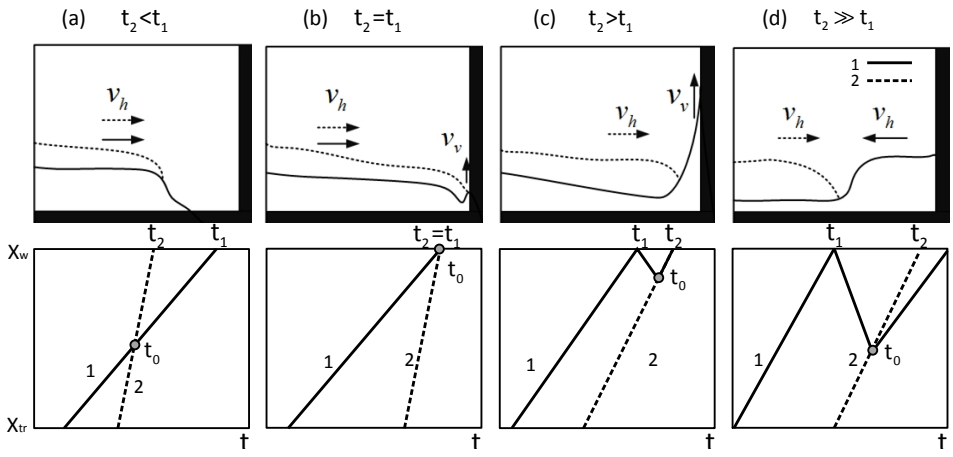

Figure 2.11: Interaction motions between the initial wave 1 (solid line) and the following wave 2 (dotted line). Dot indicates t_0, the moment of the wave 1 interacting with wave 2.

initial impact moment of wave 1 and wave 2 if there is no interaction between them. t_0 indicates the interaction moment between the two waves. Dashed gray and black curves show the undisturbed traveling routes of wave 1 and wave 2. The blue curve indicates the half route of the "new" formed overtopping wave with consideration of the interaction. Based on the time lag between t_1 and t_2, four types of interactions are observed.

WHEN $t_2 < t_1$

Wave 2 will catch up with the initial wave 1 before the impact of wave 1 on the wall, as shown in Fig. 2.11(a). This catch-up interaction generates a "new" overtopping wave. If $t_0 \ll t_1$, the catch-up occurs far away from the wall. Thus the resulting impact of the "new" wave can be seen as an individual overtopping wave.

WHEN $t_1 = t_2$

Wave 2 will catch up with wave 1 just on the wall, as shown in Fig. 2.11(b). This interaction will result in a highly turbulent and steep wave front, which will induce a violent impact. Fig. 2.12 shows a sequence of the evolution of this case. The snapshots in the first column of Figs. 2.12(a)-(e) present the catch-up process in front of the wall. When wave 2 runs on the top of wave 1, a turbulent wave front is formed. The "new" overtopping wave front velocity increases due to the increased overtopping flow depth. Figs. 2.12(e)-(h) show a whole impact process of the "new" wave. Pressure records along the wall of the corresponding impact are shown in Fig. 2.13. It can be seen that there is an impulsive impact with large magnitude within a short duration. The maximum peak pressure with a value up to 8 KPa occurs at P1. Fig. 2.14 shows the correspondent total horizontal force measured from load cells (black solid line) and the pressure sensors (red line). The general shape of the force is a typical "church-roof" signal (Oumeraci et al., 1993). The dynamic peak with large magnitude and short duration occurs around 141.38 s, followed by the quasi-static force peak around 141.7 s. Both of the forces obtained from

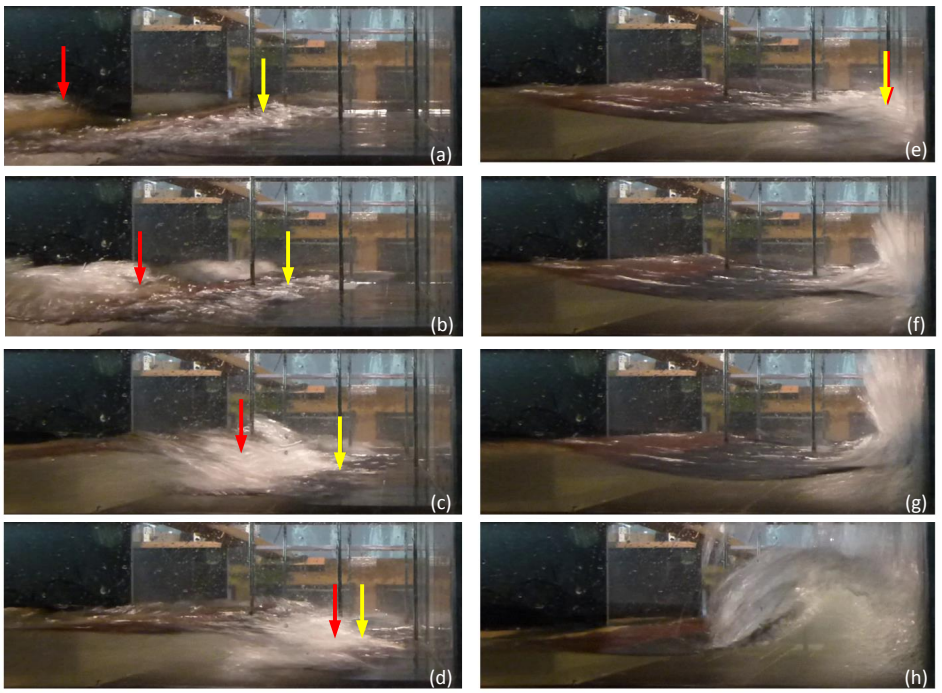

Figure 2.12: Snapshots for an overtopping wave impact (test Jon001(4), t=139-143 s). Yellow arrow indicates the locations of the initial wave 1, and the red one indicates the following wave 2.

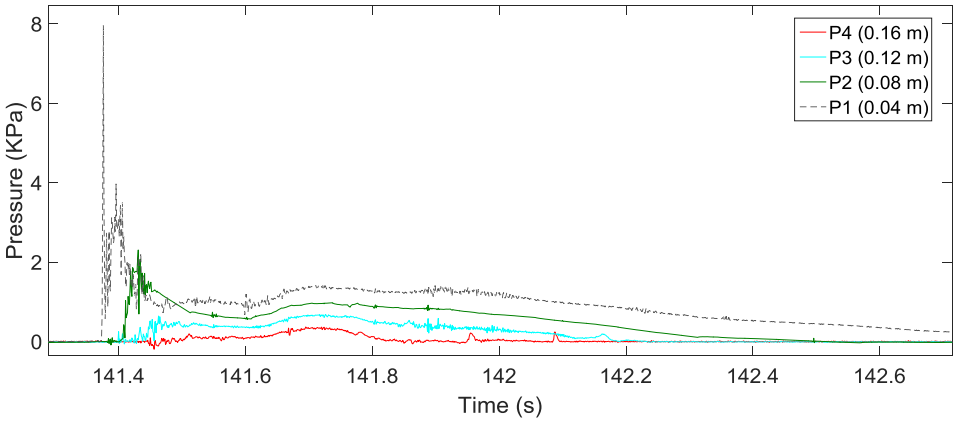

Figure 2.13: Simultaneous pressure records from the four pressure sensors of test Jon001(4) when t=139-143 s.

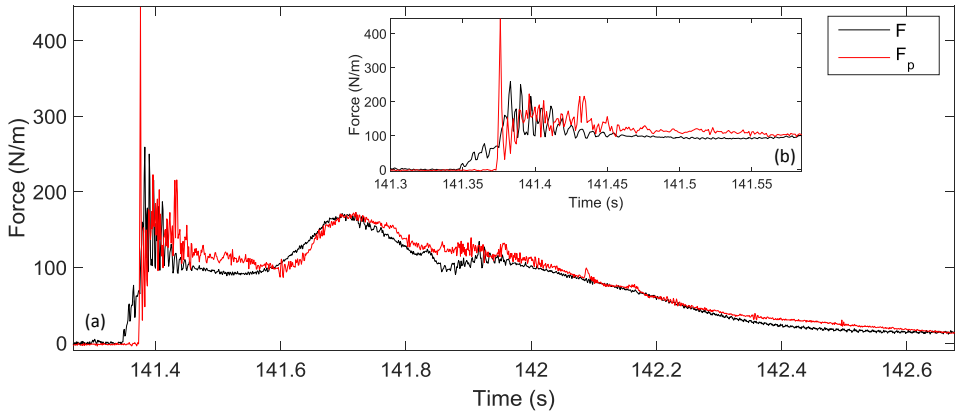

Figure 2.14: Simultaneous force records from the load cells (black) and integrated pressure sensors (red) of test Jon001(4) when t=139-143 s.

load cells and pressure sensors give consistent observations. According to the definition of the breaking wave impact, the dynamic force peak is larger than 2.5 times of maximum quasi-static force peak (Oumeraci et al., 2001), this impact resembles a breaking impact. A gently increasing force (black solid line) is observed before 141.38 s in the figure. But comparing with the time series of P1 in Fig. 2.13, the violent impact occurs after 141.38 s. This suggests that the location of the dynamic impact is not at the bottom of the wall, but around the surface of wave 1. Thus the catch-up moment is around 141.38 s. Oscillations after the dynamic peak (Fig. 2.14(b)) are observed in the signals of both the load cell and pressure sensors. This oscillation is probably induced by the compressed trapped air during the interaction of the turbulent wave front and the wall.

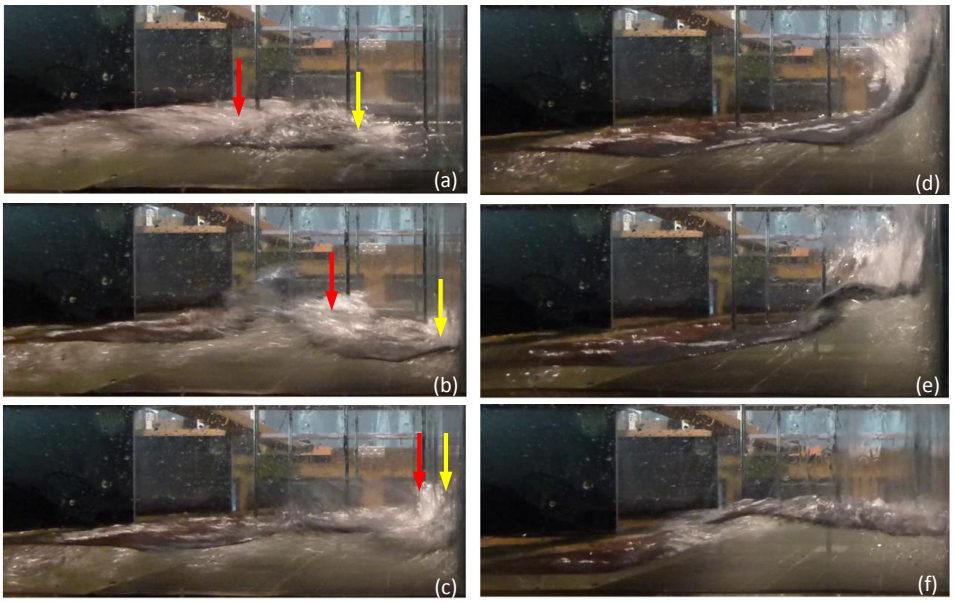

Figure 2.15: Snapshots of the wave shape developments of catch-up impact (test Jon001(4), t=174-175.5 s). Yellow arrows indicate the locations of the first waves, and the red ones indicate the successive waves.

WHEN $t_2 > t_1$

Wave 2 impacts on the wall just after the impact of wave 1, as shown in Fig. 2.11 (c). Fig. 2.15 shows six snapshots in sequence of the evolution of overtopping wave impact for this case. Due to the delayed catch-up (see Fig. 2.15(a)-(c)), a duo-impact on the wall is observed. During the deflection stage of wave 1, wave 2 strikes on the deflected wave 1 (see Fig. 2.15 (c)). Afterwards, the two waves merge during deflection stage (see Fig. 2.15 (d)). Fig. 2.15 (e)-(f) shows the reflection stage of the impact. No violent dynamic impact is observed due to "cushion" of wave 1 at impact moment. The corresponding pressure records along the wall are shown in Fig. 2.16. Comparing the four time series of pressures, only P1 displays a triple-peak shape. This suggests the merging (or catch-up) process of the two waves occurs just after the first peak (around 175.02 s) of P1.

WHEN $t_2 \gg t_1$

Wave 2 strikes on the reflected wave 1. Due to the collision between the two directional waves, the impact mechanism can be altered. If the collision occurs just in front of the wall, the "new" combined wave will impinge on the wall in a kind of plunging wave, which is in line with the observation from Kamikubo et al. (2009).

Fig. 2.17 shows an impression of an observed collision between the two waves including the near wall "collision" formation (a)-(c), flow separation and "new" wave generation (c)-(d), and the impact (d)-(e). If the second wave dominates the collision, the fast collision will create a plunging wave with a large air cavity in front of the wall (Fig. 2.17d). This impact can induce an impulsive violent impact at a much higher location on the

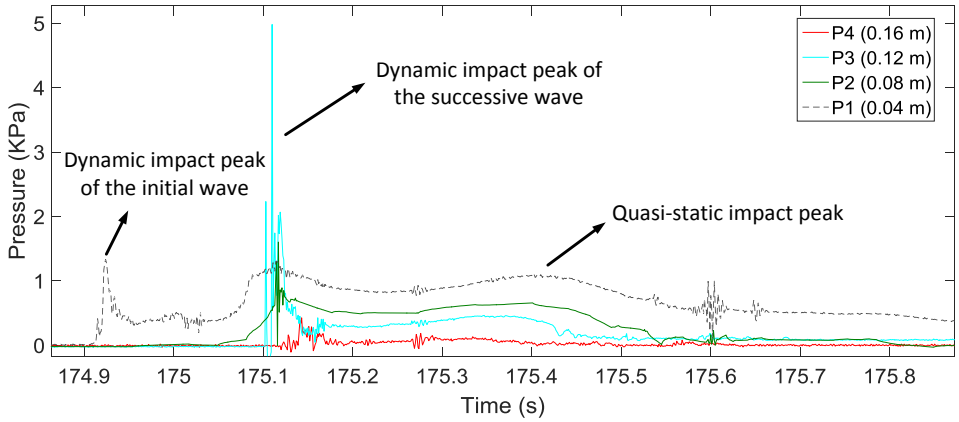

Figure 2.16: Simultaneous pressure records from the four pressure sensors in test Jon001(4) when t=174-175.5 s).

wall (Fig. 2.17e). Fig. 2.18 shows snapshots of a large air cavity involved "collision" impact overlapped with the velocity field, of the bichromatic wave test Bi-B352. The "new" wave after collision approaches to the wall from left to right with a wave front velocity around 1.2 m/s. The air cavity created in front of the wall limits the size of final impact region. From Fig. 2.18(a) to Fig. 2.18(b), an air cavity with a height around 0.04 m is formed. Afterwards, the curling wave front focuses at the centre of the cavity and impacts on the wall. In a kind of flip through impact (see Peregrine, 2003), the wave front velocity just before the impact increases to 1.4-1.5 m/s, as shown in Fig. 2.18(c)-(d). Fig. 2.19 shows the time series of four pressure sensors mounted on the wall at 0.04 m (P1), 0.08 m (P2), 0.12 m (P3) and 0.16 m (P4) above the dike crest. From 48.5 to 49 s, the initial impact caused by the first incident overtopping wave is clearly recognized. The initial dynamic peak of P1 occurring around 48.5 s is about four times larger than the quasi-static peak occurring at 48.7 s. As for P2, there is no sharp dynamic impact peak. Comparing the time series of the signals of P1 and P2, it indicates that the initial impact occurred close to the bottom of the wall. The "collision" between the reflected wave and following wave in front of the wall occurs at around 49 s. The impact after the collision starts at 49.2 s. From the time series of pressure sensors, a sharp dynamic peak is distinct at P3. It indicates that a violent impact occurs close to 0.12 m above the bottom. In the time series of P4, two dynamic peaks occur earlier and later than the dynamic peak of P3. The first dynamic peak of P4 is earlier than P3. This indicates that the impulsive impact is caused by the air cavity. This impact mechanism is similar to a breaking wave. Fig. 2.20(a) shows the calculated pressure-impulse by using Cooker and Peregrine (1995)'s pressure-impulse theory for the impact moment in Fig. 2.18. In Fig. 2.20(b), the solid curve is the calculated impact pressure profile along the wall. The red circles illustrate the measured the pressure value at the different locations. Good agreement is found between the measured p and the Cooker and Peregrine (1995)'s model, using the measured values of H, U_0, and Δ_t. This indicates that this model is applicable for the overtopping wave colli-

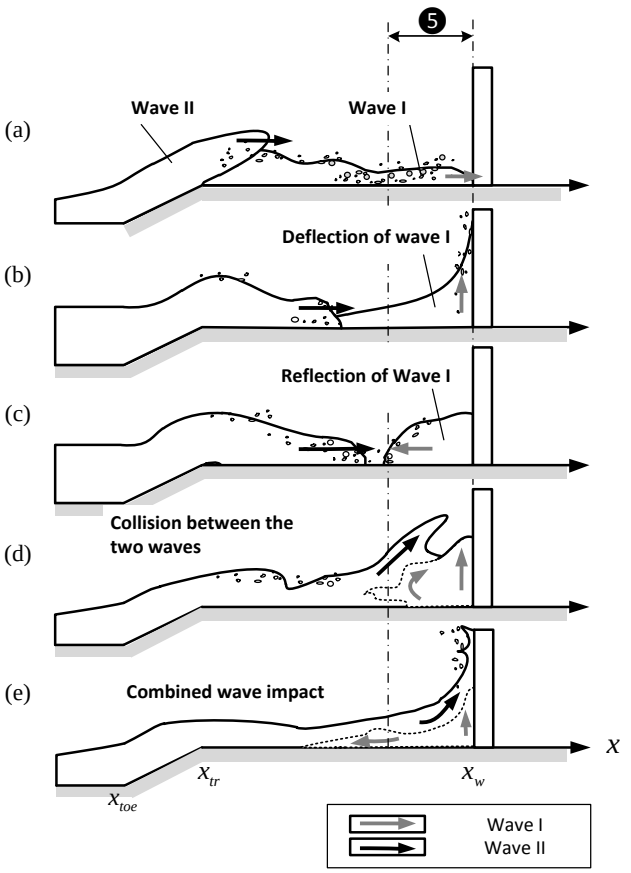

Figure 2.17: Schematic sketch of collision impact with successive overtopping waves

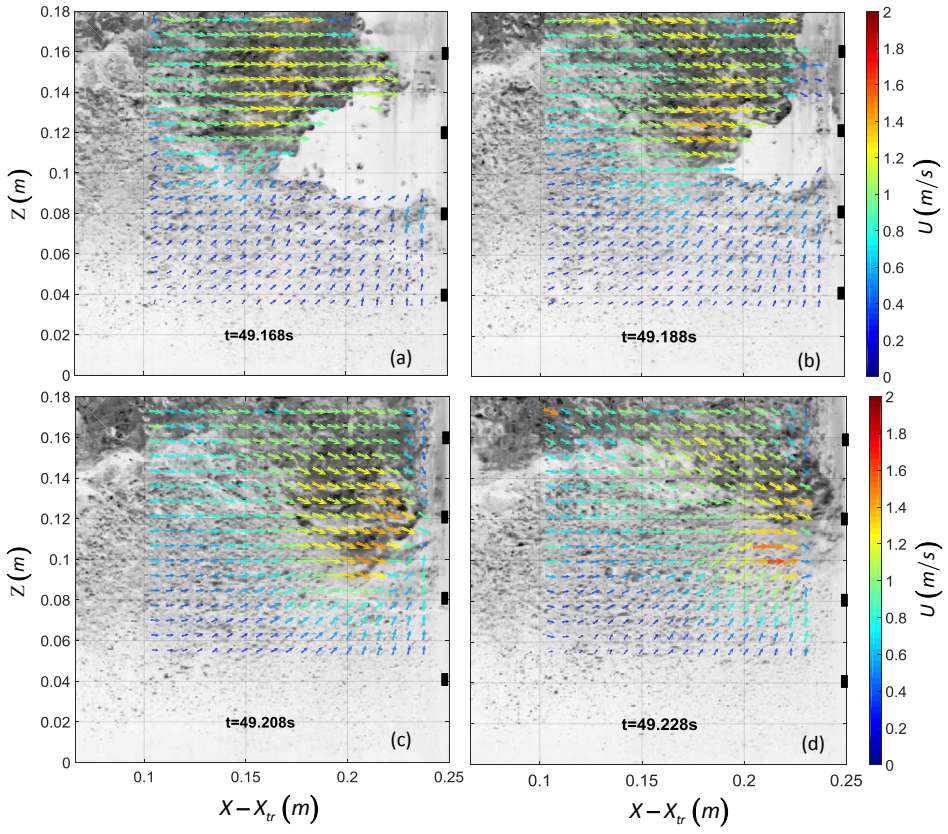

Figure 2.18: Collision impact caused by two successive overtopping waves of test Bi-B352. Four pressure sensors (P1 to P4 from bottom to the top) are illustrated as black points.

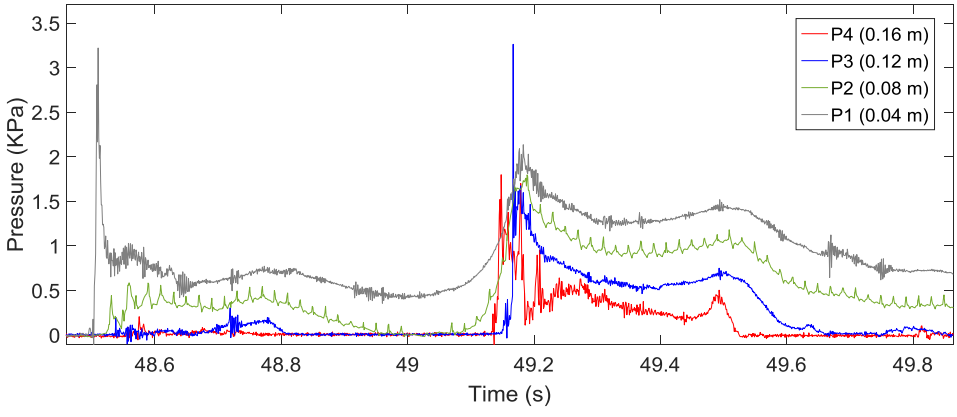

Figure 2.19: Simultaneous pressure records of the collision impact caused by two successive overtopping waves of test Bi-B352.

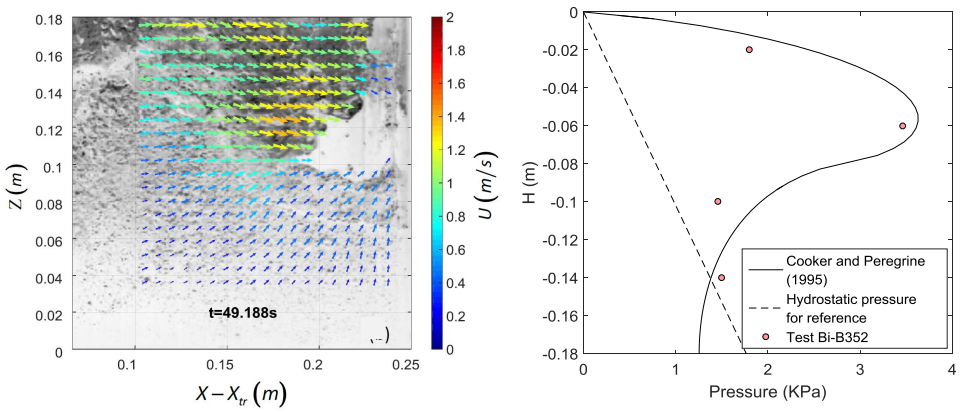

Figure 2.20: (a) Pressure-impulse calculated of test Bi-B352 for the overtopping wave at the moment shown in Fig.2.18; (b) the calculated pressure with $H = 0.18$ m, $U_0 = 1.22$ m/s, $\mu = 0.44$, $\Delta t = 0.03$ s. Wall is at $x - x_{tr} = 0.25$ m.

sion impact when a plunging wave impact is formed.

If the collision does not occur near the wall, the curling wave front would fall directly on the surface of the reflected wave 1. Then the "new" wave strikes on the wall with a steep wave front. This impact is similar to that of a single overtopping wave with a wedge shape. Fig. 2.21 shows snapshots of an impact overlapped with its velocity field for this case. The "new" wave after collision approaches to the wall from left to right. Fig. 2.21(a) to (d) shows the impact caused by the turbulent wave front with a velocity around 1.7 m/s. Afterwards, the dynamic impact of the main wedge is shown in Fig. 2.21(e) to (h) with a front velocity around 1.5 m/s. Fig. 2.22 shows the time series of the four pressure sensors for the impact. Two individual impact events are clearly recognized. From 46 to 47 s, the impact of wave 1 occurs. The whole two-peak time series of P1 during this process indicates that wave 1 has finished its impact and has been reflected back seawards. The collision between wave 1 and wave 2 occurs at around 46.9 s. Due to the collision, wave 2 rides on the top of wave 1, the location of the dynamic impact of "new" wave is around 0.07 m (close to P2), as shown in Fig. 2.21(c). During 47.1-47.2 s, there are multiple peaks shown in the time series of P2 and P3. These peaks are believed to be caused by the oscillation of the turbulent wave front during the initial impact stage. Among these oscillated peaks, there are two distinct peaks. Both of these peaks of P2 are earlier than those of P3, which suggests that the wave front is rising from bottom to the top. This indicates that there are two impact events, which confirmed the occurrence of a turbulent wave front impact and the main wedge impact during the initial impact stage for "new" wave impact after the collision.

2.6. DISCUSSION AND CONCLUSION

Prior work has documented the characteristics of the impacts of waves (e.g., breaking wave impact and broken wave impact on a wall). However, these studies lack direct rele-

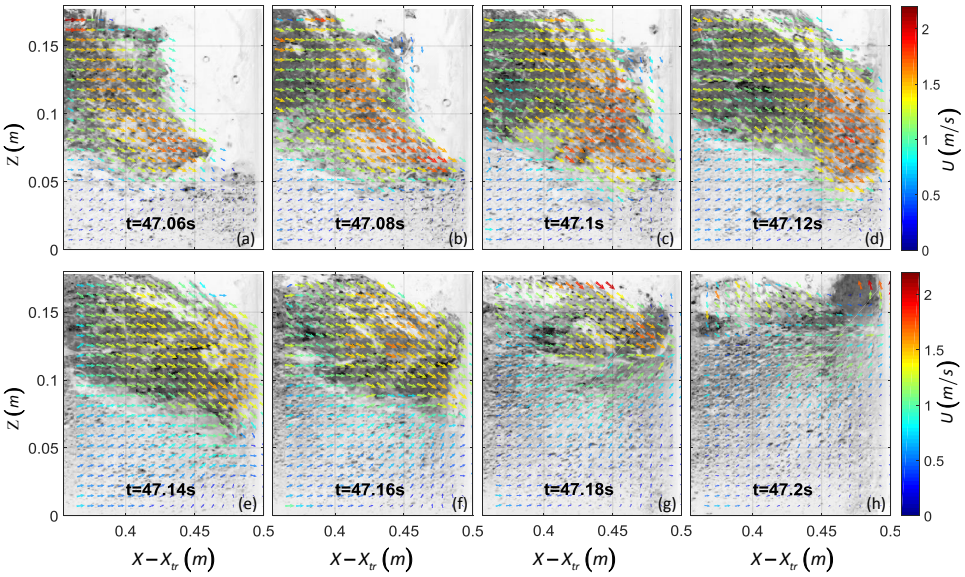

Figure 2.21: Collision impact far from the wall of test Bi-C532. Wall is at $x - x_{tr} = 0.5$ m.

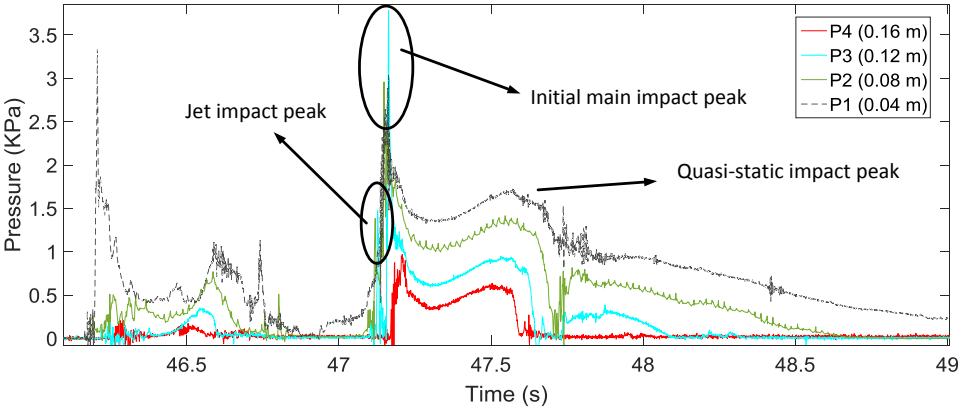

Figure 2.22: Time series of the pressure sensors at different locations along the wall of test Bi-C532.

vance to describe the overtopping wave impact mechanisms concerning the interaction between multiple incident waves on the dike crest. In this chapter, the impact process and mechanism of overtopping waves on a dike crest were presented based on the observations from the tests by using regular waves, bichromatic waves and irregular waves.

The whole impact process of a single overtopping wave can be divided into four stages: pre-impact, initial impact, deflection and reflection. The maximum total force occurs at a later phase of deflection or early phase of reflection. The time series of overtopping wave force shows a double-peak shape. This shape is in line with the existing knowledge of wave impact force, though the magnitude differs from impulsive impact defined by Oumeraci et al. (2001). The velocity field of the overtopping wave during the impact proves that the 2^{nd} impact peak is static. The turbulent wave front induces jet impact. Due to lack of information of pressure at the location below P1, the influence of jet impact on the initial load development needs to be investigated in the future.

For multiple interaction waves, two basic patterns of "collision" and "catch-up" are observed, which are similar to the swash motion on a beach. Impulsive impact of the overtopping waves can be caused by the interactions between two successive overtopping waves. Due to collision between two waves near the wall, an air cavity may be formed. This impact is quite similar to a breaking wave impact on a vertical wall, and can be predicted well by using Cooker and Peregrine (1995)'s pressure-impulse model. When the catch-up occurs far away from the wall, the resulting "new" overtopping wave is similar to a single wave impact. When the catch-up occurs just on the wall, an impulsive impact may be expected. When the catch-up occurs later than the initial impact of the first wave, the second wave would impact directly on the body of the deflected initial wave. The deflected wave plays a role of a "cushion". The magnitude of the dynamic impact of the second wave is reduced. When the collision occurs at a certain distance away from the wall, the impact mechanism is similar to a single overtopping wave, but the impact caused by the turbulent wave front is obvious and at a higher location on the wall.

The probability of occurrences of each impact type of overtopping waves was excluded in this thesis. But some preliminary analysis have been done. The largest three impact forces of each test from a total of 39 irregular wave tests with different conditions were considered within this analysis. Among these 117 significant impacts, the impacts caused by the single wave, catch-up interaction and collision take up 48%, 23% and 29% respectively. Among these 117 impacts, impulsive impact due to either catch-up on the wall or near wall collision takes up about 35%. Thus impulsive impact induced by overtopping waves needs to be paid more attention especially for the stiff structures with a high eigenfrequency. Moreover, overturning moments and local pressure at higher elevation will be governed by the collision type impacts. In the future, it is recommended to extend the current study in order to characterize the classification of each overtopping wave impact caused by different interaction motions.

The pressure gradient on the bed could lead to the removal of the top layer of the pavement and hence the initiation of scour, for which can be referred to Eq. 2.5. Thus it is suggested to specify the pressure field (e.g., the pressure distribution at the corner of a vertical plate) in order to investigate the scour due to the overtopping wave impact.

APPENDIX

2.A. EXPERIMENTAL REPEATABILITY

Much literature discussed the non-repeatability of wave impacts. The reasons of this non-repeatability are mainly a 3D effect of the turbulent front of the incident overtopping wave, and the air-entrapment. In this study, a regular wave test with 33 repetitions was conducted. d_{a01} is the unobstructed overtopping flow depth at the seaward edge of the dike crest in Section A; d_{b01} is the obstructed overtopping flow depth at the seaward edge of the dike crest in Section B; F_{dy} is the dynamic impact force (the first peak), and F_{qs+} is the maximum quasi-static force (the second peak) which are measured by load cells. F_{pdy} is the dynamic impact force obtained from the integration of pressure records along the wall; F_{pqs+} is the maximum hydro quasi-static force obtained from the integration of pressure records. The result of the second wave of test series Sin028 (with 33 repetitions) is shown in Table 2.A1. For the unobstructed overtopping layer thickness, the ratio of the standard deviation and the mean of the total 33 observations is only 4%. The quasi-static force peaks from both the load cells and pressure records give consist results, indicating a good performance of the quasi-static measurement in the current study. While for the dynamic impact forces, the standard deviation obtained from the load cell is around 40% of that from the pressure records, which is reasonable. As explained in the previous section, the load cell measured the total horizontal force subjected to the whole area of the wall whereas the pressure sensors can capture the local features of the incident wave. As the turbulent front of the overtopping wave, the air-entrapment and 3D effect would not be neglected. The standard deviation of F_{pdy} is almost 30% of the mean.

Table 2.A1: Results of repetition of total 33 regular wave tests

	d_{A0} [m]	F_{dy} [N/m]	F_{qs+} [N/m]	F_{pdy} [N/m]	F_{pqs+} [N/m]
Mean	0.046	40	53.7	73.49	60.43
Stedv	0.002	5.89	5.492	21.753	8.144
Stedv/Mean	4%	14%	10%	30%	13%

3

SINGLE OVERTOPPING WAVE IMPACT LOAD

Wave overtopping on a sea dike may pose a threat to people and property. However, the overtopping features, in particular overtopping wave loads, are not well understood. The aim of this study was to understand the overtopping process on a dike crest and to develop an empirical formula for the resulting overtopping wave impact loads on a wall as a function of the property of the incoming waves and dike geometry characteristics. In this chapter, we propose a new descriptor (the overtopping momentum flux) in order to predict the impact loads. To validate the proposed empirical function, a series of physical scale model tests using regular waves was conducted. In these experiments, we measured the overtopping wave loads on a vertical wall at different locations on a dike crest, which were induced by broken waves. A correction coefficient for the wall effect on the initial flow depth, and an empirical initial flow depth coefficient for a broken wave were determined. These empirical coefficients allowed for an interpretation of the overtopping process of a broken wave from the dike toe up to the front of the wall on the dike.

This chapter has been published in: Chen, X., Hofland, B., Altomare, C., Suzuki, T., Uijttewaal, W. (2015). Forces on a vertical wall on a dike crest due to overtopping flow. Coastal Engineering 95, 94-104.

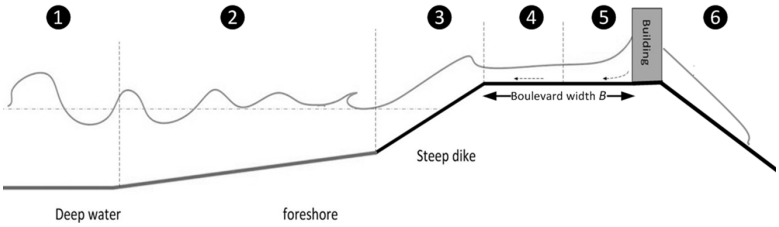

Figure 3.1: The process of overtopping waves impacting on a building: ① Wind generating waves far away from shoreline; ② Offshore waves coming into the foreshore area, increasing wave height, decreasing wave length. Finally, most waves breaking and wave energy dissipating in the form of turbulent bore. ③ Turbulent bore (broken wave) running up on the seaward slope of a dike and overtopping the crest of the dike; ④ Part of the overtopping wave continues propagating along the dike crest and the other part flowing back seaward; ⑤ Overtopping flow hitting the building, with some of it being reflected seaward, some passing through buildings; and ⑥ Overtopping flow going landward.

3.1. INTRODUCTION

Wave overtopping occurs when the dike crest is lower than the wave run-up height. Avoiding or reducing overtopping rates under an acceptable limit, is nowadays recognized as one of the design criteria for coastal structures, especially in those countries characterized by low-lying coastal areas (e.g., the Netherlands, Belgium). In a densely populated coastal town of these countries, a dike often has a wide crest which serves as an urbanized frontage, see Fig. 3.1. It is important for designers and owners to recognize key hazards (e.g., building damage) from overtopping for such buildings standing on the dike crest. As a necessary design criterion for the buildings, overtopping wave load has been considered by few studies (Allsop et al., 2005). Though the overtopping wave characteristics have been investigated by Van Gent (2002), Schüttrumpf and Oumeraci (2005), and Van der Meer et al. (2010) in the form of flow depth, front velocity and discharge along a dike crest without structures, these characteristics are lacking direct relevance to describe the overtopping wave load.

Chen et al. (2012), De Rouck et al. (2012) and Ramachandran et al. (2012) reported overtopping wave loads on vertical structures on a dike crest using small and large scale physical models. However, due to the complex flow characteristics of the highly aerated overtopping wave, to accurately measure the overtopping wave features on a dike crest is still a challenge (De Rouck et al., 2012). To date, the studies mainly describe the impact of the overtopping wave phenomenon. A double peaked force evolution shape of a single impact event is recognized and named as 'dynamic impact force' and 'quasi-static force', which is similar to the proposed "church-roof" wave breaking impact evolution by Oumeraci et al. (1993) for deeper water wave impacts on caissons and composite structures. However, the overtopping wave has no real sinusoidal wave shape, it is a bore-like wave, which could qualitatively be considered as a bore (Cox and Machemehl, 1986). Therefore, overtopping wave impact is outside the classification of the wave breaking impact, as developed by Oumeraci et al. (1993). The mechanisms of impact and the unique overtopping wave characteristics still need to be understood better.

In order to characterize the overtopping wave impacts against a building (simplified as a vertical wall in this paper) on a dike, the literature about two other prototype

problems with similar configurations was investigated: broken wave impact on a crown wall of rubble mound breakwater and tsunami bore impact on a building inland. Overtopping events at crown walls of a rubble mound breakwaters are very similar to the overtopping of a dike: the incoming wave breaks on the seaward slope of the breakwater (processes ① to ③ in Fig. 3.1) and the resulting broken wave overtops the crest and impinges on the crown wall (processes ④ to ⑤ in Fig. 3.1). An important difference is that the slope and crest are very rough and permeable, which will alter the approaching flow. Many studies exist of wave loading on crown walls (e.g., Hamilton and Hall, 1992; Pedersen, 1996; Martin et al., 1999). These studies reported that the horizontal force is proportional to the incident wave height and wave period. Hamilton and Hall (1992) found that lower crown walls yield smaller wave loads compared with a non-overtopped high wall. Pedersen (1996) reported that a gentle seaward slope reduces wave loading. Based on the argument from Cox and Machemehl (1986) about the similarity of a broken wave and a bore , Martin et al. (1999) related the problem of wave impact on the crown wall of rubble mound breakwaters to that of bore impact on a vertical wall and pointed out the quasi-static force is most likely larger than the dynamic force. Kortenhaus and Oumeraci (1998) mentioned that the order of magnitude of the broken wave forces is the same as that of slightly breaking waves. Regarding the tsunami bore impact on vertical walls (similar to processes ④ and ⑤ in Fig. 3.1), some pioneering analytical and experimental researches can date back to Cumberbatch (1960) who provided an analytical solution for the impact pressure of an uniform steady flow striking on a wall. Cross (1967) further developed Cumberbatch's model by adding a hydrostatic pressure term to calculate the total tsunami surge force. Ramsden (1996) investigated the interaction of long waves, solitary waves, bores and surges with a vertical wall. The author observed that the maximum measured total force is quasi-static but less than the hydrostatic force computed by using the maximum measured run-up height of the wall. Arikawa (2008) examined the impulsive tsunami loads on vertical concrete walls by using large scale flume tests. Nouri et al. (2010) investigated the interaction between a hydraulic bore and the impacted structures by using a dam-break approach experimentally. Several authors also studied tsunami forces on various types and shapes of structures (e.g., Arnason, 2005; Arnason et al., 2009; Nouri et al., 2010). Since the possible similarity between an overtopping wave and a bore, the existing knowledge of bore impact could be applied to the total overtopping wave force predictions. An important difference between a tsunami bore and overtopping wave is that overtopping waves are induced by stochastic storm waves. The overtopping wave impact is influenced by the presence of previously reflected waves. This effect is also less for crown walls on rubble mound structures, as the water of successive waves can penetrate into the rubble mound material.

The objective of this study is to develop an empirical formula to predict the overtopping wave load on a vertical wall on a wide crested dike, such as found in low-lying countries. In Section 3.2, a new descriptor, named as overtopping momentum flux, to characterize the total overtopping wave load on a vertical wall is proposed. An empirical formula based on the proposed descriptor is calibrated by a series of physical model tests with regular waves in a shallow water condition. The test set-up and the results are provided in Section 3.3 and Section 3.4. Finally, in Section 3.5 and 3.6, a discussion and conclusions are given.

3.2. OVERTOPPING MOMENTUM FLUX

3.2.1. WAVE MOMENTUM FLUX

Hughes (2004a,b) proposed a method of using maximum depth-integrated wave momentum flux ($M_{F,max}$) to describe the interaction between nearshore waves and a coastal structure, see Eq. (3.1):

$$M_F(x,t)_{max} = \int_{-h}^{\eta(x)_{max}} \left(p_d + \rho u^2\right) dz \tag{3.1}$$

where $M_F(x,t)_{max}$ is maximum depth-integrated wave momentum flux per unit of width at moment t; x is horizontal coordinate; z is vertical coordinate, positive upward with z=0 at still water level; t is time; p_d is instantaneous wave force (or dynamic pressure) on the wall; u is horizontal water particle velocity at the same position; ρ is water density; h is water depth in front of the dike toe; $\eta(x)$ is sea surface elevation at location x. For convenience, the "max" subscript will be removed with following: M_F.

Hughes (2004a) made a simple physical argument: the horizontal velocity u is zero when a perfect reflection occurs on an impermeable vertical wall. Then Eq. (3.1) simply becomes the integral over the water depth of the dynamic pressure, which is also the total instantaneous wave force on the wall. And the maximum depth-integrated wave momentum flux M_F can be determined for any surface wave if the velocity and pressure field are specified.

M_F is a useful concept for the application to both the periodic and transient wave types (Hughes, 2004b), the argument of the relevance of M_F and wave force on structures becomes practical. Therefore, M_F is assumed to be very useful to describe the overtopping wave load as well.

3.2.2. DERIVATION OF OVERTOPPING MOMENTUM FLUX

Fig. 3.2 gives a definition sketch of an overtopping wave propagating on a wide crested dike with boundaries setting as dike toe x_{toe} and the location of wall x_w, covering three zones: Zone 3 (run-up), Zone 4 (overtopping) and Zone 5 (impacting), referring to Fig. 3.1. In the following sections, the overtopping momentum flux is derived for Zone 3 to 5.

INITIAL OVERTOPPING MOMENTUM FLUX IN ZONE 3

In Zone 3, the incoming wave strikes onto the dike slope and runs upward. Fig. 3.3 a illustrates the moment of the incoming wave arriving at the point of maximum virtual wave run-up. The maximum depth-integrated momentum flux (M_F) of the incoming wave before it reaches the dike toe is proportional to the weight of the water contained in the wedge area ABC ($W_{(ABC)}$) (Archetti and Brocchini, 2002; Hughes, 2004a). Here the authors defined the overtopping momentum flux ($M_{F_{ov}}$), which is proportional to the water mass contained in the wedge area CEF ($W_{(CEF)}$) above the dike transition point (x_{tr}), based on the same physical argument made by Hughes (2004a), i.e.,

$$K_P M_{F_{ov}} = K_o W_{(CEF)} \tag{3.2}$$

where K_o is an unknown constant of proportionality and K_P is a reduction factor to account for slope porosity which was defined by Hughes (2004a) ($K_P = 1$ for the imperme-

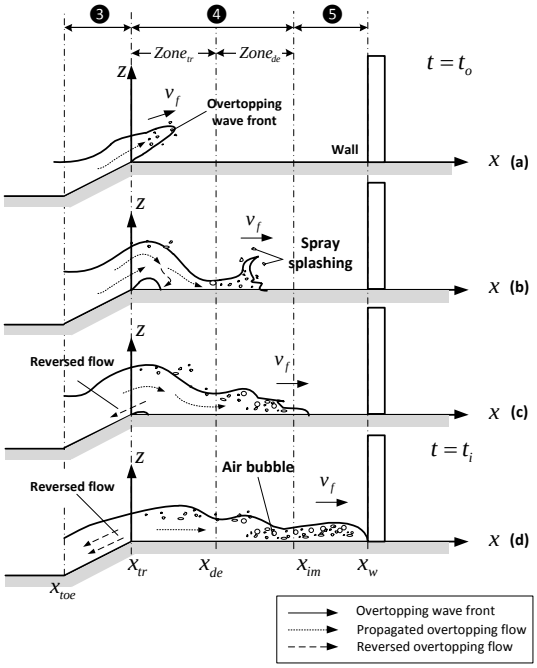

Figure 3.2: Sketch of the propagation of overtopping wave on dike crest

able slopes) as well. $W_{(ABC)}$ in Fig. 3.3a is given by

$$W_{(ABC)} = \frac{\rho g}{2} \frac{R_u^2}{\tan\beta} \left(\frac{\tan\beta}{\tan\theta} - 1 \right), \tag{3.3}$$

where β is the dike slope, θ is an angle between the run-up water surface and the still water level, R_u is the fictitious maximum wave run-up height. The weight of water per unit of width contained in the area CEF is proportional to $W_{(ABC)}$, thus

$$\begin{aligned} W_{(CEF)} &= \left(\frac{R_u - R_c}{R_u} \right)^2 W_{(ABC)} \\ &= \frac{\rho g}{2} \frac{(R_u - R_c)^2}{\tan\beta} \left(\frac{\tan\beta}{\tan\theta} - 1 \right) \\ &= \frac{\rho g}{2} (R_u - R_c)^2 \left(\cot\theta - \cot\beta \right), \end{aligned} \tag{3.4}$$

where R_c is the distance between the dike crest level to still water level (or freeboard). Note that θ depends on the dike slope and wave steepness (Yamamoto and Horikawa, 1992), but the whole term "$\cot\theta - \cot\beta$" can be a function of dike slope and needs to be determined empirically (Hughes, 2004a). Substituting Eq. (3.4) into Eq. (3.2) and rear-

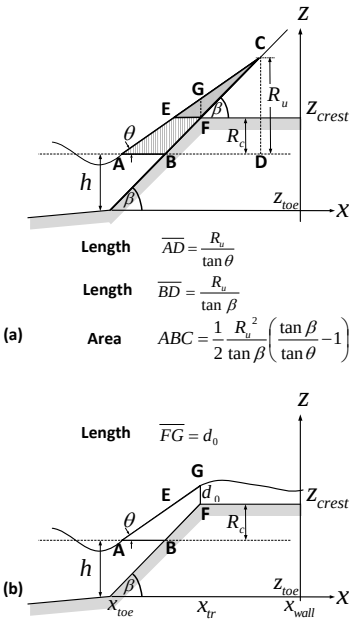

Figure 3.3: (a) Definition sketch of maximum wave run-up on a smooth impermeable plane slope presented by Yamamoto and Horikawa (1992) firstly, adapted from Hughes (2004a), (b) schematic sketch of overtopping wave in real situation.

ranging yields an equation for the initial overtopping momentum flux, i.e.,

$$\begin{aligned} M_{F_{ov}} &= \frac{K_o W_{(CEF)}}{K_P} \\ &= \frac{\rho g}{2}\frac{K_o}{K_P}(R_u - R_c)^2\left(\cot\theta - \cot\beta\right). \end{aligned} \tag{3.5}$$

The maximum initial overtopping wave depth d_0 at x_{tr} (see Fig. 3.3b) is proportional to the difference between R_u and R_c (Schüttrumpf, 2001; Van Gent, 2002; Schüttrumpf and Oumeraci, 2005; Van der Meer et al., 2010), and can be expressed as

$$d_0 = C_1\left(R_u - R_c\right), \tag{3.6}$$

where C_1 is an empirical coefficient.

Substituting Eq. (3.6) into Eq. (3.5), it yields

$$M_{F_{ov}} = \frac{\rho g}{2}\frac{K_o}{K_P C_1^2} d_0^2 f(\beta), \tag{3.7}$$

where $f(\beta)$ is a function of the dike slope, and needs to be determined empirically. After

rearranging, Eq. (3.7) can be rewritten as

$$M_{F_{ov}} = C_2 f(\beta)\rho g d_0^2 \tag{3.8}$$

where C_2 is an unknown empirical coefficient.

OVERTOPPING FLOW IN ZONE 4

When the overtopped flow front drops on the dike crest, the overtopping wave experiences a kind of nappe impact first (Fig. 3.2b), then propagates horizontally to the wall (Fig. 3.2c), and finally impacts on the wall (Fig. 3.2d).

Based on different mechanisms of propagation of the overtopping wave, Zone 4 has been subdivided into two parts: transition zone ($Zone_{tr}$) and decay zone ($Zone_{de}$). Within the transition zone, part of overtopping wave returns back to the sea. The overtopping momentum flux loses a certain part here. Due to the complexity of the momentum exchange process, an unknown factor C_3 is introduced to describe this reduction:

$$M_{F_0} = C_3 M_{F_{ov}} = C_4 f(\beta)\rho g d_0^2, \tag{3.9}$$

where M_{F_0} is the maximum depth-integrated momentum flux at x_{de}. x_{de} is the location where the overtopping wave particle velocity transfers horizontally, and the flow behaves as a progressive wave. C_4 is an unknown coefficient need to be determined experimentally.

The maximum overtopping wave depth, d_x at a specific location x along the dike crest, follows an exponential decay function (Van Gent, 2002; Schüttrumpf and Oumeraci, 2005; Van der Meer et al., 2010, and so on), and is expressed as

$$\frac{d_x}{d_0} = \exp(-\lambda_0 \frac{x - x_{tr}}{B_c}), \tag{3.10}$$

where B_c is the width of the dike crest, and λ_0 is an empirical coefficient to describe the overtopping depth decay rates. Since M_{F_0} is a function of d_0, it would be reasonable to regard $M_F(x)$ at the specific location x on the dike following an exponential decay as well. Thus $M_F(x)$ can be predicted by

$$\frac{M_F(x)}{M_{F_0}} = \exp(-\lambda_1 \frac{x - x_{tr}}{L}), \tag{3.11}$$

where L is local wave length at the dike toe, calculated by $L = CT$. T is the local wave period, and C is the incoming wave local phase celerity, λ_1 is an empirical dimensionless coefficient for the decay rate. Herein, the authors used the local wave length L instead of B_c in Eq. (3.10) due to the irrelevance of dike crest width for the overtopping wave impact event, when a wall appears on the dike.

OVERTOPPING FLOW IN THE IMPACT ZONE (ZONE 5)

In the impact zone ($x_{im} \leqslant x < x_w$, as seen in Fig. 3.2), the dominant process of the overtopping wave changes from energy dissipation into a violent impingement. The appearance of the vertical wall on the dike suddenly alters the features of the incoming overtopping wave. However, the flow features within the tip region are assumed constant

(Cross, 1967) before the tip impacts on the wall. Then going back to the argument made by Hughes (2004a), the maximum depth-integrated momentum flux M_F is a physically relevant descriptor of the wave force on a structure with a force per unit of wave width. Thus the maximum total impact force on the wall is $F_t = \alpha_1 K_R M_F(x_w)$, where $M_F(x_w)$ is the maximum momentum flux near the wall and K_R is a reduction factor to account for the wall height ($K_R = 1$ for high vertical wall which means there is no momentum loss at x_w), and α_1 is an empirical coefficient. Combining the previous equations, the maximum total impact force on the wall F_t can be expressed as:

$$\frac{F_t}{C_5 f(\beta)\rho g d_0^2} = exp(-\lambda_1 \frac{B}{L}), \tag{3.12}$$

in which $B = x_w - x_{tr}$ is the boulevard width, and C_5 is an empirical coefficient.

3.2.3. INITIAL OVERTOPPING WAVE DEPTH

Eq. (3.12) is the derived empirical equation for the overtopping wave load, in which C_5, $f(\beta)$ and λ_1 need to be determined by experiments. The next step is to connect d_0 in Eq. (3.12) with the local incident wave conditions. Martin et al. (1999) predicted the broken wave load on a crown wall for a rubble mound breakwater by estimating d_0^* as

$$d_0^* = \alpha_2 H(1 - \frac{R_c}{R_u}), \tag{3.13}$$

where d_0^* is an imaginary overtopping wave depth at the dike transition point x_{tr}, thus the effect of the wall on the real overtopping wave depth is not taken into account; α_2 is an empirical coefficient. In Martin et al. (1999)'s study, $\alpha_2 = 1$ is determined empirically from Fig. 7 of Yamamoto and Horikawa (1992). However the value of $\alpha_2 = 1$ is not suitable for the present study, it needs to be determined by experiment. For regular wave run-up height R_u on a infinite beach slope, Eq. 3.14 is empirically used:

$$R_u = \xi_0 \cdot H, \tag{3.14}$$

where ξ_0 is Iribarren number ($= \tan\beta / \sqrt{H/L_0}$). For large values of ξ_0, R_u is only related to the incident wave height, and the ratio of R_u/H tends to a constant value. The constant is within a range of 2 to 3 (e.g., Hunt, 1959; Battjes, 1974; Peregrine and Williams, 2001).

3.3. EXPERIMENT SET-UP

3.3.1. FACILITIES

Physical model tests were performed in a 4 m wide, 1.4 m deep and 70 m long wave flume at Flanders Hydraulic Research, Antwerp, Belgium. A piston-type wave generator with a stroke length of 0.6 m was used generating monochromatic, multi-chromatic and random waves, using a passive wave absorption system. The wave flume was split into four sections (approx 1 m for each), as shown in Fig. 3.4. One reason of this design was to test the configurations with and without a wall simultaneously, the other one was to reduce reflected waves by installing passive wave absorption baffles in the

outer sections. The reflection coefficient of the passive wave absorbers is 0.16. By limiting the time series of each experiment to the traveling time of the reflection towards the wave generator, the reflections would not affect the measurements. Incident wave conditions were determined by measuring the waves without a dike in the outer section (Fig. 3.4b); Section A was used to measure the unobstructed overtopping wave features along the dike crest and Section B was used to measure the impact force of overtopping wave. In Section A, the overtopping wave was collected by an overtopping tank behind the dike model, named as unobstructed flow, see Fig. 3.4c. In Section B, the overtopping wave was reflected back seawards after its impingement, named as obstructed flow, see Fig. 3.4d. The shallow foreshore profile and the dike models were made of concrete and wooden plates respectively. The main parameters are depicted in Fig. 3.4.

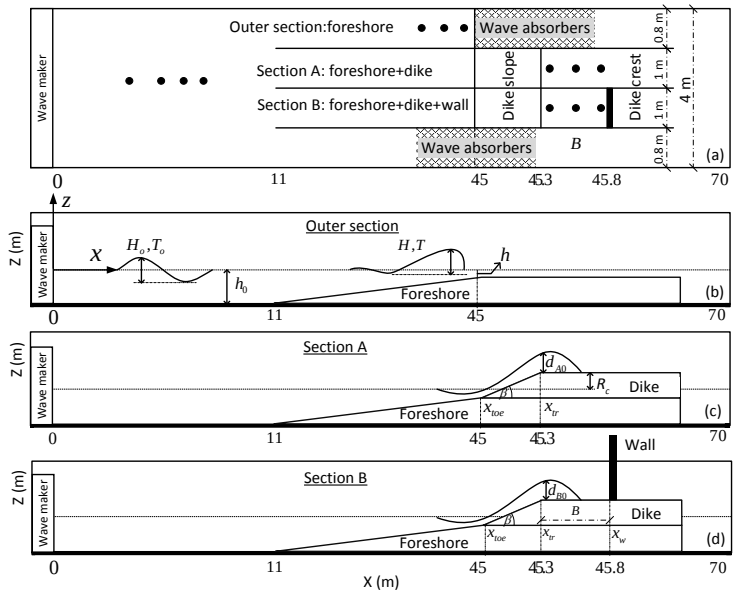

Figure 3.4: Wave flume in Flanders Hydraulic Research (Antwerp, Belgium). (a) is a top view of the flume, (b), (c) and (d) are the respective sections: 'outer section', A and B.

Two different dike slopes of $\cot\beta = 3$ and $\cot\beta = 6$ were tested which covers a typical range of coastal dike slopes representative for low-lying countries, see Schüttrumpf and Oumeraci (2005). For the steep slope ($\cot\beta = 3$), tests were conducted with $B = 0.25$, 0.5 and 0.75 m to investigate the spatial effect of overtopping wave impact force. For the gentle slope ($\cot\beta = 6$), only $B = 0.5$ m was tested. The foreshore slope was 1:35 and dike height 0.1 m. The foreshore slope created a depth-limited condition for incident waves and thus only two still water depth $h_0 = 0.96$ and 1 m were tested.

In order to calibrate the empirical formula proposed in Section 2, which is derived from the overtopping process of a single wave, the test program was restricted to regular waves only. The ranges of the parameters varied in the tests are listed in Table 3.1 and

Table 3.2. The symbols in the tables are illustrated in Fig. 3.4. For each water depth, regular waves with offshore wave steepness (H_0/L_0) from 0.003 to 0.021 were generated. This leads to the incident waves breaking on the foreshore slope. The resulting broken wave (bore) heights at the dike toe are within a range of $H = 0.03 - 0.1$ m in model scale.

Table 3.1: Ranges of structure dimensions for dike model

R_c (m)	$\tan\beta$ (-)	B (m)	R_c/B (-)
0.012;0.052	1:3	0.25; 0.5; 0.75	0.016; 0.21
0.012;0.052	1:6	0.5	0.024; 0.1

Table 3.2: Ranges of wave conditions

h_0 (m)	h (m)	H_0 (m)	T_0 (s)	H (m)
0.96; 1	0.05; 0.09	0.1; 0.2; 0.3	3; 4; 5	0.04-0.076
T (s)	ξ_0	H/h	R_c/H	h/L
3-5	2.3-10	0.6-1.1	0.16-1.3	0.01-0.025

The key parameters investigated include incident wave height near the toe of the dike H, incident wave period near the toe of the dike T, overtopping wave depth near x_{tr}, d_{A0} in Section A and d_{B0} in Section B. All these parameters were measured directly or indirectly by wave gauges. Home-made resistance type wave gauges recorded the water surface elevation at a sampling rate of 20 Hz throughout the entire duration of 80 seconds in each test. The number of waves per test varied between 10 and 15, depending on the input wave period. These short test durations avoid the influence of lacking active wave absorption. The locations of measured wave or flow surface elevation can be found in Fig. 3.4 and Table 3.3, in which H_0 is offshore wave height and H is local wave height at the dike toe.

In total 118 regular wave tests were conducted and 39 unique tests. All of the tests with $B = 0.5$ m, $\cot\beta = 3$ and $h_0 = 1$ m were repeated at least 2 times. The test repeatability was investigated in a series of tests with the same configuration ($h_0 = 1$ m, $H_0 = 0.2$ m, $T_0 = 4$ s, $B = 0.5$ m and $\cot\beta = 3$) with 36 repeated test runs. Good test repeatability resulted in an averaged 0.24% standard deviation of overtopping wave depth d_{B0}. Based on the good repeatability and the limited test time, no extra repeated tests were done for other configurations. Therefore, the results of the present work are based on the evaluations of 39 different test runs.

3.3.2. WALL MODEL AND SETUP

The wall model consisted of two parts: a force-measuring portion and a fixed wall. The force-measuring portion consists of an aluminium plate of 1 cm thickness, supported by an aluminium framework. Narrow gaps (1 mm) separated the aluminium plate from the fixed wall. The wall part was made of PVC board, fixed into Section B. Two-load cells of model series Tedea-Huntleigh 614 were used to determine the total overtopping wave force with sampling rate of 1000 Hz, which were mounted with the aluminium plate. The geometry of the wall model, supporting framework and positioning of the load

Table 3.3: Locations of wave gauge group for steep slope tests

Wave measurement		
	Near wave maker	x (m)
	H_0	7.85
		8.45
		9.32
		10.42
	Outer section	x (m)
	H	44.96
Flow depth measurement		
	Section A	$x - x_{tr}$ (m)
	d_{A0}	0.025
	Section B	$x - x_{tr}$ (m)
	d_{B0}	0.025

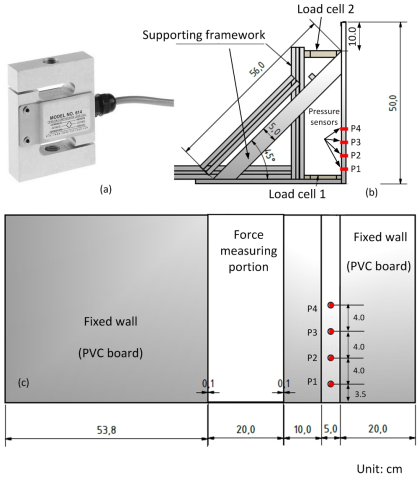

Figure 3.5: Wall model and force measuring system including (a) load cell (b) positioning of load cells and supported frameworks and (c) front view of wall model and locations of pressure sensors

cells are shown in Fig. 3.5. Next to the force-measuring portion, four pressure sensors were mounted on the face of the wall. They are sampled at a rate of 1000 Hz in order to detail the local pressure evolution and to help understand the impact mechanism of the overtopping wave. The lowest sensor (P_1) was mounted 3.5 cm above the dike crest and the space between each two sensors' center was 4 cm.

3.3.3. DATA PROCESSING PROCEDURES

INCIDENT WAVE CONDITION

After the experiments, the wave and force data were processed. Firstly, incident wave height (H) and period (T) at the dike toe were extracted from the wave surface elevations

collected by the wave gauges installed at the dike toe in the outer section, using the zero-down-crossing method.

OVERTOPPING FLOW DEPTH

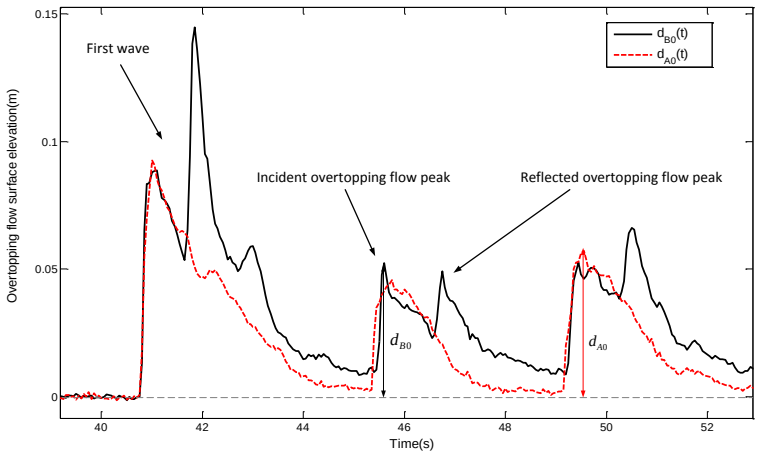

Figure 3.6: An example of overtopping wave surface elevation near the edge of dike crest, 2.5 cm to x_{tr}.

The peaks of overtopping wave depth along the dike crest in both Section A and Section B were picked from the time series of the flow surface elevation. Fig. 3.6 illustrates an example of time series of overtopping wave surface elevations in both of Section A and B. The dashed line indicates the flow time series in Section A and the solid line indicates that in Section B. Due to the reflection from the wall, the overtopping wave in Section B shows a two-peak time series signal (e.g., incident flow peak and reflected flow peak). Only the incident flow peak (the $d_{A0_{max}}$ and $d_{B0_{max}}$) is chosen for further analysis. The subscript "A" refers to Section A and "B" to Section B. For convenience, the subscript "max" was removed from the maximum flow depth yielding d_{A0} and d_{B0} in this study. As the first wave generated is higher than the subsequent ones, which doesn't represent a wind-wave overtopping event, see Fig. 3.6. Thus, the first overtopping event was removed from the processed database. The final data of d_{A0} and d_{B0} used for analysis were the averaged value from three overtopping waves which gave the largest three total impact loads on the wall of each test.

FORCE DATA

The signals of the load cells were digitally filtered. A cut-off frequency of 50 Hz was chosen for the load cells, in order to keep the characteristics of force signal and at the same time reduce noise. The forces measured by load cells are compared with the integrated forces from the pressure sensors, see Fig. 3.7a. The two-peak force signal of a single impact event was observed. The first peak is called dynamic impact force and the second one is called quasi-hydrostatic force. The second peak is generally higher than the first peak in the low frequency force measurement, thus most important for the overall stability of large structures like houses and walls. Therefore, the analysis focuses on the

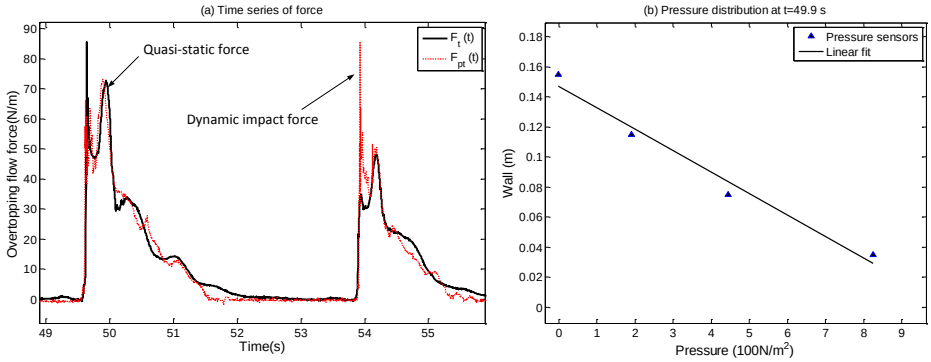

Figure 3.7: An example of overtopping wave force measurement. (a) a comparison of flow force (F_t) by load cells (straight line) and flow force (F_{pt}) by pressure sensors (dashed line). F_{pt} is obtained by integrating the raw pressure data following the method of Ramachandran et al. (2012). (b) pressure distribution at $t = 49.9$ s.

second peak. Pressure sensors work well for the first peak with short impact duration, and both the pressure sensors and load cells give a similar good performance on the quasi-hydrostatic force measurement. Also the large force inferred from the pressure sensors is probably due to the fact that a local high pressure is attributed to a large area. Fig. 3.7b illustrates the linear pressure distribution at the moment $t = 49.9$ s, which provides a proof of quasi-hydrostatic nature of the second peak force. Furthermore, the data of maximum total impact force F_t were determined by averaging the values of the three highest measured quasi-hydrostatic forces of each wave train by load cells. Based on the measured hydrostatic pressure at the time of occurrence of the second force peak, the point of application of the measured force will be at a distance of $z_a = \frac{1}{3}\sqrt{2F_t/\rho g}$ from the bed. The localized flow impact mechanism and its dynamic impact force are not included in the current chapter.

3.4. RESULTS

3.4.1. DETERMINE THE UNOBSTRUCTED FLOW DEPTH d_{A0}

In the current study, the incident wave breaks on the foreshore, the resulting broken wave continues running up to dike slope and generating the overtopping wave. The range of the calculated ξ_0 is from 2.3 to 10. A regular wave run-up formula R_u proposed by Schüttrumpf (2001) was applied which covered a wide range of ξ_0 from 0.9 to 9.6.

The measured unobstructed flow depth d_{A0} was compared with Eq. (3.13), and the authors get

$$d_{A0} = 0.77H\left[1 - \frac{R_c}{R_u}\right], \tag{3.15}$$

where $R_u = 2.25H\tanh(0.5\xi_0)$. 0.77 is the empirical coefficient α_2 in Eq. (3.13), determined by fitting measured d_{A0} with $H(1-R_c/R_u)$. Fig. 3.8 plots the estimates of overtopping wave depth in Section A with the measurements. Eq. (3.15) works well for providing the good trend but with much scatter. Some of the scatter was caused by the limitation

of the measurement using wave gauges, whereas some of it came from the choice of α_2. A further discussion on α_2, is given in Section 3.5.

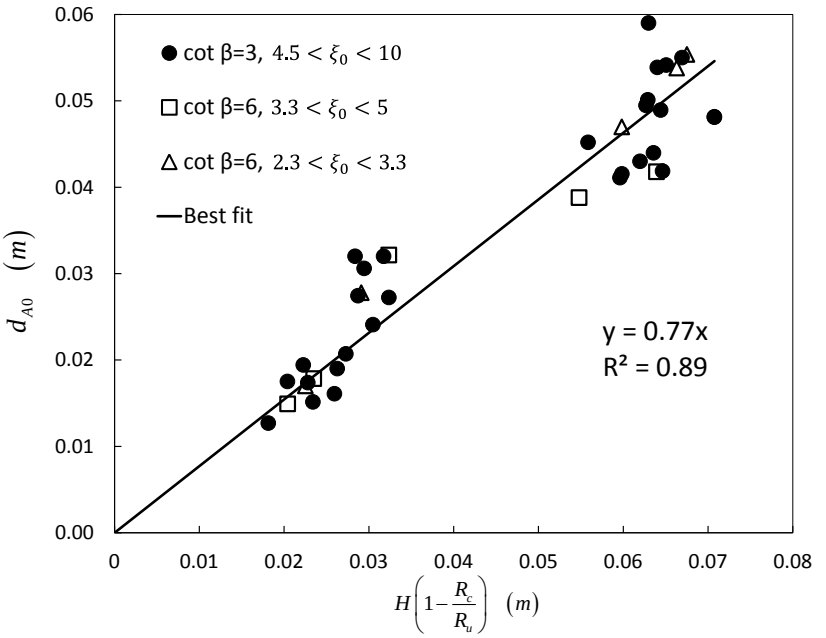

Figure 3.8: Measured d_{A0} versus Eq. (3.13) with $\alpha_2 = 0.77$.

3.4.2. DETERMINE FLOW DEPTH CONSIDERING THE ABSENCE OF WALL

Since d_{A0} is commonly used with the assumption of no wall on the dike, the authors defined a coefficient C_{tr} to correlate the unobstructed flow depth (d_{A0}) and obstructed flow depth (d_{B0}) by considering the influence of the wall,

$$d_{B0} = C_{tr} d_{A0}. \tag{3.16}$$

where C_{tr} is obtained experimentally. In the present study, d_{A0} was measured at 2.5 cm behind x_{tr} in Section A, and d_{B0} was measured at the same location but in Section B, see Fig. 3.6. Fig. 3.9 shows the comparison of the results d_{B0}/d_{A0}, and an empirical formula for C_{tr} given by the best-fit curve,

$$C_{tr} = 0.33 \cdot ln\left(\frac{B}{L}\right) + 1.86. \tag{3.17}$$

In Fig. 3.9, even though there is a lot of scatter, an interesting trend is observed: C_{tr} crosses two regions: $C_{tr} < 1$ and $C_{tr} > 1$. When $C_{tr} < 1$, it indicates that the d_{B0} would be overestimated by using d_{A0} to predict F_t. It is a fact that the effective overtopping water mass contribution to the impact process is a function of the relative location of the wall

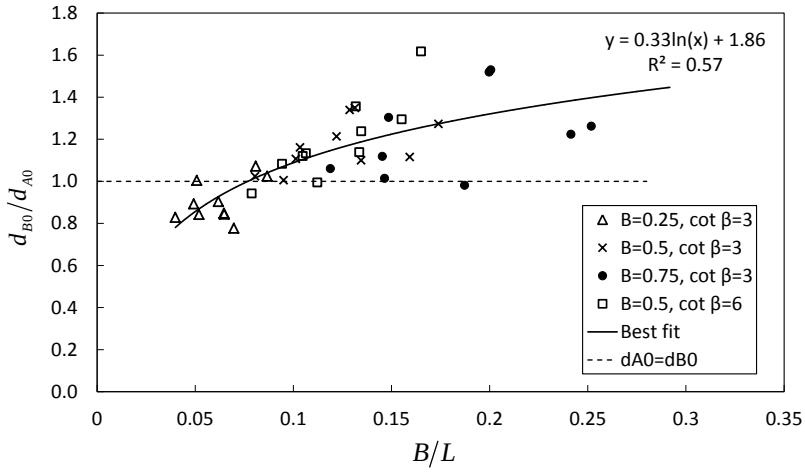

Figure 3.9: Influence of wall on initial overtopping wave depth, d_{A0} is measured at 2.5 cm behind x_{tr} in Section A and d_{B0} is measured at the same location but in Section B.

B/L. Only part of overtopping wave of one overtopping event will finally impact on the wall. And when $C_{tr} > 1$, d_{B0} would be underestimated by using d_{A0} to predict F_t because of the residual water layer left by the previous overtopping event which would increase the level of d_{B0}.

3.4.3. DETERMINE OVERTOPPING MOMENTUM FLUX

In this section, the empirical coefficients (e.g., C_5, $f(\beta)$, and λ_1) as proposed in Eq. (3.12) for the maximum total impact force F_t are determined by fitting the equation to experimental data.

Fig. 3.10 shows the results from $\cot\beta = 3$ with three different boulevard widths B (from x_{tr} to x_w). d_{B0} is measured at 2.5 cm behind x_{tr} in Section B. From the best-fit curve, 4.9 represents the factor $C_5 f(\beta)$ and 8.86 represents the factor λ_1 with a regression coefficient $R^2 = 0.84$. There is some scatter mainly for the case $B = 0.25$ m. A reasonable explanation is that the wall is located within or close to the transition zone, where the characteristics of the overtopping wave are complex, see Fig. 3.2b.

Data of slope $\cot\beta = 6$ is compared with those of slope $\cot\beta = 3$ for the same $B = 0.5$ m, shown in Fig. 3.11. The solid squares indicate the tests of $\cot\beta = 3$ and the open squares indicate the tests of $\cot\beta = 6$. It is found that a gentle slope gives a smaller overtopping wave load comparing to a steep slope when B/L is between the range of 0.1 to 0.15 in accordance with finding by Pedersen (1996).

Table 3.4 shows the results of empirical coefficients for both dike slope tests. Subsequently an empirical dike slope function $f(\beta) = \cot\beta$ and $\lambda_1 = \lambda_2 \cot\beta$ can be determined based on the results shown in Table 3.4, where λ_2 is an empirical coefficient. Then the proposed overtopping wave load relationship given by Eq. (3.12) can be fitted to the test results for slopes $\cot\beta = 3$ and 6 with the dike slope function $f(\beta) = \cot\beta$, see

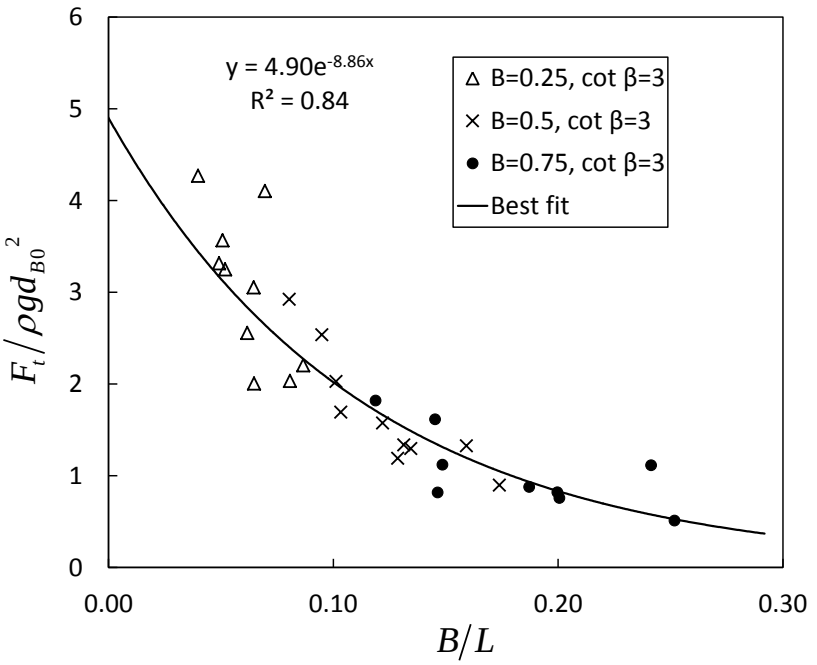

Figure 3.10: Test results for $\cot\beta = 3$.

Table 3.4: Results of λ_1 and $c_5 f(\beta)$ for $\cot\beta = 3$ and 6

$\cot\beta$	3	6
λ_1	11.41	20.3
$C_5 f(\beta)$	6.43	12.63
R^2	0.85	0.92

Fig. 3.12. A best-fit of Eq. (3.12) to the overtopping wave data leads to:

$$\frac{F_t}{\rho g (d_{B0})^2} = 1.7 \cot\beta \exp(-3.08 \cot\beta \frac{B}{L}) \tag{3.18}$$

where (1.7 $\cot\beta$) represents the empirical function $C_5 f(\beta)$ and (3.08 $\cot\beta$) represents the decay coefficient λ_1 in Eq. (3.12). Note that the dike slope function $f(\beta) = \cot\beta$ is determined empirically in the present study, so it is only applicable for the range of $\cot\beta = 3-6$. A discussion on the dike slope function will be provided in Section 3.5.

For practical reasons, d_{B0} used in Eq. (3.18) is not obtainable if there were no wall present on the dike. Thus, there is a limitation of using Eq. (3.18) to predict F_t at specific locations on the dike. Therefore, including C_{tr} to correct d_{B0}, a final equation can be written as:

$$\frac{F_t}{\rho g (d_{A0})^2} = 1.7 C_{tr}^2 \cot\beta \exp(-3.08 \cot\beta \frac{B}{L}). \tag{3.19}$$

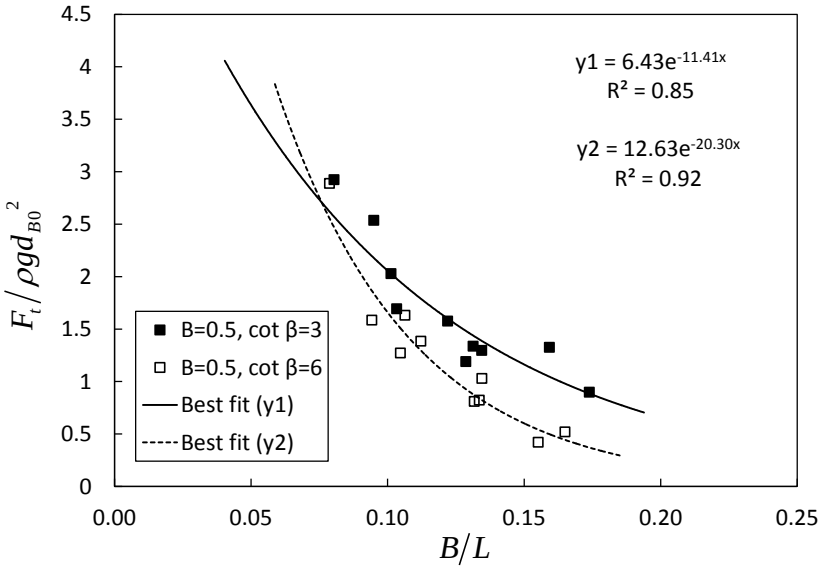

Figure 3.11: Test results of different dike slope for the same $B = 0.5$ m condition: solid square indicates the case for $\cot\beta = 3$ and hollow square indicates the case for $\cot\beta = 6$.

The predicted force (F_{cal}) using Eq. (3.19) is compared with the measured F_t, showing a good performance with a regression coefficient $R^2 = 0.95$, see Fig. 3.13.

Finally the authors use Eq. (3.15) and Eq. (3.19) to estimate the overtopping wave force, shown in Fig. 3.14. A qualitative comparison between Fig. 3.13 and Fig. 3.14 shows an increased scatter with substituting Eq. (3.15) into Eq. (3.19) as shown in Fig. 3.14, compared to the good performance of Eq. (3.19) by using measured d_{A0} shown in Fig. 3.13.

3.5. DISCUSSION

Prior work has documented the characteristics of overtopping waves on a dike (e.g., flow depths, flow velocities and discharges) and the impacts of bore-like waves on a vertical wall (e.g., broken wave impact on a rubble mound breakwater and tsunami bore impact on a wall). However, these studies have been lacking either direct relevance to describe the overtopping wave load or similar configurations.

In this chapter, a simple formula for overtopping wave load on a vertical wall placed on top of a wide crested impermeable dike was derived, based on two arguments: one: is the weight of water contained in the upper part of a run-up wedge above the dike crest level is proportional to the initial maximum depth-integrated overtopping momentum flux, and the other: the overtopping momentum flux is following an exponential decay. A slope function and two key coefficients were determined by physical model tests using regular waves.

The overall satisfactory performance of the proposed crude formula for the measurements, demonstrates that applying the maximum depth-integrated wave momentum

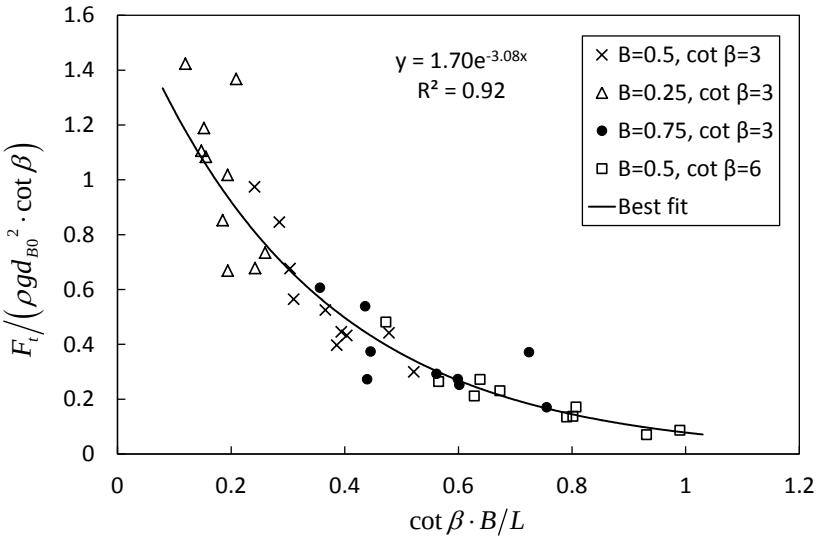

Figure 3.12: Test results of different dike slopes and different B with considering dike slope function $\cot\beta$.

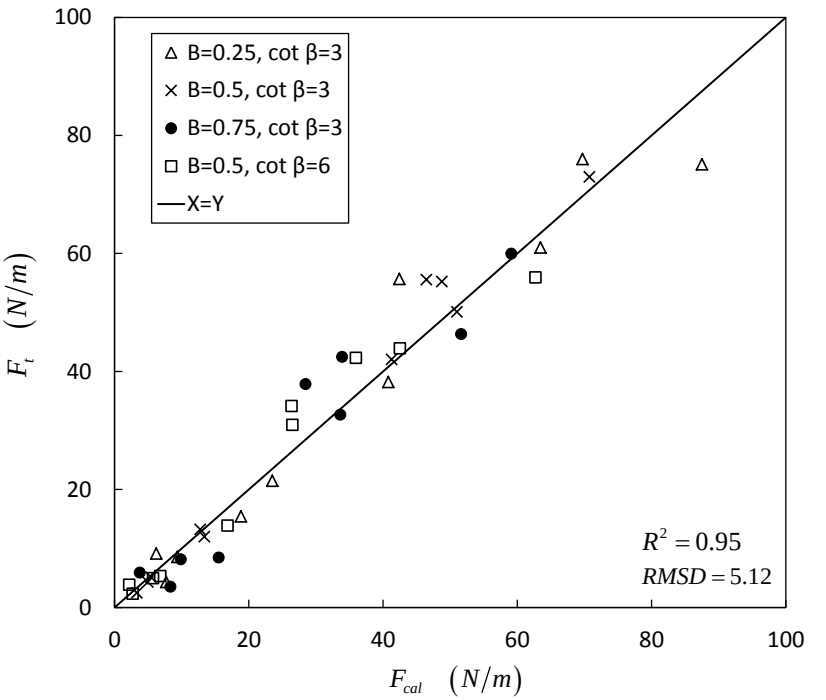

Figure 3.13: Measured F_t versus Eq. (3.19).

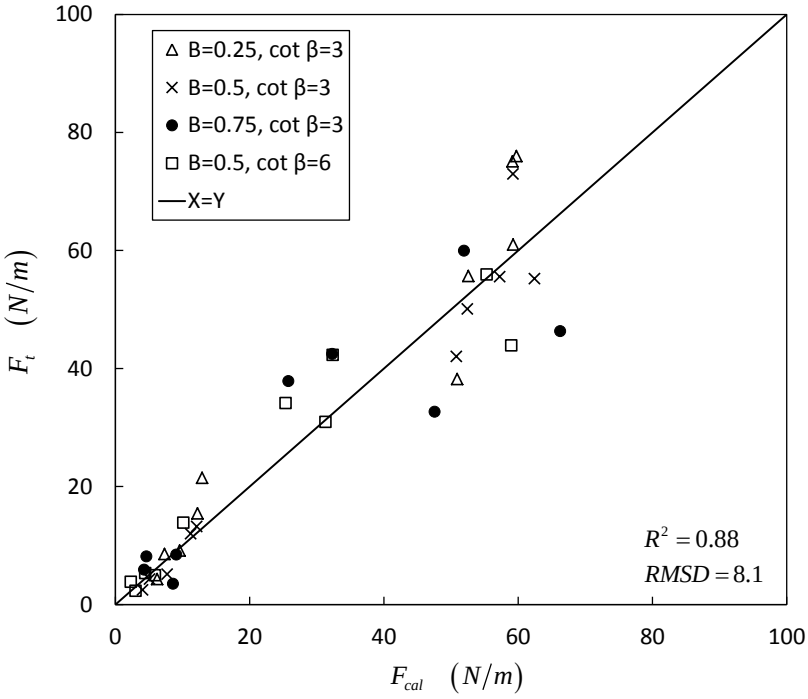

Figure 3.14: Measured F_t versus predicted flow force using Eq. (3.15) and Eq. (3.19).

flux method proposed by Hughes (2004b) for overtopping wave. The author also defined a transition zone at the beginning of the dike crest and a decay zone. The former one is used to connect the wave run-up zone with the latter one. The overtopping wave in the decay zone is assumed similar to a progressive wave, and is following an exponential decay shape. This exponential decay shape of the predictive formula is in good agreement with the spatial distribution of the overtopping discharges, see Pullen et al. (2007). From the results, the authors found that there is much scatter for the tests with a smaller value of B/L for $\cot\beta = 3$ condition. This could suggest the differences of flow characteristics between the transition zone and the decay zone; Meanwhile Fuchs (2013) reported the importance of the dike slope for the overtopping wave features near the beginning of the dike crest, but not far inland. This gives a reasonable proof of the classification of the two zones. However more work still needs to be done to confirm the boundary between the transition and the decay zone in the future.

The overtopping momentum flux ($M_{F_{ov}}$) introduces an empirical dike slope function $f(\beta)$ to the overtopping wave load formula with a physical relevant meaning. Though Hughes (2004a) has already established a series of empirical slope functions for the run-up height of regular waves, irregular waves, and solitary waves, it is still lacking for regular broken waves. Interestingly, Hughes' (2004a) dike slope function for regular wave run-up height contains a simple term of $\tan\beta$, and it works well in a wide range of $\cot\beta = 2-10$. The overprediction for the case with $\cot\beta < 2$ indicates the limitation

of using the argument of the triangular shape of water wedge for a steep dike, because the run-up water surface is not straight, but concave (Hughes, 2004a). In the present study, the empirical slope function was determined in terms of $\cot\beta$, and was covering the range of $\cot\beta = 3-6$. This is in line with the basic shape of Hughes'(2004a). Therefore, the dike slope function in the present study is reasonable, and could be expanded to the range of $\cot\beta = 2-10$, but still needs to be confirmed. Herein, the authors would like to note that the dike slope function contains the dike slope β and the run-up water surface angle θ. The reason of empirically determining $f(\beta)$ is the difficulty of estimating the run-up surface angle θ. Yamamoto and Horikawa (1992) proposed a method for estimating θ, which depends on the incident wave steepness and dike slope. Yamamoto and Horikawa's (1992) θ function provides a potential of combining Hughes'(2004a) work to develop a uniform empirical dike slope function for different wave types in future studies.

In the present study, the dike slope function $f(\beta)$ was introduced in the decay coefficient λ_1 of the proposed overtopping wave load formula. The final load formula including $f(\beta)$ in the decay coefficient fits the experimental data well. In order to explain this good fit, a simple physical argument of the exponential decay function is given. A classical exponential decay function contains two constant terms, one is an initial quantity and the other one is a constant decay coefficient. The ratio of these two constants determines the uniqueness of an exponential decay function. In the present study, the initial amplitude of the proposed exponential function for overtopping wave load includes a dike slope function, left hand side of Eq. (3.12). The incident wave conditions were the same for different dike slope tests, and the position of the dike toe was kept constant in Section A and B. Thus it is reasonable to include the same dike slope function in the decay coefficient λ_1 in Eq. (3.12).

From the test results, the gentle slope reduces the overtopping wave load which is in line with the observations from Pedersen (1996). This reduction is expected, due to the longer travel distance of overtopping waves along the gentle slope which causes more energy loss. Whereas from the decay coefficient point of view, a gentle slope gives a faster drop of the overtopping wave load.

In this study, the initial overtopping wave depth measured in Section B (with a wall) was used to develop the flow load formula. Considering the effect of the wall on the overtopping wave features, and the availability of an overtopping wave depth formula in literature, a coefficient C_{tr} was defined to correct the obstructed overtopping wave depth in Section B. If the wall is too close to the seaward edge of dike crest, the real overtopping wave volume in front of the wall would be overestimated in comparison with the situation without considering the wall, whereas it would be underestimated with ignoring the water volume still present from the previous overtopping wave. Though the scatter of C_{tr} weakens the performance of the proposed overtopping wave load formula, it provides a reasoning to consider the effect of the wall on the flow load. Increased scatter shows up when B/L is larger than 0.15. It is undoubtedly caused by the variation in the overtopping wave depth measurement when the reflected flow collides with the successive flow near the position of wave gauge.

When estimating the initial overtopping wave depth by using local wave conditions, an empirical coefficient $\alpha_2 = 0.77$ was used for both dike slopes of $\cot\beta = 3$ and 6. Ya-

mamoto and Horikawa (1992) proposed a theoretical equation for α_2, and verified it by some experiments and field measurements. When comparing the α_2 value obtained in the present study with that of Yamamoto and Horikawa (1992), $\alpha_2 = 0.77$ agrees well with Yamamoto's theoretical value for $\cot\beta = 3$, but overestimates his theoretical value for $\cot\beta = 6$. But the theoretical value of α_2 underestimates their measurement when the dike slope is gentle ($\cot\beta = 6-10$). Yamamoto's measured data points lie scattered above the theoretical curve, but have an upper limit around 0.8, which is close to 0.77 for $\cot\beta = 6$ in this study. Note that the obtained $\alpha_2 = 0.77$ currently is only compared with what is calculated or measured within a similar range of wave steepness. Therefore, for estimating the initial depth of overtopping wave induced by a broken wave, Yamamoto and Horikawa's (1992) method is recommended (Martin et al., 1999), and with $\cot\beta = 3-6$, $\alpha_2 = 0.77$ is suitable for an impermeable dike slope. The authors would like to point out that Eq. (4) and (7) of Schüttrumpf and Oumeraci (2005) also work well for the prediction of d_{A0} in this study, but Eq. (3.15) is relatively simple.

When comparing to a hydraulic bore generated by a dam-break approach, there is no well-defined equivalent depth (a_0) for the wave overtopping situation to describe the flow characteristics (Ryu et al., 2007). Only limited research work has been reported to make the connection between these two types of flow/wave. Ryu et al. (2007) found that dam-break flow theory can be used to predict the overtopping wave field on a ship deck in deep water, and pointed out that the importance for the application is to determine the a_0 for the overtopping wave. However, their a_0 was determined empirically by one wave height in deep water condition, which doesn't work for the current situation. The authors think similarity exists between the dam-break wave and overtopping wave within the decay zone ($Zone_{de}$) in Fig. 3.2. The proposed empirical formulas in this paper aim to give a solution for overtopping wave using wave conditions at the dike toe. Therefore, the proposed empirical formula can't be directly used for the hydraulic bore, for example just assuming $a_0 = d_{A0}$.

3.6. CONCLUSIONS

In this chapter, overtopping momentum flux was used to develop an empirical formula to predict overtopping wave load. The proposed empirical formula Eq. (3.19) was verified by experimental data, demonstrating good performance. A dike slope function $f(\beta)$, a correction coefficient for obstructed flow depth C_{tr}, and an initial overtopping wave depth coefficient α_2 were determined by experiments. These empirical coefficients allowed for an interpretation of the overtopping process of a broken wave from dike toe up to the front of wall on the dike. In this chapter, the work only focused on a single overtopping wave in a series of regular waves. In the following chapter, more work were carried out by other types of waves (e.g., random waves) to investigation the influence of the interaction processes within a wave group on the overtopping wave load. These would give an insight the occurrence of extreme overtopping events and impact loads, improve the formulation for C_{tr} with a wider parameter range or statistical values, and provide statistical tools for the extreme load prediction.

4

EXTREME OVERTOPPING WAVE FORCE

The impact force induced by waves overtopping a dike with a shallow foreshore and a vertical wall on its crest, was studied. To this end, physical model tests with irregular waves were performed in a wave flume at a typical scale of 1:25. The goal of this study was to develop a method to estimate the maximum forces on the wall during a known storm peak. The time series of water depth at toe of the dike, flow thickness at seaward edge of the dike crest and impact forces were measured. An empirical Generalized Pareto distribution is verified as the best distribution to characterize the extreme overtopping wave forces.

This chapter is based on: Chen, X., Hofland, B., Uijttewaal, W. (2016). Maximum overtopping forces on a dike-mounted wall with a shallow foreshore. Coastal Engineering 116, 89-102.

4.1. INTRODUCTION

Many low-lying coastal towns are protected by defence structures (e.g., seawalls and dikes). Urban development along the waterfront is attractive, although the space is restricted. For example, the residential and commercial developments along UK and Mediterranean shorelines are just behind the seawall (Allsop et al., 2008); Whereas, the development in Belgium and the Netherlands typically is on the top of a sea dike (Van Doorslaer et al., 2015), see Fig. 4.1 (a). Due to climate change and sea level rise, violent storms are expected which would aggravate the coastal flooding risk. The buildings and people within these densely populated waterfront areas would experience significant impacts from overtopping waves induced by the storms (see Fig. 4.1 (b)). However, users and owners of the waterfront buildings may be unaware of the potential threats (Allsop et al., 2008).

The coast of the Netherlands and Belgium is characterized by very shallow water foreshore in the front of the coastal dike to dissipate the incoming wave energy (Verwaest et al., 2010). Recent studies reveal that the shallow water environment may contribute to the generation of infragravity waves. The combination of large waves and infragravity waves would resulting in the exacerbation of the coastal flooding during strong storms (Suzuki et al., 2012). This flooding mechanism is expected to occur, but not brought to the forefront until the super typhoon Haiyan hit the Philippines on early November 2013 (Roeber and Bricker, 2015). The coastal town of Hernani in Philippines with coral reef in the front was reported struck by a destructive long-period tsunami-like wave with an extreme damage. The mechanism of this significant damage has never been accounted for before (e,g., Shimozono et al., 2015; Roeber and Bricker, 2015), because a coral or artificial reef is normally seen as a protection of the tropical coastal areas against flooding and erosion by dissipation wave energy (Ferrario et al., 2014). Based on the field survey and numerical modeling afterwards, Shimozono et al. (2015) and Roeber and Bricker (2015) published their new results to indicate the tsunami-like wave in Hernani is the result of a superposition of the infragravity wave and sea-swell components (Shimozono et al., 2015) or surf beat generated during the wave breaking process (Roeber and Bricker, 2015). Through the further understanding of the damage caused by typhoon Haiyan, a coral or artificial reef can exacerbate the damage during large storms (Quataert et al., 2015; Roeber and Bricker, 2015). This suggestion is in line with the potential extreme coastal flooding of Belgian and Dutch coast with a shallow foreshore. Therefore, to evaluate the wave overtopping impact induced by the combined large wave and infragravity waves on waterfront buildings has become more interesting and important.

The literature and design guidelines for coastal structures mainly focus on the impact of non-breaking and breaking waves on vertical seawalls or breakwaters, and on the statistic distribution of the impact forces (Oumeraci et al., 2001; Cuomo et al., 2010a, 2011, et al). Only few studies on broken wave load have been done by Martin et al. (1999) and Nørgaard et al. (2013) in both deep water and shallow water condition. Oumeraci et al. (1993) and Martin et al. (1999) compared the differences of the impact force evolution shape and mechanisms caused by non-break waves, breaking waves and broken waves. In which, broken wave impact is believed to represent the impact of an overtopping wave. However, most of the studies of broken waves are especially for the design of rubble mound breakwater crown wall (Pedersen, 1996; Martin et al., 1999; Nørgaard

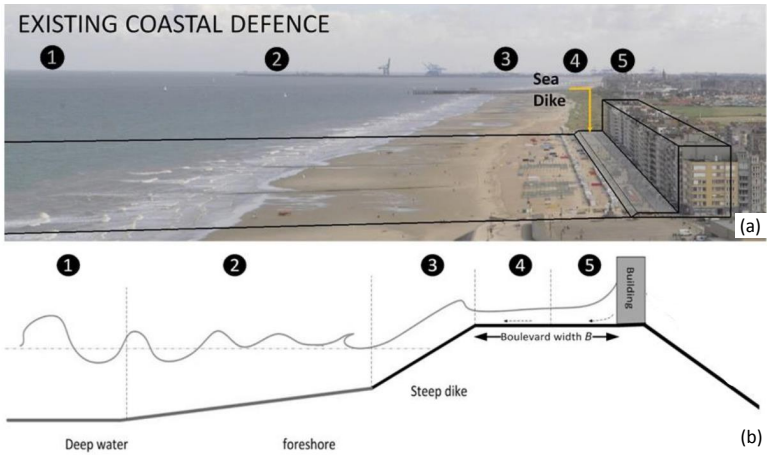

Figure 4.1: (a) An example of a coastal dike with buildings on top (Wenduine, Belgium); (b) Sketch of an overtopping impact process. The whole process of overtopping flow impacting on the building, adapted from Chen et al. (2015): ① Wind generates waves far away from shoreline; ② Offshore waves coming into the shallow foreshore area, increasing wave height, decreasing wave length. Finally, most waves breaking and wave energy dissipating in the form of turbulence bore. ③ Turbulent bore (broken wave) running up on the seaward slope of a dike and overtopping the crest of the dike; ④Part of the overtopping flow continue propagating along the dike crest and the other part flowing back seaward; ⑤ Overtopping wave impacting on the building eventually.

.

et al., 2013), but not a vertical wall on a impermeable dike.

The most relevant research work on the topic of overtopping impact force carried out so far consists of the experimental model tests. Chen et al. (2012, 2014, 2015), De Rouck et al. (2012), Ramachandran et al. (2012) used regular waves and Van Doorslaer et al. (2012) used the overtopping simulator. The aim of these tests was to investigate the characteristics of the overtopping impact forces. A double-peaked evolution shape of a single impact force (e.g., 'dynamic impact peak' and 'quasi-static peak') is recognized and reported by the researchers mentioned above. The two-peak shape of overtopping force is similar to the proposed church-roof breaking wave impact by Oumeraci et al. (1993), but without the significant magnitude difference between the two peaks exhibited by the breaking wave. Chen et al. (2015) proposed an empirical formula to predict the quasi-static peak of the overtopping force, which decays exponentially along the dike crest. A certain relationships between the overtopping force and overtopping discharge and individual overtopping volume were investigated by Ramachandran et al. (2012) and Van Doorslaer et al. (2012), which bring a possibility of using the existing work of overtopping volume and discharge to predict the force. The studies mentioned above conducted by far have improved the understanding of the impact process of overtopping wave and the prediction of the single force, but still not enough. From the point of practical design, we are particularly interested in determining the maximum force which is expected to occur on the building during a given storm peak ($F_{max,exp}$). In order to answer such a design question, statistical study of the overtopping forces is needed, which can be used to develop a procedure to determine the expected maximum force for a given storm peak.

By far, the statistical studies of wave overtopping has been mainly focused on how to predict the representative significant or the maximum individual overtopping volumes and discharge based on a considerable laboratory work for both smooth gentle and steep slopes of dikes without vertical structures on the crest (e.g., Van der Meer and Janssen, 1995; Pullen et al., 2007; Hughes and Nadal, 2009; Victor et al., 2012; Hughes et al., 2012; Pan et al., 2015); and rubble mound breakwaters (e.g., Zanuttigh et al., 2013). They recommended the use of 2-parameter Weibull distribution family (one of the commonly used extreme value distributions) to estimate the individual overtopping volume, and an empirical shape parameter of Weibull distribution which is related to hydraulic condition and dike structure properties. A common procedure for defining the extremes is using the upper percentiles of the distribution of the individual overtopping volume, such as: Hughes et al. (2012) selected the upper 10% of the overtopping volumes; Victor et al. (2012) chose the 50% of the values; and Nørgaard et al. (2014) used the upper 30% and Pan et al. (2015) applied the full distribution. It seems that the choice of the upper percentiles of the distribution is arbitrary and non-consistent among different studies and depending on the specific settings. Moreover, most of the extreme overtopping volume studies made a subjective a priori choice of using Weibull distribution. Coles (2001) argues the non-necessity a priori judgment about the adoption and recommends to use the Generalized Extreme Value (GEV) distribution (contains three forms of distribution families: Gumbel, Frèchet and Weibull) and Generalized Pareto distributions (GP) to do the extreme value analysis. Based on these statistical works mentioned above, and the existence of the relationship between the overtopping forces and the individual overtopping volumes and discharges reported by Ramachandran et al. (2012) and Van Doorslaer et al. (2012), a similar statistic analysis would be performed to determine the maximum overtopping force during a certain storm peak duration. While for the wave impact forces for design purpose, F_{max}, $F_{1/250}$ and $F_{1\%}$ are commonly accepted and used for designing coastal structures, which are defined as the maximum force, the average value of the largest four forces, and 1% largest force of 1000 waves generated by laboratory test with a certain test duration (Cuomo et al., 2011).

The objective of this chapter is to define a reference statistical distribution that can be used to determine the expected maximum overtopping force for a specific design condition (e.g., specific wave characteristics and storm peak duration). Since the relevant knowledge on the subject is limited, a 1:25 physical model representing a typical waterfront situation in low-lying countries is employed. A foreshore in front of the dike creates a shallow water condition where most of the incoming waves break. A wall is placed on the dike with a certain distance to the seaward dike slope. Not each incident wave overtopping the dike will impact on the wall. Also the incident overtopping wave on the dike can be influenced by the reflected previous waves. Thus, the direct relationship between each individual peak force and each incident wave at the toe of the dike is discarded, but physical relations are still taken into account.

The chapter is organized as follows. First, a description of the physical model set-up to simulate the overtopping process under different wave conditions (also presented in Chen et al. (2015)), data processing procedure and experimental observations are given. Then, the result of selecting the best-fitting distribution to the dataset, and empirical formulas for the distribution parameters are presented. Finally, discussion and conclusion

are given.

4.2. PHYSICAL MODEL TESTS

4.2.1. TEST FACILITY AND PROGRAM

EXPERIMENT SET UP

The experiments were performed in a 4-m wide, 1.4-m deep and 70-m long wave flume at Flanders Hydraulic Research in Antwerp, Belgium. The wave flume was spilt into four sections, with the two inner sections are 1.1 m in wide, and the two outer sections are 0.8 m in wide, see Fig. 4.2. Passive wave absorption baffles were installed in the outer sections. The outer section without a dike was used to measure incident wave conditions; and Section B was used to measure the impact force of overtopping wave by installing a “wall" model. The shallow foreshore profile and the dike models were made of concrete and wooden plates respectively. The dike slope was set as $\cot\beta = 3$, the distance between the wall and seaward edge of dike crest were $B = 0.25$ m and 0.5 m, the foreshore slope is 1:35 and dike height is 0.1 m.

The “wall" model was fixed into Section B and integrated with a force-measuring portion in the central. Two-load cells of model series Tedea-Huntleigh 614 were used to determine the total overtopping flow force with a sampling rate of 1000 Hz. The lowest natural frequency of the “wall" is 150 Hz. The geometry of the “wall", supporting framework and positioning of the load cells are shown in Fig. 4.3. Next to the force-measuring portion, four pressure sensors were mounted on the face of the wall. Additional details can be found in Chen et al. (2015).

TEST CONDITIONS

The test series and the range of the parameters varied are listed in Table 4.1. The symbols in the table are illustrated in Fig. 3.4. The key parameters measured include: incident wave height $H_{m0,t}$ and wave period $T_{m-1,0,t}$ at the toe of the dike; the water depth at the toe of the dike h_t; the freeboard R_c; the width of the dike crest B and the breaker parameter $\xi_{m-1,0}$, which is calculated by using $T_{m-1,0}$ at the toe. Resistant type wave gauges were employed to record the water surface elevation at a sampling rate of 20-Hz throughout the entire tests. 22 irregular wave tests (JONSWAP, $\gamma = 3.3$) with different conditions (in total 88 tests including repetitions) were conducted. The repeated test runs were conducted by changing phase seeds number. The test series are classified into three cases: shallow water condition (S) when $1 < H_{m0,o}/h_t < 2$, very shallow water condition (VS) when $2 < H_{m0,o}/h_t < 4$, and very very shallow water condition (VVS) when $H_{m0,o}/h_t > 4$. Using the ratio of offshore wave height $H_{m0,o}$ and local water depth h_t to distinguish the shallow and very shallow condition is proposed by Van Gent (1999). However, the range of tested conditions $H_{m0,o}/h_t$ in Van Gent (1999) stops at 3. In this study, our range of $H_{m0,o}/h_t$ is up to 6. So we specified the tests with $H_{m0,o}/h_t > 4$ as very very shallow condition, see Table 4.1.

One of the limitations of the current experiment setup is that the long test duration with a serious overtopping condition would reduce the water level near wave paddle. This decrease would alter the generated waves. In order to avoid this influence, a limit of decreased water level was set as 0.003 m by restricting the running duration to 900 s

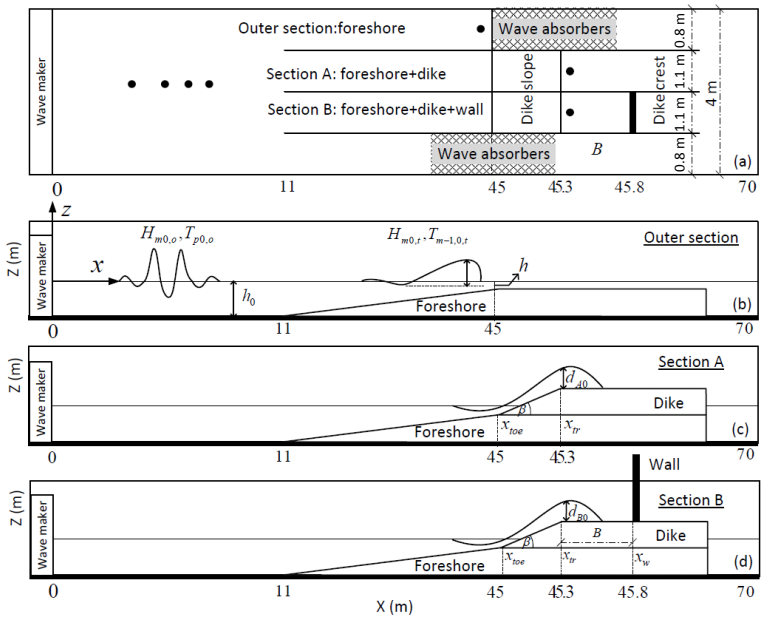

Figure 4.2: Wave flume in Flanders Hydraulic Research (Antwerp, Belgium). (a) is a top view of the flume, (b), (c) and (d) are the respective sections: 'Outer section', Section A and Section B (adapted from Chen et al. (2015)).

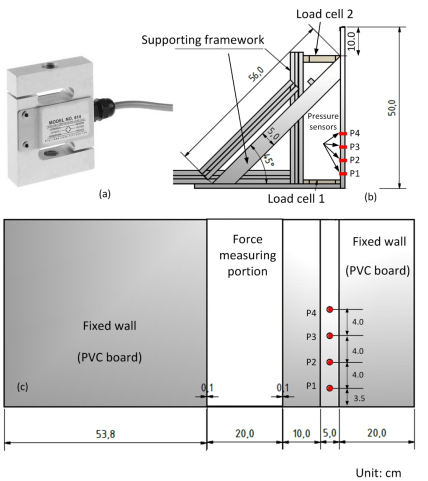

Figure 4.3: Wall model and force measuring system including (a) load cell (b) positioning of load cells and supported frameworks and (c) front view of wall model and locations of pressure sensors, adapted from Chen et al. (2015).

and 2400 s for different overtopping condition. These tests contain around 550 waves for the short tests and 1200 waves for the long ones. Romano et al. (2015) pointed out that at least 500 waves series can be used for overtopping tests with a comparable accuracy, and recommended 1000 waves series. Therefore, the test series in this study are acceptable. Another limitation is the first order wave generation in the flume and the lack of active absorption of long wave energy. For spurious long waves in the flume, it is found to be negligible due to relative large water depth at the wave generator and low steepness (Ottesen-Hansen et al., 1980; Shah and Kamphuis, 1996). A limited seiching mode was present in the flume, in the frequency range of 0.023-0.025 Hz, which is outside of the main frequency range of the infragravity waves in the flume. The full density spectrum, excluding this seiche band, was used to obtain the incident significant wave height H_{m0} and spectral wave period $T_{m-1,0}$. No increasing trend of the long wave energy was observed, thus the passive absorption system was found to be sufficient. The frequency resolution of the spectrum was 0.01 Hz for the long duration tests and 0.02 Hz for the short duration tests. For the very very shallow (VVS) cases (see Table 4.1), the averaged ratio of the seiche height $H_{m0,seich}$ to H_{m0} is 12%, which becomes significant. Thus the local water depth h_t of the VVS cases was corrected by adding half of the significant seiche height.

4.2.2. EXPERIMENTAL OBSERVATIONS

When water depth along a foreshore is shallow, the incident short waves on the foreshore force long (“infra-gravity") waves released from the short-wave groups in the shoaling and breaking process (Van Dongeren et al., 2007). This wave group propagation is observed in the current study. Fig. 4.4(a) and (b) show two examples of very shallow condition (test Jon003(4)) and very very shallow condition (test Jon012(4)) with the same input wave spectrum. The first two figures of each panel show the measured wave spectrum at offshore (close to wave generator) and the dike toe respectively. It can be seen clearly that the wave energy transfers into low frequency domain, which indicates that the water condition presented at the toe of the dike is shallow, and infragravity waves are expected. In this study, $T_{m-1,0}$ at the toe of the dike is used only as wave period parameter, which is highly relevant for characterize the low frequency wave motion near the shore (Van Gent, 2001). The third figure of each panel in Fig. 4.4 shows the time series of overtopping wave impact forces on the wall. Comparing the two cases (see Table. 4.1), it can be seen that the common large force peaks shown in the two figures occur at almost same time but with different magnitude, which suggests the relativeness of the occurred large forces and the incident wave groups.

For the very very shallow cases ($H_{m0,o}/h_t > 4$, see Table 4.1), the incident waves almost totally break either at foreshore or dike slope, then resulting a large "infra-gravity" wave. This large "infra-gravity" wave overtops the dike crest in a form of a single large turbulent bore, which gives an impact with a dominant quasi-static peak. This observation is highly similar to that observed from the work of Chen et al. (2015) by using regular waves. Whereas for the shallow and very shallow cases ($H_{m0,o}/h_t < 4$, see Table 4.1), the incident waves do not fully break before the overtopping process starts, which resulting in the short waves within a wave group overtop the dike crest and a group of impacts. Due to the interaction between subsequent overtopping waves within a group, the im-

Table 4.1: Test program

Test series	Repet.	Duration (s)	$H_{m0,t}$ (m)	$T_{m-1,0,t}$ (s)	h_t (m)	R_c (m)	B (m)	$\xi_{m-1,0}$ (-)	$\frac{R_c}{H_{m0,t}}$	$\frac{H_{m0,o}}{h_t}$	Case
Jon001	4	900	0.08	6.35	0.09	0.01	0.50	9.16	0.14	2.36	VS
Jon002	4	900	0.09	7.51	0.09	0.01	0.50	10.41	0.13	2.38	VS
Jon003	4	900	0.10	8.83	0.09	0.01	0.50	11.85	0.12	2.49	VS
Jon004	4	900	0.08	5.03	0.09	0.01	0.50	7.53	0.16	1.83	S
Jon005	4	900	0.08	5.94	0.09	0.01	0.50	8.66	0.15	1.85	S
Jon006	4	900	0.09	6.66	0.09	0.01	0.50	9.44	0.14	1.87	S
Jon007	3	900	0.08	4.40	0.09	0.01	0.50	6.58	0.15	1.26	S
Jon008	4	900	0.07	3.91	0.09	0.01	0.50	5.96	0.16	1.24	S
Jon009	4	900	0.07	3.33	0.09	0.01	0.50	5.18	0.17	1.23	S
Jon010	5	900	0.07	9.52	0.06	0.05	0.50	14.87	0.68	4.30	VVS
Jon011	9	900	0.08	11.04	0.06	0.05	0.50	16.38	0.60	4.34	VVS
Jon012	6	900	0.09	12.47	0.06	0.05	0.50	17.53	0.52	4.44	VVS
Jon013	2	2400	0.06	7.31	0.05	0.05	0.50	12.14	0.83	3.29	VS
Jon014	2	2400	0.07	8.10	0.05	0.05	0.50	13.08	0.78	3.27	VS
Jon015	1	2400	0.07	8.85	0.05	0.05	0.50	13.85	0.73	3.30	VS
Jon016	4	2400	0.05	5.19	0.05	0.05	0.50	9.39	0.98	2.23	VS
Jon017	4	2400	0.06	5.71	0.05	0.05	0.50	10.09	0.94	2.22	VS
Jon018	3	900; 2400	0.06	6.51	0.05	0.05	0.50	11.17	0.88	2.24	VS
Jon038	1	2400	0.07	11.60	0.04	0.07	0.25	18.91	1.04	6.78	VVS
Jon039	1	2400	0.07	12.82	0.04	0.07	0.25	19.64	0.91	6.84	VVS
Jon053	1	900	0.06	3.94	0.07	0.03	0.50	6.61	0.52	1.62	S
Jon054	1	900	0.06	4.42	0.07	0.03	0.50	7.30	0.50	1.59	S

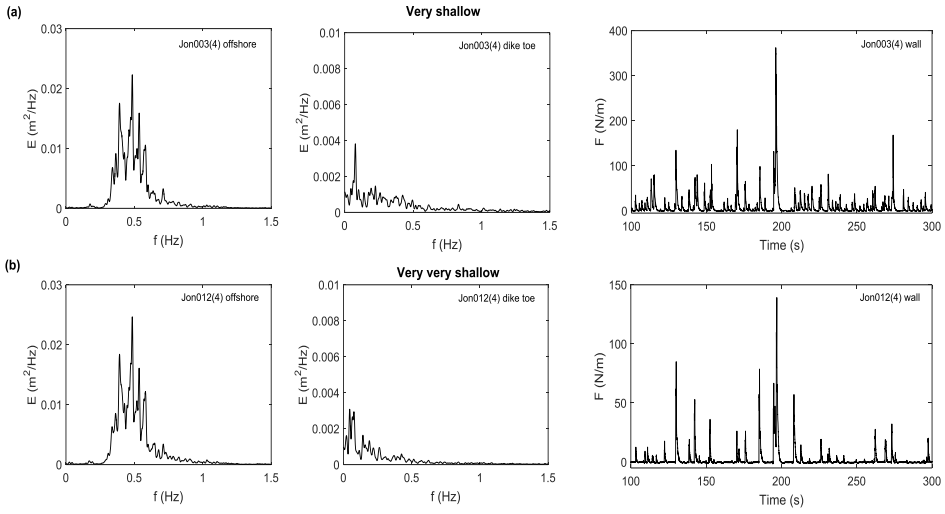

Figure 4.4: Examples of wave spectrum at offshore, toe of the dike and time series of overtopping wave force for very shallow condition (a), and very very shallow condition (b).

pact mechanism can be altered compared to the single impact event. Fig. 4.5 shows an impression of a frequently observed collision between a reflected initial wave and the incoming successive wave just in front of the wall of the tests with $H_{m0,o}/h_t < 4$. After the collision, the “new" combined wave approaches to the wall as a kind of impulsive breaking wave impact on a vertical wall (see Oumeraci et al., 2001). Fig. 4.6 (a) gives an example of the time series of the “impulsive" impact force of test Jon003(4), with an initial overtopping impact force starting at 830.5 s, and the successive wave impact at 831.4 s. As a comparison, Fig. 4.6 (b) presents the time series of the overtopping wave force of test Jon012(4), which represents a typical broken wave impact with dominated quasi-static force. Based on the comparison between these impact events, it is clear that the occurrence of the impulsive impact is also possible for broken waves. Similar wave motion within a wave group on a porous berm is also stated by Kamikubo et al. (2009). Both of the large bore impact and “impulsive" impact processes described in this section will cause extreme forces. Therefore, the distribution of the overtopping wave forces should be able to describe the extreme forces with different impact mechanisms.

4.2.3. DATA PROCESSING

The force measurement is important for this study. Two types of instruments were used to measure the overtopping force: one is load cell with a rigid system, and the other one is pressure sensor. Pressure sensors can capture the real dynamic impact with a short duration. However, the pressure sensors were installed along a vertical line only (see Fig. 3.5) which is the limitation of the current set-up. 3D effect caused by the air entrainment within the turbulent front of the overtopping flow would reduce the representative nature of the data measured by pressure sensors. The spacing between each two pressure sensors is large as well, the integration of the pressure data would result in

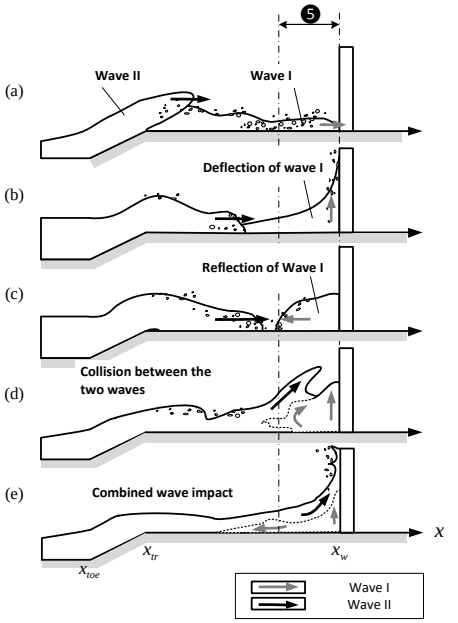

Figure 4.5: An example of the near wall collision in Zone 5. (a) the first overtopping wave I starts to impact on the wall, and the following wave II stars to overtop process; (b) the wave I deflects along the wall, and the following wave II propagates on the dike crest; (c) the reflected wave I runs into the wave II in front of the wall; (d) the reflected wave I is “pushed" back to the wall due to the collision between the two overtopping waves; (e) the combined wave impacts on the wall.

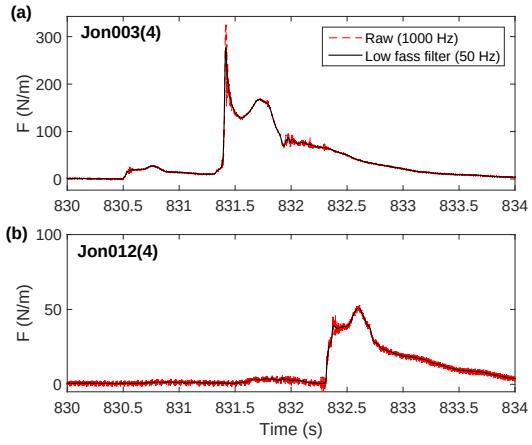

Figure 4.6: A comparison of types of impact force time series. Red dash line indicates the raw signals from load cell, and black solid line is the filtered one at a cut-off frequency of 50 Hz.

the overestimation of the impact forces. Therefore, only the data obtained from load cell would be used for further analysis while sacrificing accuracy of the short duration. In this section, the filtering process is introduced firstly; Then the method of choosing data sample for the further statistical analysis is presented.

FILTERING

As mentioned in the previous sections, an overtopping force signal consists of dynamic peak with a short duration, and the quasi-static force peak. The two peaks are caused by different mechanisms during the impact progress. For the first dynamic peak, the impact is influenced by the air entrainment within the turbulent overtopping flow, which would suffer from the 3D effect and scale effect (e.g., Cross, 1967; Chen et al., 2014). As for the quasi-static peak which follows the Froude scaling law, the scale effect can be neglected. In order to filter out the high frequency components from the background noise and the oscillation caused by the air entrainment, digital low pass filters with cut-off frequency at 50 Hz is applied with sacrificing some of the maximum peaks of the un-filter signal. Fig. 4.6 shows an example of the time series of impact forces from load cell before and after filtering. The natural frequency of a typical residential building (with a height of 3 to 50 m) is 1-8.7 Hz in prototype (5-43.8 Hz in model scale). The peak value due to low-pass filter is reduced about 10-20% for all cases. Therefore, choosing the cut-off frequency at 50 Hz is acceptable which can keep most of the characteristic of the time series of overtopping forces.

FORCE PEAKS

After filtering the force data from load cell signals, next step is to determine the force peaks for the further statistical analysis. The Peaks-Over-Threshold (POT) method is used to define independent force peaks (e.g., Caires and van Gent, 2008; Solari and Losada, 2012). For the impact forces with two peaks, only the largest one is selected to represent

the peak of this impact. In order to keep a consistency of choosing the individual and independent force peak for all the different test cases, an initial threshold with a value of $1/8\rho g H_{m0,toe}^2$ by using the form of the mean wave power (Goda, 2010) and a minimum time interval of 1.6 s (roughly an impact duration) are applied, see Fig. 4.7. When either the overtopping force peak is less than the calculated mean wave power at the toe, or the occurrences of the adjacent force peaks are shorter than 1.6 s, we consider them to be dependent, and they will be excluded from the data sample.

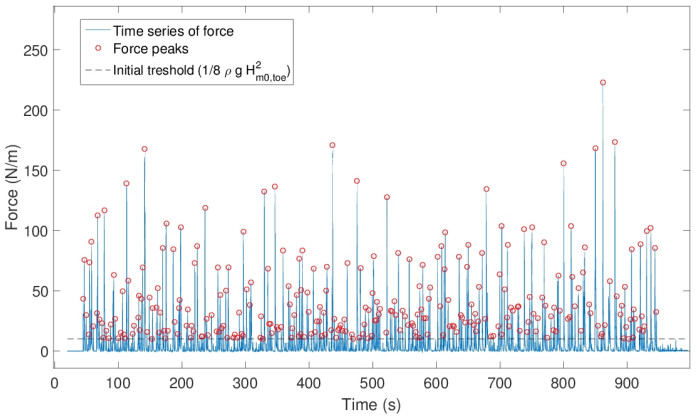

Figure 4.7: An example of force peaks above the initial threshold.

4.3. RESULTS

4.3.1. DETERMINATION OF EXTREME OVERTOPPING FORCE SAMPLE

Individual and independent overtopping force peaks (above the initial threshold) for all 88 tests were identified from the time series of the forces, after filtering and the peak selecting procedure. In this section, a high threshold is applied to identify the extreme, large values for the overtopping forces.

DEFINITION OF THE NUMBER OF INCIDENT WAVES

Due to the shallow water depth in front of the dike, the number of the incident waves is not easy to determinate. Herein, we define a representative incident wave number at the toe (N_{toe}) by using the ratio of the test duration and mean spectral wave period , based on the relevant $T_{m-1,0}$ of the low frequency waves, see Eq. (4.1):

$$N_{toe} = \frac{D}{T_{m-1,0}}. \tag{4.1}$$

where D is the duration of the storm peak (test duration).

DETERMINATION OF A HIGH THRESHOLD

A high threshold is needed because we are only interested in the extreme tail of the overtopping force distribution. Based on the reported empirical relationship between the

overtopping volume and forces (Van Doorslaer et al., 2012), Weibull is considered as the best fit distribution for individual overtopping volume. Hughes et al. (2012) determined the upper 10% of individual wave volumes gave better representation of the extreme tail of the overtopping volume distribution, while sacrificing accuracy in the lower volume range of the distribution. Therefore, the upper 10% percentile of the force peaks is selected as the high threshold for defining the extreme force sample, although such cut-off seems arbitrary and is especially problematic when the sample size is small, which is a well known dilemma (Mazas and Hamm, 2011). The selection of the threshold value will be discussed in Section 4.4.

OVERTOPPING FORCE IMPACT COEFFICIENT

In this study, we conducted 22 different test series, in total 88 tests (including repetitions). Due to the limitation of the test duration, the size of the sample is quite small. In order to obtain more reliable statistic analyses, the samples from each repetition of the same test series were combined into a new sample as the equivalent force of a signal that comes from one test with a long duration. All of the force peaks (e.g., F_i) of the dataset are considered. The size of the sample is N_F. Then the overtopping impact coefficient is defined as:

$$P_i = \frac{N_F}{N_{toe}+1}, \tag{4.2}$$

which means the proportion of the incident waves which will give impacts on the wall in total waves. Since only the extreme large impacts are interesting, 10% of P_i is used in this study as the overtopping impact probability with the expression of $P_{im} = 0.1P_i$. Thus based on Eq. (4.2), the sample size of the upper 10% of the overtopping forces $N_{F,10\%}$ can be decided if the storm duration D and mean spectral wave period $T_{m-1,0}$ at the toe are known. P_{im} is empirically expressed as a function of incident wave conditions at the toe and the dike geometry parameters. In Fig. 4.8, P_{im} is plotted against a combination of relative dike width (B/L_t) and relative freeboard ($R_c/H_{m0,toe}$). L_t is calculated by $L_t = T_{m-1,0,t}\sqrt{gh_t}$ in shallow water condition. The open square markers illustrate the individual tests, whereas the filled circles denote the combined test. The same trend that is observed with both of the individual tests and combined tests indicates that the method of using combined tests from the repetitions is reliable. Eq. (4.3) shows the best fit between P_{im} and the combination of relative dike width and relative freeboard of the data from the 22 combined tests with $R^2 = 0.95$:

$$P_{im} = -0.06\ln\left(\frac{B}{L_t}\frac{R_c}{H_{m0,t}}\right) - 0.09, \tag{4.3}$$

4.3.2. DISTRIBUTION OF EXTREME OVERTOPPING FORCES

The objective of this study is to select a statistical distribution that provides the best goodness of fit to the maximum forces for a certain storm duration. In the previous section, the extreme data sample is defined by using the upper 10% the forces of each combined test. The next step is selecting a best-fit distribution, although Weibull is widely used for overtopping studies.

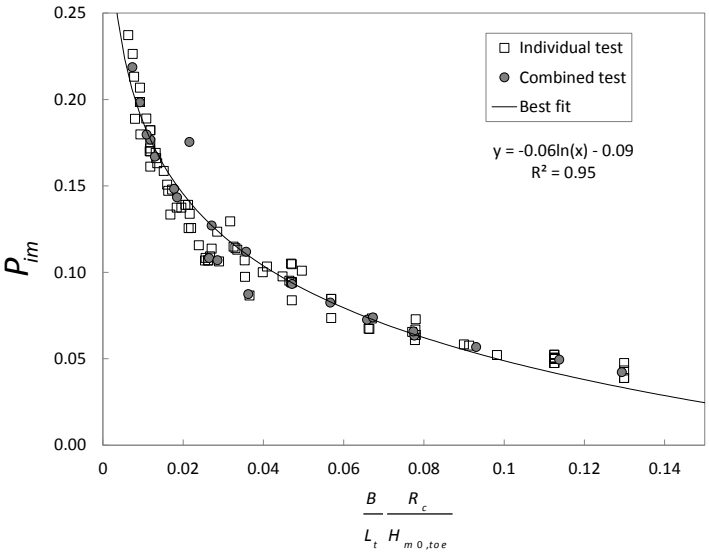

Figure 4.8: Overtopping force impact coefficient, which indicates the probability of the overtopping forces larger than $F_{10\%}$ during a storm.

In general, conventional methods of comparing and selecting an appropriate distribution is to compute RMSE (Root Mean Squared Error) and Bias (Hamdi et al., 2013). The RMSE is the square root of the variance of the residuals, indicating the differences between the values predicted and the values observed. Lower RMSE value gives a better fit. Whereas for the Bias, there are two selection criteria based on the likelihood function and involving the number of distribution parameters and the sample size (Méndez et al., 2006; Mazas and Hamm, 2011; Hamdi et al., 2013). One is Akaike Information Criteria (AIC) (Akaike, 1973) and the other one is Bayesian Information Criteria (BIC) (Schwarz, 1978). Since the data used in the present paper are from different test conditions with different sample sizes, the Bias method by using AIC and BIC is not suitable(Méndez et al., 2006).

The data sample is using the upper 10% tail of the distribution of the forces (e.g., $F_i > F_{10\%}$) of each test. Weibull, Generalized Pareto(GP), Gamma, Exponential (Exp.), Generalised Extreme Value (GEV), Lognormal (LogN.) and Rayleigh (Ray.) distributions are tested to fit to the extreme sample. The fitting was performed by using Maximum Likelihood (ML) method for the aforementioned distributions. Herein, the decision was made by comparing the mean of the RMSE of the total 22 test series for each distribution, see Table. 4.2. The results show that the GP behaves well for most of the test, although other distributions like Weibull, Gamma and Exponential also give good fits. The discussion of the behavior of the overtopping force extreme tail and the characteristics of the different distributions which can give good fit for some tests will be presented in Section 4.4.

In the end, GP (Pickands III, 1975; Coles, 2001) is selected as the best-fitting distribu-

Table 4.2: Summary of the results for different distribution models by using ML estimator

Test ID	$N_{F,10\%}$	GP	Weibull	Gamma	Exp.	GEV	LogN.	Ray.
Jon001	100	5.45	5.47	5.63	5.66	13.01	30.09	19.89
Jon002	95	5.35	4.17	5.18	6.75	5.82	68.97	18.08
Jon003	89	4.76	7.21	9.13	11.75	15.31	64.02	19.85
Jon004	106	5.91	7.14	8.08	9.85	24.92	29.24	21.21
Jon005	101	4.18	3.58	3.32	2.77	12.55	35.11	18.29
Jon006	97	3.25	3.35	4.40	8.33	8.84	32.07	13.03
Jon007	88	6.66	8.16	8.63	8.44	8.02	15.83	19.15
Jon008	121	6.81	9.85	10.83	11.33	14.26	6.66	20.94
Jon009	117	1.73	1.61	1.85	1.87	6.57	26.08	8.63
Jon010	44	5.01	5.06	5.81	8.25	26.74	43.83	18.56
Jon011	82	4.41	4.46	4.56	4.66	18.19	33.84	13.95
Jon012	55	10.11	10.47	11.17	12.71	10.02	52.44	25.66
Jon013	104	1.05	1.75	1.98	2.21	5.95	11.03	4.00
Jon014	86	11.54	13.62	14.82	16.63	15.69	13.78	27.26
Jon015	67	7.09	9.22	10.13	11.02	4.75	8.83	20.10
Jon016	78	1.87	1.90	1.98	1.79	8.07	4.66	5.02
Jon017	83	1.20	1.92	2.26	2.53	4.75	18.50	3.44
Jon018	149	1.48	1.41	1.34	1.50	4.57	10.77	5.85
Jon038	18	10.00	10.23	10.58	11.22	6.12	5.63	16.67
Jon039	20	10.66	11.09	11.39	9.58	7.22	6.57	20.20
Jon053	15	4.19	4.49	4.44	3.57	4.52	3.01	6.24
Jon054	15	3.19	3.04	2.96	2.06	3.51	5.52	6.43
Mean of RMSE		5.27	5.87	6.39	7.02	10.43	23.93	15.11

tion for the top-10% of overtopping wave forces, leading to the following expression for the probability density distribution of F_i:

$$G(F_i) = \begin{cases} 1 - \frac{N}{n+1}\left[1 + \frac{k}{\sigma}(F_i - F_u)\right]^{-\frac{1}{k}} & if \quad k \neq 0 \\ 1 - \frac{N}{n+1}\exp\left(-\frac{F_i - F_u}{\sigma}\right) & if \quad k = 0. \end{cases} \tag{4.4}$$

where F_u is the threshold, k is the shape parameter, and σ is the scale parameter. The shape parameter k determines the qualitative behavior of GP. If $k > 0$, the distribution has an unbounded tail; if $k = 0$, the GP is an exponential distribution with the scale parameter σ; and if $k < 0$, the GP is bounded by $F_{i,max} = F_u - \sigma/k$ (Coles, 2001). In this study, the threshold F_u is defined as the top 10% quantile of the impact force $F_{10\%}$, N is the number of forces larger than $F_{10\%}$, and n is the representative wave number at the toe N_{toe}. So the term $N/(n+1)$ in Eq. (4.4) is the overtopping force impact coefficient as defined in Eq. (4.2).

Then the exceedance probability of F_i ($F_i > F_{10\%}$) can be written as Eq. (4.5):

$$P(F_i > F_u) = 1 - G(F_i) = \begin{cases} P_{im}\left[1 + \frac{k}{\sigma}(F_i - F_u)\right]^{-\frac{1}{k}} & if \quad k \neq 0 \\ P_{im}\exp\left(-\frac{F_i - F_u}{\sigma}\right) & if \quad k = 0. \end{cases} \tag{4.5}$$

Rearranging Eq. (4.5), the m_{th} largest impact force peak of the incoming N_{toe} waves in a storm peak with a duration D is expressed as:

$$F_m = F_u + \frac{\sigma}{k}\left[\left(\frac{P_{im}}{P_m}\right)^k - 1\right], \tag{4.6}$$

with P_m the exceedance probability of the m_{th} largest impact force peak of the incoming N_{toe} waves with expressing as $m/(N_{toe}+1)$. For the largest force peak, $m = 1$. This all assumes that $k \neq 0$. If $k = 0$, working in the same way with Eq. (4.5) leads to

$$F_m = F_u + \sigma \ln\left(\frac{P_{im}}{P_m}\right). \tag{4.7}$$

4.3.3. PARAMETER DETERMINATION

A GP distribution has three parameters (threshold, shape parameter k and scale parameter σ). In this study, k and σ need to be determined. There are several fitting methods for estimating the best values of each parameter: Least Squares (LS), Maximum Likelihood (ML), Moment method (MOM), Maximum Product of Spacings method (MPS), Pickands' estimator (PKD) and Probability Weighted Moments (PWM). The performance and limitation of each method for the shape parameter of GP is summarized by Brodtkorb et al. (2000). Like the distribution selection procedure in the previous Section 4.3.2, the fitting method for the GP distribution is also compared, see Table 4.3. The result shows that MPS performs quite well for most of the tests. Therefore, the method of MPS is employed to estimate k and σ of GP and their confidence interval. Fig. 4.9 shows an example of the GP fit for test Jon002, in which the x axis indicates the exceedance probability of forces above the threshold, and the y axis indicates the relative value of the impact force above

Table 4.3: Summary of the results for different estimator of GP fitting

Test ID	$N_{F,10\%}$	MPS	ML	MOM	LS	PWM	PKD
Jon001	100	4.21	5.45	5.44	4.93	5.20	14.70
Jon002	95	4.65	5.35	5.51	5.34	5.93	11.13
Jon003	89	3.38	4.76	3.74	4.61	3.99	16.39
Jon004	106	4.04	5.91	6.72	7.16	5.62	12.25
Jon005	101	2.77	4.18	3.85	4.85	3.70	10.74
Jon006	97	2.89	3.25	3.16	3.31	3.15	9.99
Jon007	88	4.73	6.66	6.57	7.66	7.02	10.09
Jon008	121	4.69	6.81	7.18	6.53	6.91	6.92
Jon009	117	1.22	1.73	1.48	1.37	1.34	2.35
Jon010	44	6.97	5.01	7.11	5.01	5.95	55.20
Jon011	82	3.87	4.41	4.07	3.83	4.18	17.93
Jon012	55	7.31	10.11	10.60	8.75	10.17	23.17
Jon013	104	0.92	1.05	1.02	0.89	1.32	1.12
Jon014	86	10.94	11.54	12.76	11.66	12.00	18.64
Jon015	67	3.86	7.09	7.87	7.39	7.21	13.49
Jon016	78	1.99	1.87	1.88	3.76	1.94	2.41
Jon017	83	1.08	1.20	1.17	1.20	1.31	3.59
Jon018	149	1.26	1.48	1.42	1.33	1.56	3.55
Jon038	18	4.00	10.00	10.84	10.27	10.57	5.42
Jon039	20	6.07	10.66	10.57	11.21	10.31	10.32
Jon053	15	3.37	4.19	4.16	3.95	4.65	52.03
Jon054	15	1.94	3.19	2.72	3.77	2.66	11.18
Mean of RMSE		3.92	5.27	5.45	5.40	5.30	14.21

the threshold.

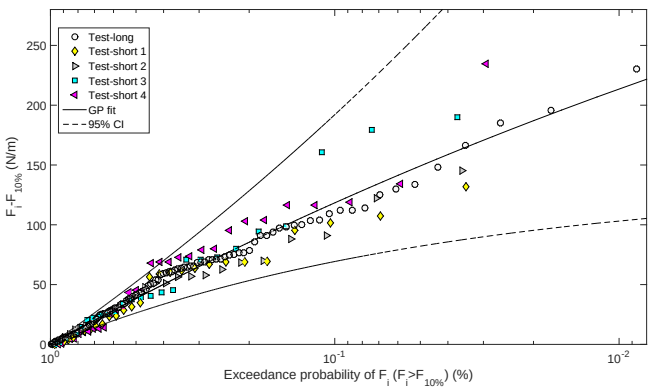

Figure 4.9: An example of the GP fit for test Jon002. Diamond, right-triangle, square and left-triangle markers indicate the data from repetitions 1 to 4 of test Jon002. Circles are the full data set created by adding the four repetitions. The solid line indicates the GP distribution, with 95% confidence interval (dashed line).

4.3.4. EMPIRICAL GP DISTRIBUTION

After the fitting procedure, a specific GP distribution has been determined for each test series, which can be used to estimate F_i at a certain exceedance probability P_m, e.g., the expected value of the maximum force peak, $F_{i,max}$. In this section, a series of empirical formulas for the GP parameters (threshold, scale and shape) is proposed by using incident wave characteristics and dike geometry parameters.

EMPIRICAL THRESHOLD

In the previous analysis, we used the upper 10% quantile force peak $F_{10\%}$ as the threshold, F_u, to fit the upper 10% tail of the force peak distribution to GP distribution. For different test conditions, the tails of the real force distributions are different. Therefore, a characteristic force, which can represent the features of the overtopping wave impact event, is needed for determining an empirical threshold value.

Chen et al. (2015) introduced an empirical formula to predict the force peak for individual overtopping events by using regular waves, which is proportional to the square of overtopping flow layer thickness at the beginning of the crest. In this study, most of the primary incoming waves break at the foreshore or on the dike. The resulting individual bore-like impacts on the wall are similar to those in regular wave tests (Chen et al., 2015), because the high pressures of the short duration impulsive impact peaks described in Section 4.2.2 are not take into account due to the low-pass filtering of the forces. Therefore, based on the similar physical relevance of both regular wave and irregular wave tests, we use Eq. (4.8) to express the characteristic force since the term within the square brackets in Eq. (4.8) is proportional to overtopping flow layer thickness:

$$F_c = \rho g \left[H_{m0,t} \left(1 - \frac{R_c}{R_u} \right) \right]^2, \tag{4.8}$$

where R_c is the freeboard, R_u is the wave run-up height. The meaning of each parameter can be found in Fig. 3.4. The run-up height Ru is applying the formula Eq.4b for $R_{u2\%}$ in Van Gent (2001). The wave parameters in Eq.4b are using $H_{m0,t}$ and $T_{m-1,0,t}$ of the total wave energy spectra, and the coefficients are taken from Table 5 of Van Gent (2001).

Fig. 4.10 shows the relationship between dimensionless $F_{10\%}$ and dimensionless calculated characteristic force F_c by using Eq. (4.8). The best curve-fitting result with R-squared of 0.96 provides a reasonable estimate of the threshold value of GP distribution in this study, see Eq. (4.9):

$$\frac{F_u}{\rho g H_{m0,t} R_c} = 0.84 \exp\left(0.36 \frac{F_c}{\rho g H_{m0,t} R_c} \right) \tag{4.9}$$

SCALE PARAMETER

The scale parameter σ, that was determined for all tests, is exponentially increasing with F_c as shown in Fig. 4.11. The circles indicate the combined test, and solid line represents the best fit, see Eq. (4.10):

$$\frac{\sigma}{\rho g H_{m0,t} R_c} = 0.37 \exp\left(0.37 \frac{F_c}{\rho g H_{m0,t} R_c} \right) \tag{4.10}$$

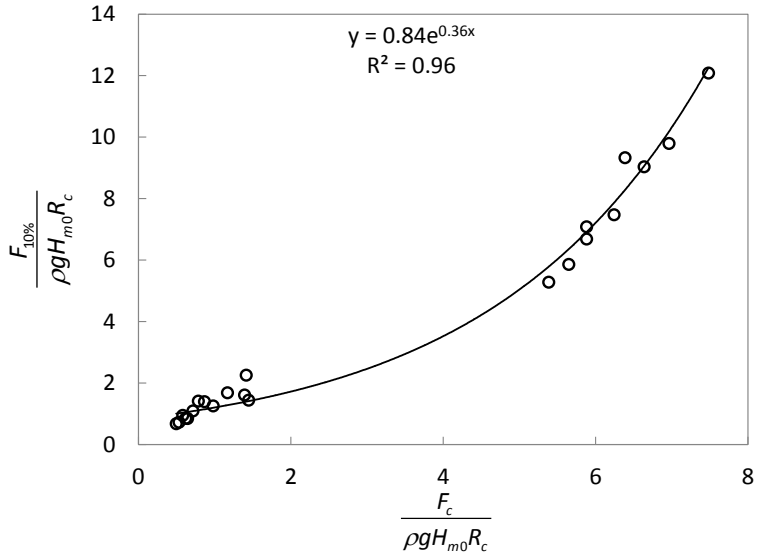

Figure 4.10: Empirically estimated threshold of GP distribution.

The standard error of σ obtained from GP fitting is expressed in the same manner as Eq. (4.10):

$$\frac{\sigma_{StErr}}{\rho g H_{m0,t} R_c} = 0.07 \exp\left(0.33 \frac{F_c}{\rho g H_{m0,t} R_c}\right) \tag{4.11}$$

which is obtained from the best fit of standard error of σ from the tests with repetitions. Fig. 4.12 shows the non-dimensional standard error of σ against non-dimensional F_c. Circles indicate the tests with repetitions, whereas crosses indicate the four tests without repetitions. As the sample size of the non-repeated tests is small, the uncertainty of the GP fitting is large. Therefore, the crosses deviate from the main trend, as shown in Fig. 4.12, which is reasonable.

SHAPE PARAMETER

Through inspection, and after several attempts to use dimensionless combinations of the scale parameter and different wave parameters, the best empirical result for the shape parameter was the relationship:

$$k = -0.59 \ln\left(\frac{\sigma}{\rho g H_{m0,t}^2}\right) - 0.34. \tag{4.12}$$

Fig. 4.13 shows the best fit curve for the shape parameter k obtained from GP fitting, and the correlation coefficient for the best fit of Eq. (4.12) was 0.72. As can be seen, k varies within a wide range from -0.3 to 0.8 decreasing with increasing values of σ. Herein, the best fit curve is obtained by excluding two big outliers from the test Jon013 and Jon017.

Fig. 4.14 shows the standard error of k obtained from GP fitting. The empirical stan-

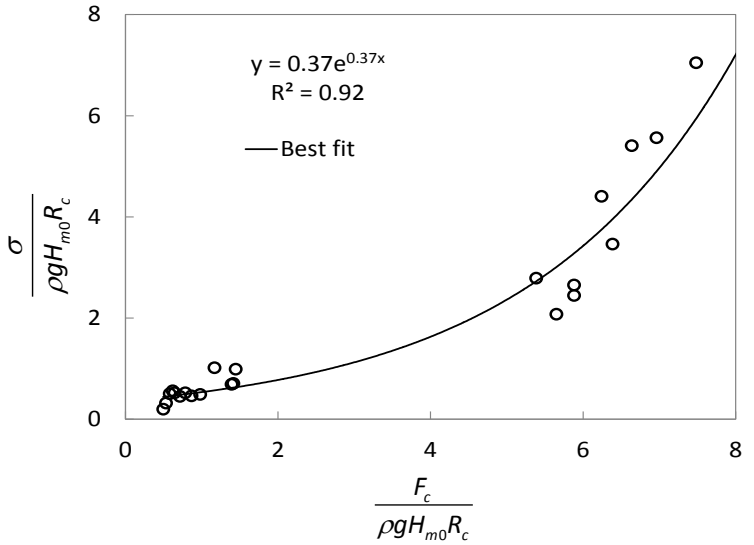

Figure 4.11: Empirically estimated scale parameter σ.

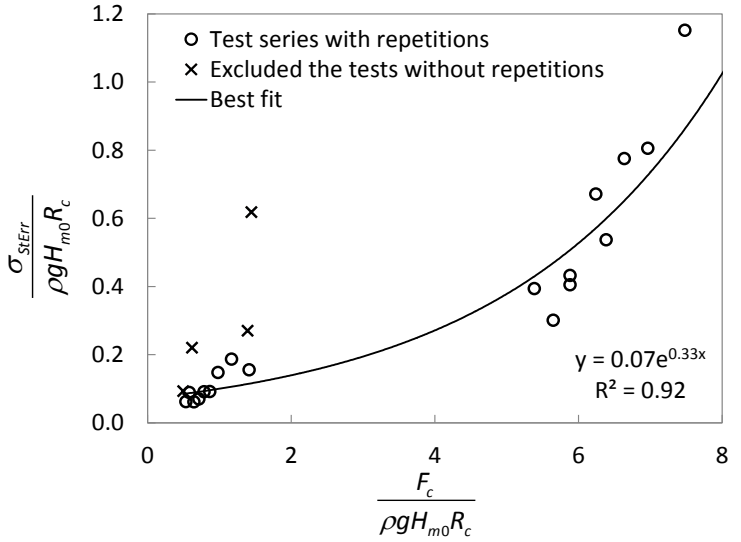

Figure 4.12: Empirically estimated the stranded error of scale parameter σ.

dard error of k was determined by using the mean value of the K_{StErr} from the tests with repetitions. The reason of excluding the tests without repetitions is same as that of σ_{StErr}.

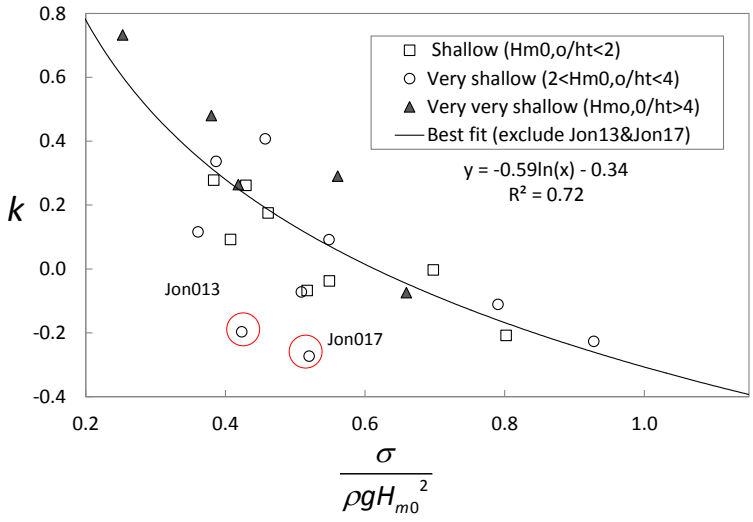

Figure 4.13: Empirically estimated shape parameter k.

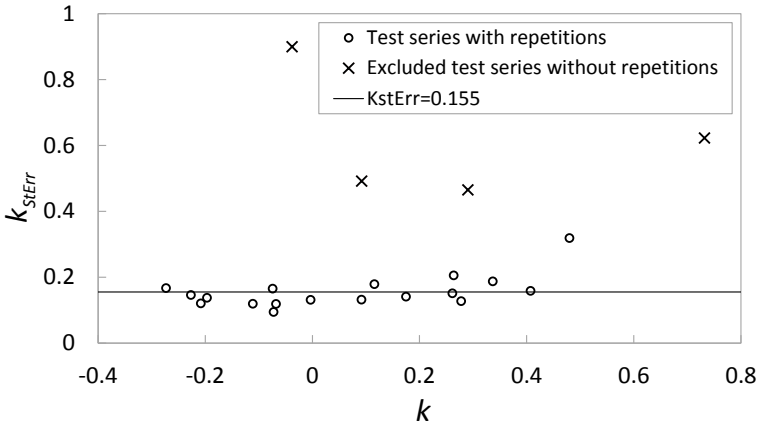

Figure 4.14: Empirically estimated the stranded error of shape parameter k. The best fit of K_{StErr} is determined as a constant value 0.155, which is the mean value of the test with repetitions, illustrated by the filled circles. The excluded test is illustrated as red cross.

PERFORMANCE OF THE PROPOSED EMPIRICAL GP MODEL

Based on the previous results, a seven-step procedure for predicting the maximum force which is expected to occur on the building ($F_{max,exp}$) for a certain storm peak duration is summarized:

- Calculate the overtopping impact probability P_{im}: using Eq. (4.3);
- Calculate the characteristic force F_c: using Eq. (4.8);

- Calculate the empirical threshold F_u: using Eq. (4.9);
- Calculate the empirical scale parameter σ: using Eq. (4.10), with a standard error using Eq. (4.11);
- Calculate the empirical shape parameter k: using Eq. (4.12), with a standard error 0.155;
- Calculate the expected maximum overtopping force exceedance probability $P_m = \approx T_{m-1,0,t}/D$;
- Calculate the expected maximum overtopping force $F_{max,exp}$ and its uncertainty range for a storm peak duration D: using Eq. (4.6) or Eq. (4.7) if $k = 0$.

The performance of the proposed GP distribution with the empirically determined GP parameters (threshold, scale parameter, and shape parameter) is evaluated by comparing the calculated maximum overtopping force $F_{max,exp}$ with the maximum overtopping force $F_{max,GPfit}$ estimated by fitting a GP distribution to each test. In Fig. 4.15, $F_{max,GPfit}$ is plotted against $F_{max,exp}$ with a correlation coefficient $R^2 = 0.96$, which indicates the proposed empirical GP distribution provides an acceptable performance on the prediction of maximum overtopping force.

4.4. DISCUSSION

In this study, GP is selected as the most suitable distribution for the extreme data sample of 22 test series. However, other distributions like Weibull, Gamma, Exponential distributions were also good for some tests. In statistics, large sample theory is a generic framework for assessment of statistical tests (Cam and Yang, 2000). Mazas and Hamm (2011) argued that the possibility of other distributions give better fits because sometimes we do not know whether the distribution we selected is within the large sample domain. We combined repetitions of each test series as new data samples, which can provide a relative larger sample than the individual tests. Fig. 4.13 gives the empirical estimation of k. The decreasing trend of k with increasing σ is still clear. When k drops from the positive domain to the negative, the tails of the force distribution intends to change from having an unbounded tail to a bounded tail. Even though the scatter is big resulting a poor fit, the result of comprising fitted $F_{max,GPfit}$ with empirically determined $F_{max,exp}$ is quite well (with $R^2 = 0.96$). The range of k values obtained from GP fitting is only -0.3 to 0.8, which demonstrates that it is not sensitive to the extreme values comparing the scale parameter σ. Based on practical experience, especially for coastal engineering applications, wave height at the toe of the structure is a key design parameter. Normally, wave heights are physically bounded (Mazas and Hamm, 2011), so the Weibull distribution always has a good performance in predicting wave height (e.g., Rayleigh distribution which is a special case of Weibull distribution) and wave overtopping (e.g., Victor et al., 2012; Zanuttigh et al., 2013; Nørgaard et al., 2014; Pan et al., 2015). In order to provide a better prediction for k and investigate more insight with physics, more test with enough data sample and a wide range of test parameters are needed.

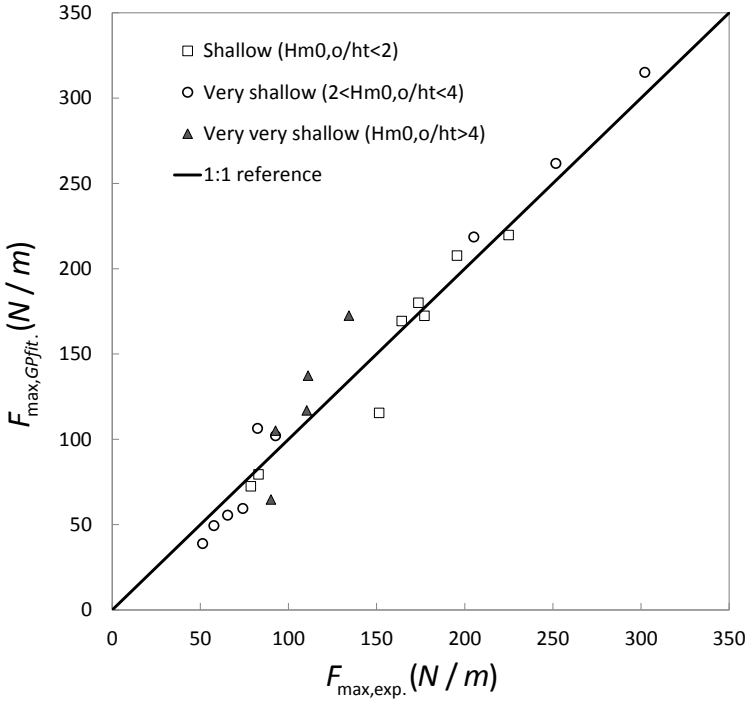

Figure 4.15: Comparison of $F_{max,exp}$ and $F_{max,GPfit}$ of the test series with duration of 900 s. Hollow squares indicate the tests of shallow water conditions, hollow circles indicate the tests of very shallow water conditions, and the filled triangles indicate the tests of very very shallow water conditions.

The threshold of GP fit is selected as the upper 10% quantile of the overtopping force. Even though the final results are good, the uncertainty caused by the threshold is excluded. In the future study, more effort is needed to arrive at a more precise threshold for different overtopping wave conditions. Martin et al. (1999) promoted a method of using broken wave impact force formula obtained from regular wave tests to irregular waves via the hypothesis of equivalence introduced by Saville (1962). Therefore, based on the similarity of large wave impact from the observations of regular wave tests (Chen et al., 2015), the characteristic force is used for the estimation of the threshold F_u, Eq. (4.9), and the scale parameter σ, Eq. (4.10).

In this study, the measured force can be influenced by scale effects. This typically results in a measured force that is larger than that in reality, since the "wall" used in the laboratory is much more rigid, and has a higher natural frequency than at full scale (Oumeraci et al., 2001). In order to reduce this effect, a low-pass filter at 50 Hz in model scale was deployed for force data processing, which indeed reduced the measured extreme force peaks if the first dynamic peak was much larger than the quasi-static peak. The order of the reduction of the dynamic peak force is about 10% to 20% of the unfiltered data from the load cells. Applying a low-pass filter is quite reasonable for the current study as the impacted object on the dike is a vertical wall with large inertia, which

Table 4.4: Parameter range for the curent study

Parameter	Range
$\xi_{m-1,0}$	5−19
$R_c/H_{m0,t}$	0.1−1
$H_{m0,o}/h_t$	1−6
B/L_t	0.03−1.5
$\cot\beta$	3

can represent buildings or other types of large structures. However, more methods of transforming the measured force to the force in real situations need to be developed in a future study. For now, if natural frequency of the object is higher than 10 Hz (in prototype), an up to 20% higher force would be advised to be used. A second source of scale effect is the influence of surface tension and related large air bubbles in the model. Using fresh water and a small scale overestimates the impact pressure because less entrained air is present (Bullock et al., 2001). In this study, this effect was not taken into account, so a somewhat conservative force might be obtained.

The current physical model tests were conducted with one dike slope (1:3), one foreshore slope (1:35), and two dike crest widths $B = 0.5$ m for most of the tests, and $B = 0.25$ m for only two tests. The wave height and wave periods used to develop the empirical formulas for GP distribution in this paper are the measured at the position of the toe without the dike structure as recommended by Van Gent (2001) especially for the shallow water condition. The influence of foreshore slope and dike slope are not considered in this study, but will be investigated in the future. The applicability of the proposed empirical formula is limited to the range of the parameters, which are listed in Table 4.4.

4.5. CONCLUSION

Prior work has documented the statistical characteristics of the overtopping volumes and discharge over a dike. However, the study of the overtopping forces has not well-developed yet. This paper addresses the statistical analysis of the overtopping forces on a vertical wall on a horizontal dike crest with a shallow foreshore in front of the dike via a series of physical model tests. GP distribution gives a suitable fit among commonly used distributions for the extreme overtopping forces (the upper 10% of the force distribution). The three parameters includes a threshold (F_u), scale parameter (σ) and shape parameter (k). The threshold is fixed as 10% exceedance overtopping force, $F_{10\%}$, which gives the good performance on the extreme force sample size in this study. The threshold (F_u) and scale parameter (σ) are empirically described by the incident wave conditions at the toe and dike freeboard and dike crest width, whereas the shape parameter (k) is correlated to the scale parameter. A new 7-step procedure is a simple tool for assessing the maximum force occurred during a certain storm peak duration, which shows an overall satisfactory performance.

In the future, more work should be carried out to investigate the influence of the foreshore slope and dike slope. By using wider range of the wave condition, and the dike

crest width, the shape parameter k need to be better estimated.

APPENDIX

The GP fitting results are presented in Table 4.1.

Table 4.1: GP fitting results

Test series	$N_{F,10\%}$	$F_{10\%}$	k	k_{StEr}	σ	σ_{StErr}
Jon001	100	91.412	0.092	0.132	33.895	5.264
Jon002	95	103.879	-0.111	0.119	59.007	8.543
Jon003	89	136.900	-0.227	0.146	79.840	13.054
Jon004	106	64.425	0.261	0.151	22.243	3.683
Jon005	101	71.720	-0.003	0.131	42.264	6.443
Jon006	97	91.666	-0.208	0.120	54.894	7.870
Jon007	88	60.869	0.175	0.141	24.166	3.942
Jon008	121	51.471	0.278	0.127	18.241	2.647
Jon009	117	44.513	-0.068	0.118	23.508	3.319
Jon010	44	41.967	0.480	0.319	16.352	4.952
Jon011	82	61.344	-0.074	0.165	37.106	6.827
Jon012	55	88.397	0.264	0.205	27.730	6.093
Jon013	104	34.972	-0.197	0.137	14.424	2.242
Jon014	86	47.982	0.407	0.158	17.656	3.100
Jon015	67	50.299	0.337	0.187	16.589	3.317
Jon016	78	19.683	0.116	0.178	8.556	1.686
Jon017	83	26.929	-0.273	0.167	14.244	2.528
Jon018	149	25.458	-0.072	0.094	15.637	1.861
Jon038	18	29.241	0.732	0.622	8.442	4.022
Jon039	20	41.636	0.290	0.464	27.335	10.776
Jon053	15	31.275	0.092	0.491	13.380	5.241
Jon054	15	28.719	-0.038	0.899	19.686	12.307

5

VULNERABILITY OF BUILDINGS ON COASTAL DIKES DUE TO WAVE OVERTOPPING

The vulnerability of buildings on coastal dikes due to overtopping wave impacts is difficult to assess. A method is developed in this chapter to quantify the vulnerability of masonry buildings on a coastal dike exposed to wave overtopping. Using the formulas from the previous chapter the accidental loads due to the extreme wave impacts are characterized. Using the approach from Eurocode 6, the strength of masonry buildings under these loads is assessed. Results from a case study in Belgium show that masonry buildings located at 10-15 meters away from the seafront would suffer from localized damage under a 1000 year storm due to breaking windows, and would collapse under a 10,000 year storm. The method can be used to assess the safety of existing buildings on coastal dikes, and to design new buildings.

This chapter is based on: Chen, X., Jonkman, S.N., Pasterkamp, S., Suzuki, T., Altomare, C. (2016). Vulnerability of coastal buildings due to wave overtopping. Journal of Waterway, Port, Coastal, and Ocean Engineering (submitted).

5.1. INTRODUCTION

Low-lying and densely populated coastal regions in the Netherlands and Belgium are becoming more attractive areas for economic, environmental, and social development (Aerts and Botzen, 2011). In these regions, buildings and infrastructures are present quite close to the sea defence line. There is a relatively high risk of damage and loss of life caused by coastal flooding, and the risks could increase with climate change and sea level rise.

Coastal flooding can be caused by high sea level, breaching of the sea defence, as well as wave overtopping. Even though the first two causes are the main concerns when assessing flood risk for the highly developed coastal sites, overtopping effects will be important for buildings on the coast. Allsop et al. (2008) pointed out that the direct hazard from overtopping for the coastal buildings and human beings is being ignored, so more attention is needed.

In the Netherlands and Belgium, wide crested dikes are used as flood defence structures for the densely populated coastal front sites (Verwaest et al., 2010). Overtopping for coastal dikes with slopes occurs when the incident wave runs up along the seaward slope of the dike and over its crest. The buildings on the top of the dikes are threatened from overtopping effects associated with wave run-up. Fig. 5.1 shows a typical configuration for a Belgian coastal site and the most relevant overtopping processes. In winter, storms often lead to a significant increase in surge combining with high waves that may induce serious overtopping by runup waves. This shoreward overtopping wave on the dike can exert a strong hydrodynamic force on the buildings. There are no relevant records of the direct damage from wave run-up overtopping on waterfront buildings either in reality or site model tests. Even though relevant research has been done for wave impacts of tsunamis (e.g., Nistor et al., 2009) and surges (e.g., Ramsden, 1996; Hatzikyriakou et al., 2015) on coastal buildings, a method to assess the damage due to the runup of overtopping waves on structures on a coastal dike is not yet available as far as the authors are concerned. The objective of this paper is to develop a practical method to evaluate the vulnerability of buildings on coastal dikes caused by the impact load of overtopping waves. This method can also be used to provide guidance for designing new buildings on the dike. The study focused on the collapse and localized damage of masonry buildings as this is a common building type on the Dutch and Belgian coast. The approach is also applicable to other building types.

The structure of this paper is as follows. Section 5.2 describes the impact mechanism of overtopping waves, and introduces the empirical method to calculate the maximum overtopping wave load during a certain storm peak. In Section 5.3, we analyze the failure mechanisms of masonry buildings on coastal dikes. We assess the masonry properties including material strength and support conditions. We calculate the capacity of lateral moment, and define the limit state function of the masonry structural and non-structural elements. In Section 5.4, a case study is presented. Using realistic data for the Belgian situation, the comparison of the calculated maximum overtopping wave load and the lateral capacity of building elements for collapse of a masonry building is considered. Discussion and conclusions are drawn in Section 5.5.

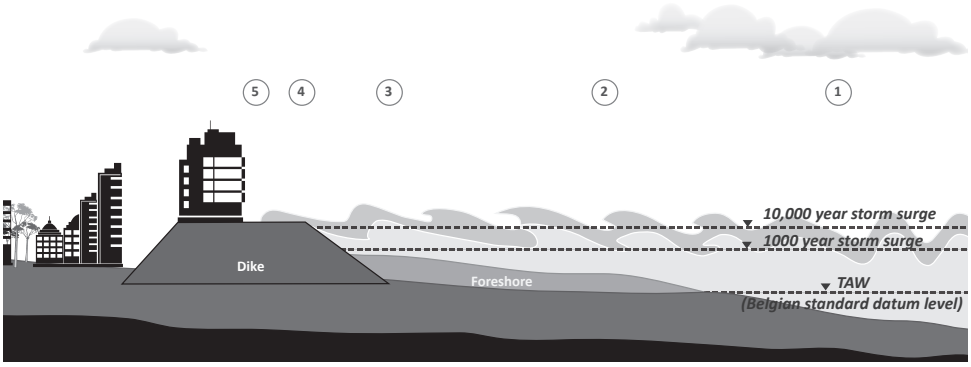

Figure 5.1: An example of a typical coastal dike with buildings on top in Belgium. The whole process of overtopping wave impacting on the building: ① Wind generates waves far away from shoreline; ② Offshore waves coming into the shallow foreshore area, increasing wave height. Finally, most waves are broken and wave energy is dissipated in the form of turbulent bore. ③ Turbulent bore (broken wave) running up on the seaward slope of a dike and overtopping the crest of the dike; ④ Part of the overtopping flow continue propagating along the dike crest and the other part flowing back seaward; ⑤ Overtopping wave impacting on the building eventually (Chen et al., 2015).

5.2. OVERTOPPING WAVE LOADS

Overtopping waves are specifically defined as the waves that are generated after the incident run-up waves flow over the dike crest. An estimation of the maximum load of overtopping waves is necessary in order to evaluate the vulnerability of buildings during a certain storm peak. In this section, first we provide an overview of general flood load on buildings. Then overtopping wave impacts are specified. Afterwards, an empirical estimation of the maximum overtopping wave load during a storm peak is given, which is based on previous study such as Chen et al. (2016).

5.2.1. GENERAL FLOOD LOADS

The coastal construction manual FEMA P-55 (2011) classifies the general flood loads that coastal residential buildings can be exposed to. The most common flood load is the hydro-static load from flood water in both lateral and vertical direction. The hydro-static load in lateral direction is mainly caused by standing water or slowly moving water, whereas the hydro-static load in vertical direction is normally due to the buoyancy, as shown in Fig. 5.2(a). Another common flood load is hydrodynamic load (or drag force), which is induced by fast moving flow, surge and tsunami around the structure, as shown in Fig. 5.2(b). For the coastal buildings, especially those buildings located in the wave breaking zone, the wave impact load is important: the horizontal breaking wave impact load is depicted in Fig. 5.2(c). Besides the direct hydro-static and hydrodynamic load from water, there are two other types of indirect load that need to be considered. One is the impact load imposed on a building by floating objects in the flood water. The other one is the localized scour around the foundation of buildings by waves and currents during the flood.

A dynamic overtopping wave load on a building consists of an impact force and a

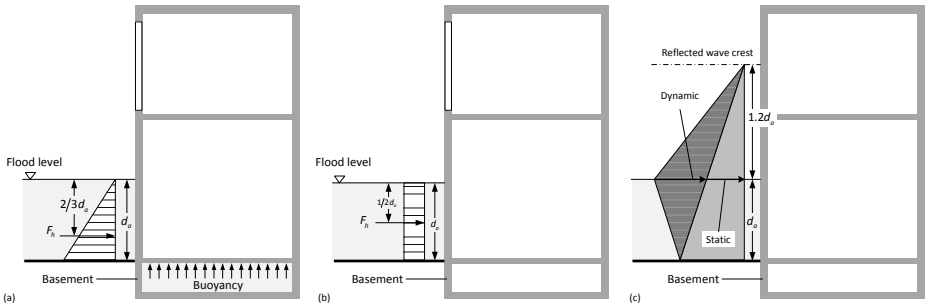

Figure 5.2: (a) Horizontal hydro-static load and vertical buoyancy on building; (b) hydrodynamic load on buildings; (c) horizontal breaking wave impact load on the external wall (adapted from (FEMA P-55, 2011))

.

hydrodynamic drag force. Since the building is located in the path of the incident overtopping waves on the dike crest, part of the incident overtopping waves will strike on the facade of the building resulting in an impact load, and be reflected back seawards. The impact load is the dominant dynamic load on the building during this impact process. The other part of the incident waves would flow over the dike crest through the gaps between two buildings. During this process, the building is subjected to hydrodynamic drag force. In this study, the hydrodynamic load induced by the impact of an overtopping wave on the external wall is considered as the primary flood load. We only concern the impact load due to wave overtopping since it is the most relevant load to the vulnerability of the buildings under the additional assumptions that the impact load is larger than hydro-static load and incident waves already break on coastal dikes. Details of the failure mechanisms of the building are given in Section 5.3.

5.2.2. OVERTOPPING WAVE IMPACT MECHANISM

IMPACT PROCESS AND CHARACTERISTICS

An overtopping event consists of the process of wave generation (see the processes ① to ③ in Fig. 5.1), overtopping wave formation (see the processes ③ to ④ in Fig. 5.1), and the resulting impact (see the processes ④ to ⑤ in Fig. 5.1). An individual overtopping wave generated on the dike crest is similar to a tsunami wave. Thus an impact load of the individual overtopping wave may be seen as the impact of tsunami wave. The study of this impact dates back to Cumberbatch (1960)'s analytical solution for the impact of a uniform steady flow on a wall. Afterwards, Cross (1967) improved Cumberbatch (1960)'s model to calculate the total tsunami force. Ramsden (1996) expanded the study of tsunami impact to include more formats of waves to represent tsunami waves, e.g., long waves, solitary waves, bores and surges. Several authors also studied tsunami forces on various types and shapes of structures (e.g., Arnason, 2005; Arnason et al., 2009; Nistor et al., 2009; Nouri et al., 2010). Therefore, the current knowledge of tsunami can be applied to study the impact process of an overtopping wave on a vertical wall (e.g., the processes ④ to ⑤ in Fig. 5.1). However, overtopping waves are generated by storm waves which are stochastic. Thus it is necessary to provide an estimation of the maximum or

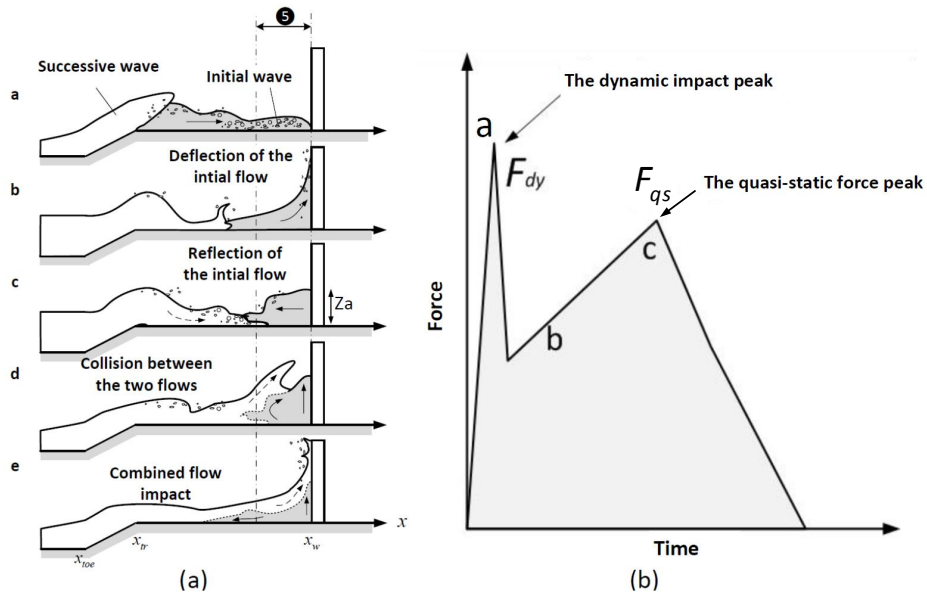

Figure 5.3: (a) Sketch of overtopping wave impact process; (b) Sketch of the time series of overtopping wave impact load.

representative overtopping impact load including the incident wave characteristics and dike geometry parameters.

Fig. 5.3 shows a schematic sketch of two overtopping wave impact events and a ketch of overtopping wave impact time series. In Fig. 5.3(a), the impact processes of two overtopping waves are shown. Stages (a) to (c) indicate the impact process of the individual overtopping wave (in gray color). Stages (c) to (e) show the interaction between the initial reflected overtopping wave (in grey color) and the following incident overtopping wave (in white color). In stage (d), the piling-up of the following incident wave on the top of the reflected wave can result in a violent impact on a high vertical position on the external of the wall. In Fig. 5.3(b), the schematic sketch of the time series signal of an overtopping wave impact including stages (a) to (c) is illustrated with marked dynamic impact peak in the stage (a) and the maximum quasi-static force peak in the stage (b) or (c). During the initial impact stage (a), the overtopping wave front changes its direction suddenly and results in a sharp dynamic impact peak with a large magnitude and short duration. During the stages of deflection (b) or reflection (c), the maximum quasi-static force peak is formed with a relative lower magnitude and longer duration, which is governed by gravity. At the moment the maximum quasi-static peak occurred, the instant pressures along the wall are almost linearly distributed (Chen et al., 2014).

Chen et al. (2015) stated that the magnitudes of the dynamic force peak and the quasi-static force peak of a single overtopping wave impact are no obvious difference. The authors also pointed out the significance of the quasi-static force peak on the stabil-

ity of building on the dike. Thus the maximum quasi-static force peak (F_{qs}) is selected as the overtopping impact load on the building. However, violent impact can be expected if the interaction of multiple overtopping waves occurs in front of the wall Chen et al. (2016). The dynamic peak of the violent impact with a short duration (0.01-0.1 seconds) could influence the local structural elements with a high natural frequency Chen et al. (2015, 2016). Thus, when considering the local structural element with a high natural frequency such as windows, the dynamic force (F_{dy}) can be considered as the overtopping impact load determined by using F_{qs} amplified by a factor α_{im},

$$F_{dy} = \alpha_{im} F_{qs}. \tag{5.1}$$

It is suggested that the minimum value of α_{im} is 2.5 (Oumeraci et al., 2001), which depends on the structure properties.

EXPECTED MAXIMUM OVERTOPPING WAVE LOAD

Due to a lack of relevant records for overtopping wave load on real buildings and systematic knowledge (Allsop et al., 2008), a model to predict the extreme overtopping wave load during a single storm is required. Chen et al. (2016) conducted a series of experimental model tests by using random waves. The impact loads of overtopping waves were measured by load cells with the inclusion of the violent impact influenced by the interaction of overtopping waves. The maximum value of F_{dy} and F_{qs} of each overtopping event was used for determining the maximum impact load F_m during a storm peak. Based on the results, the authors proposed an empirical Generalized Pareto (GP) distribution to estimate the maximum impact load of overtopping waves (F_m) during a storm peak, shown as:

$$\begin{cases} F_m = F_u + \frac{\sigma}{k}\left[\left(\frac{P_{im}}{P_{max}}\right)^k - 1\right], \ k \neq 0 \\ F_m = F_u + \sigma \ln\left(\frac{P_{im}}{P_{max}}\right), \ k = 0 \end{cases} \tag{5.2}$$

where F_u is the threshold of GP distribution [N/m]; σ is the scale parameter of GP distribution [N/m]; k is the dimensionless shape parameter of GP distribution [-]. P_{im} is the overtopping wave impact probability [-], and P_{max} is the probability of the maximum overtopping wave impact load [-]. Details of the definition and determination of each parameter in Eq. 5.2 are shown in Appendix 5.C.

Based on the quasi-static nature of the maximum overtopping wave load F_m, we define an equivalent overtopping run-up height (Z_a, see Fig. 5.3(a)) along the wall of the building as:

$$Z_a = \sqrt{\frac{2F_m}{\rho g}}. \tag{5.3}$$

where ρ is the density of the water [kg/m^3]. When considering the real dynamic force executing on a local structural or non-structural element with high natural frequency, we multiply F_m by the factor $\alpha_{im} = 2.5$ as the dynamic load on local structural elements and 1.58 for Z_a in this study. In the future, a model for α_{im}, concerning different type of structural materials is needed. The empirical formula is obtained from the scaled experimental model tests. The scale effect of the model tests can be neglected since F_m

is quasi-static, following the Froude scaling law.

5.3. VULNERABILITY OF BUILDINGS CAUSED BY OVERTOPPING WAVES

In this section, the relevant failure mechanisms of buildings on a coastal dike and the corresponding limit states are defined for a masonry building and its components. An approach for assessing the vulnerability of buildings caused by overtopping waves is developed. The partial factor method, as described in the Eurocode 6 is used to derive design values of load and strength, and comparison with the ultimate limit state.

5.3.1. FAILURE MECHANISMS OF BUILDINGS

For the buildings on the coastal dikes, the most relevant failures due to the overtopping load are structural collapse and localized damage of elements of the building. Fig. 5.4 shows a fault tree for the collapse failure mode. The collapse can be caused by either loss of the support of the foundation of the building (losing stability) or the failure of a key structural element (low strength). Failure of the foundation can be caused by the loss of the bearing capacity of the subsoil. This undermining of the subsoil can be induced by scour around the foundation due to fast overtopping flow or the failure of the dike itself. Other sources may cause the foundation to lose its stability. For example, the incident overtopping wave may infiltrate in the dike. This phenomenon may increase the uplift pressure and eventually undermine the stability of the foundation. Considering the short duration of the impact of overtopping wave on the dike comparing to the infiltration process, this undermining process can be neglected. The failure of a key structural element is directly related to the lateral action from overtopping waves. Key structural elements of a building are load bearing walls, columns and stability walls. The failure of these elements will lead to the collapse of the whole building. These structural elements are normally designed to be strong enough to withstand external load, such as the wind load.

When considering a large overtopping wave, it is expected to destroy the bearing wall or column when its impact load is beyond the strength of the structure. The collapse of the building is likely to cause loss of life if people are present. In this study, we only take into account the failure caused by the direct impact action of overtopping waves on the building (i.e. the solid lines of Fig. 5.4).

The local damage of the building is identified as a kind of failure which does not lead to collapse. It may include the failure of windows, doors and the facade walls (non-load bearing wall). The failure of windows and doors is due to the lower strength of the elements and their connections compared to the subjected load, whereas the failure of the non-structural wall is similar to that of the key structural walls by either shear failure or bending failure. The local damage of the building will create openings in the facade and the inside content of the building will be exposed to the overtopping water.

5.3.2. FAILURE OF THE EXTERNAL WALL

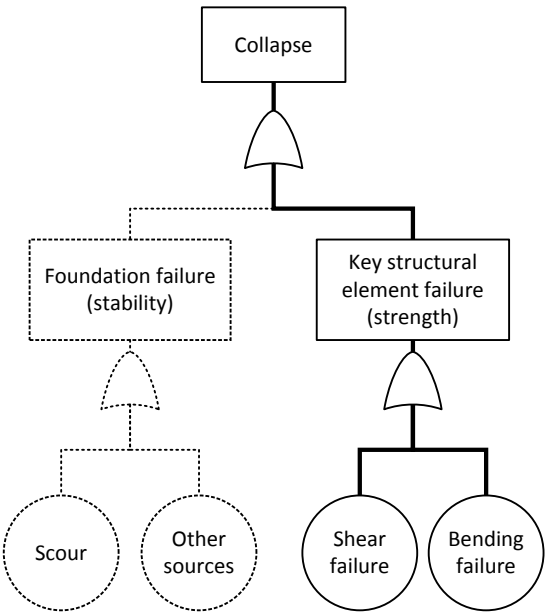

Figure 5.4: A simple fault tree of the collapse of buildings on a coastal dike.

EQUIVALENT STATIC LOAD

The impact load from overtopping waves is assumed to be an accidental load. It is for a design situation that is defined as having a low probability of occurring during the working life of the structure. An additional assumption is that the dike will not breach or become stable during the overtopping event. A rough estimation of the occurrence of wall failure under bending is made by assuming the averaged hydraulic pressure is approximately equal to the characteristic uniform distributed load q_k for the failure state Kelman (2002). Fig. 5.5 shows the illustrations of different loads subjected to a wall. Fig. 5.5(a) shows the characteristic uniform distributed load q_k subjected to the wall panels on the ground floor, which is typically designed for wind load. Fig. 5.5(b) shows hydro-static pressures subjected to the wall when $Z_a \geq h$. Z_a is the equivalent overtopping run-up height on the wall [m], as defined in Eq. 5.3, and h is the floor height [m]. The maximum hydro-static pressure $q_{w,max}$ [KN/m^2], minimum hydro-static pressure $q_{w,min}$ [KN/m^2] and the averaged pressure q_{avg} [KN/m^2] are shown in Eq. 5.4 to 5.6. When $Z_a < h$, $q_{w,min} = 0$, the equivalent average hydro-static pressure over the entire wall plate is expressed as shown in Eq. 5.6. Therefore, the averaged pressure of a wall plate $q_{avg,S}$ can be used to replace q_k as the characteristic lateral load of a wall when it withstands hydraulic load.

$$q_{w,\max} = \rho g Z_a \tag{5.4}$$

$$q_{w,\min} = \begin{cases} \rho g (Z_a - h) & \text{for} \quad Z_a \geq h \\ 0 & \text{for} \quad Z_a < h \end{cases} \tag{5.5}$$

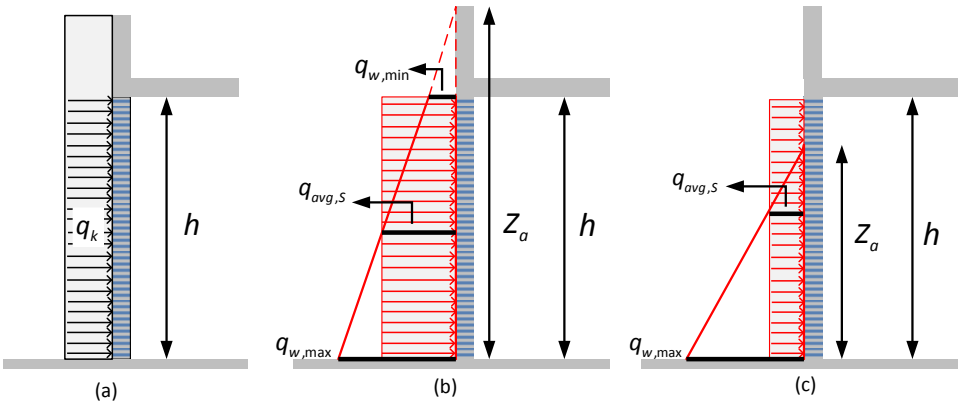

Figure 5.5: (a) Uniform distributed characteristic lateral load; (b) linearly distributed hydrostatic load over the wall when $Z_a \geq h$; (c) linearly distributed hydrostatic load when $Z_a < h$.

$$q_{avg,S} = \begin{cases} \rho g\,(Z_a - 0.5h) & \text{for} \quad Z_a \geq h \\ \frac{\rho g {Z_a}^2}{2h} & \text{for} \quad Z_a < h \end{cases} \tag{5.6}$$

LIMIT STATE FUNCTION

Masonry and concrete buildings are two common types of buildings. The first material is often used in older and historical buildings and the non-load bearing walls of some modern concrete buildings. Concrete is mainly used for high-rise modern buildings. On the coastal dikes in Belgium, most buildings are low and medium rise masonry buildings those were constructed 50 to 100 years ago. In this study, we focus on the masonry type buildings with the seaward external wall panel of the ground floor as the key structural wall (load bearing wall or stability wall). The presented approach could also be applied to concrete buildings.

From the fault tree shown in Fig. 5.4, the failure of this type of external wall will lead to the collapse mode of the building. If the external wall is a non-structural wall, the failure of this wall may lead a local damage. The failure of a masonry external wall (including both the key structural and non-structural walls) consists of two basic failure modes: bending failure and shear failure when subjected to lateral overtopping wave loads. Since masonry is weak in tension, only the bending failure is considered in the current study. When designing masonry walls to resist lateral actions, shear strength of the walls need to be checked when the lateral resistance is large enough to withstand the design bending moment of the subjected load.

The bending failure of a masonry wall panel takes into account the conditions of the vertical and horizontal supports from the floors and the internal wall. The limit state function of the bending failure of a masonry wall G is expressed as:

$$G = M_R - M_S \tag{5.7}$$

where M_R is the lateral resistance capacity and M_S is the design moment of the lateral load. When $G < 0$, the wall panel status will be referred to bending failure. The subscripts "S" and "R" indicate the design load and the resistance respectively in the following sections.

DESIGN MOMENT OF THE LATERAL LOAD

For the design moment of the overtopping wave M_S can be conservatively determined by assuming the load is uniformly distributed over the entire wall panel by using the design moment in Eurocode 6 (British Standards Institution, 1996). The design moment, M_S, for a uniform distributed load over an entire wall panel:

$$M_S = \gamma_f \alpha q_k l^2 \tag{5.8}$$

where γ_f is the safety factor for load (load factor) [-], which is recommended to take value 1.0 in the accidental design situations in EN 1990 Annex A; α is a bending moment coefficient which depends on the orthogonal strength ratio μ, the support edge condition of the panels, and the height to length ratio of the panels, h/l; and l is the distance between the two vertical supports of the wall panel.

The bending coefficient α perpendicular to the bed joints is written as α_2, and that parallel to the bed joints is written as $\alpha_1 (\alpha_1 = \mu\alpha_2)$, see Fig. 5.A1 in Appendix 5.A. The orthogonal strength ratio μ depends on the unit and the mortar used, which takes into consideration the special characters of non-isotropy. The supports include the horizontal supports (e.g., floors, roofs, footings, beams) and vertical supports (cross walls, pilasters), see Fig. 5.6(a) and (b). Walls can be designed as one-way spanning with only considering two edge conditions for simplicity, or two-way spanning wall with considering the four edge conditions. The edge condition and the rigidity of the masonry wall determine the lateral resistance of the wall panel. There are three types of simplified edge conditions: free edge, simply supported edge, and fully restrained continuous edge. The examples of these edges are shown in Fig. 5.6(c). For a free edge, there is no moment and shear restraint. For a wall having a simply supported edge, it is often connected to a column or slab with ties. The direct force, shear and possibly moment are limited to the strength of ties. For a fully continuous restraint edge, the direct force and moment restraint are limited by the flexural strength of masonry. Thus the restraint developed at each edge of the wall can influence the lateral resistance of the wall panel (Moore, 2008).

LATERAL RESISTANCE

The lateral resistance capacity of a masonry wall panel is defined as:

$$M_R = \frac{f_{xk}}{\gamma_M} Z \tag{5.9}$$

where f_{xk} is characteristic flexural strength of masonry [N/mm^2], γ_M is the safety factor for material (material factor) [-] and Z is Elastic section modulus of a unit height or length of the wall [mm^3]. For the characteristic flexural strength f_{xk}, it is always expressed as f_{xk1} when considering the bending moment about an axis parallel to bed joints; If the bending moment about an axis is perpendicular to the bed joints, f_{xk2} is

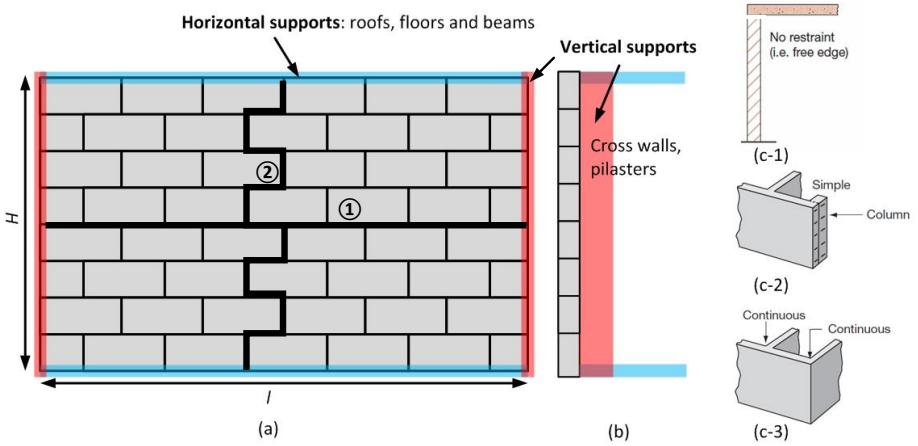

Figure 5.6: Support conditions of a plain masonry wall. (a) Front view of a plain wall with horizontal and vertical supports. (b) side view of a plain wall with horizontal and vertical supports. (c) examples of different edge conditions (Moore, 2008): (c-1) a wall built up to but not pinned to structure above with a free edge: no restraint. (c-2) a case of metal ties to columns with simple support: direct force restraint limited to strength of ties. (c-3) a case of bonded return walls with fully continuous restrained support: direct force and moment restraint limited by flexural strength of masonry.

used. Fig. 5.6(a) shows two plain failures of the wall parallel to the bed joints (line ①) and perpendicular to the bed joints (line ②). When a vertical load acts on the wall, the flexural strength will be increased in the direction parallel to the bed joints. Then $f_{xk}$is expressed as:

$$f_{xk} = f_{xk1} + \gamma_M \sigma_{d,min} \tag{5.10}$$

where $\sigma_{d,min}$ is the design vertical load [N/mm^2], which is only considered when the wall panel is designed as a load bearing wall. The material factor γ_M takes into account the material properties and construction method. For evaluating the existing buildings, the value of γ_M is suggested to set as 1.2 (Steenbergen and Vrouwenvelder, 2010). By substituting Eq. 5.8 and Eq. 5.9 into Eq. 5.7, the limit state function of the bending failure G for a masonry wall panel is obtained:

$$G = \frac{f_{xk}}{\gamma_M} Z - \gamma_f \alpha q_k l^2, \tag{5.11}$$

where γ_M and γ_f are suggested to take the value of 1.2 and 1.0 respectively. When the wall panel reaches its limit state ($G = 0$), the resistant capacity of the characteristic static pressure and overtopping run-up height of a wall can be calculated as:

$$q_{avg,R} = \frac{f_{xk}}{\gamma_M \gamma_f \alpha l^2} Z, \tag{5.12}$$

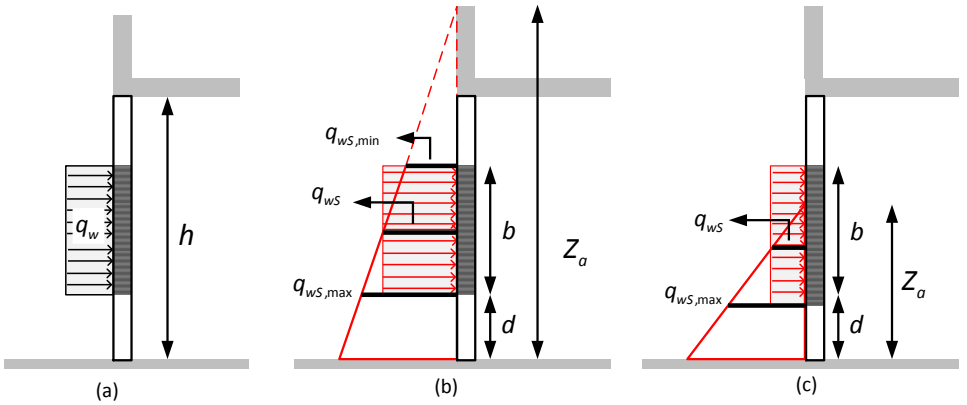

Figure 5.7: (a) Uniform distributed characteristic lateral load on windows; (b) linearly distributed hydrostatic load over the window when $Z_a \geq b+d$; (c) linearly distributed hydro-static load when $Z_a < b+d$.

and consequently, the equivalent run-up height that the building can withstand ($Z_{a,R}$) can be determined as:

$$Z_{a,R} = \begin{cases} \frac{q_{avg,R}}{\rho g} + \frac{1}{2}h & \text{for} \quad q_{avg,R} > \rho g h \\ \sqrt{\frac{2hq_{avg,R}}{\rho g}} & \text{for} \quad q_{avg,R} \leq \rho g h. \end{cases} \tag{5.13}$$

Since the load factor $\gamma_f = 1$, the actual subjected overtopping wave load equals to design load $q_{avg,S}$ or $Z_{a,S}$. When these values are larger than $q_{avg,R}$ and $Z_{a,R}$, we expect this wall panel to fail. If the wall panel is a key structural element (load bearing wall), collapse failure will occur. Otherwise, localized damage occurs.

5.3.3. FAILURE OF WINDOWS

Similar to the external wall, the failure of single pane glass windows in the external wall facing to the incident overtopping waves is analyzed. Due to the complexity of the glass failure mechanisms, Kelman (2002)'s simplified model is applied regarding the window pane as a simply supported thin plate.

EQUIVALENT STATIC LOAD

The equivalent static load on windows q_{wS} can be calculated by Eq. 5.14 and the illustrations of different loads subjected to the window are shown in Fig. 5.7. d is the elevation of the window, and b is the height of the window.

$$q_{wS} = \begin{cases} \rho g\,(Z_a - 0.5b - d) & \text{for} \quad Z_a \geq b+d \\ \frac{\rho g (Z_a - d)^2}{2b} & \text{for} \quad Z_a < b+d \end{cases} \tag{5.14}$$

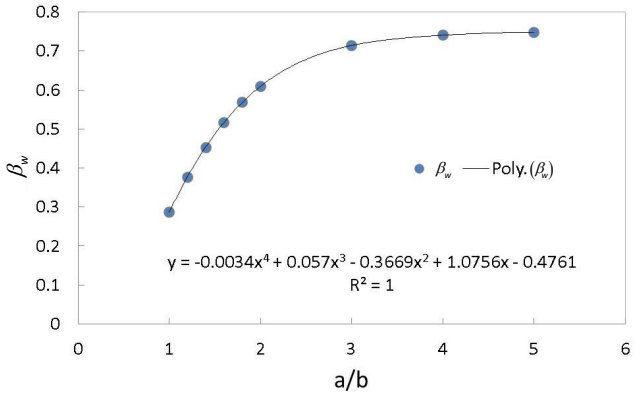

Figure 5.8: Empirical β_w of a thin plate with four edges simply supported based on thin plate theory.

LIMIT STATE FUNCTION

The limit state function of window is defined as:

$$G_w = \sigma_R - \sigma_s. \tag{5.15}$$

where σ_s is the applied overtopping load stress on the window. It can be calculated by using the following expression:

$$\sigma_s = \frac{\beta_w q_k b^2}{{t_g}^2} \tag{5.16}$$

where b is the height of the glass pane and t_g is the thickness of the glass pane; q_w is the characteristic uniform distributed load; β_w is the bending coefficient, which depends on the ratio of the length a and height b of the glass pane and the support condition of the four edges; t_g is the thickness of the glass pane. Fig. 5.8 shows an empirical determined bending coefficient curve for a simply supported thin plate. The strength value of glass pane with $\sigma_{R,50\%}$ = 60 MPa is used as the resistant strength of a window pane, which could be interpreted as approximately a 50% failure probability Kelman (2002). Thus, the resistant capacity of the static pressure of the window is defined when $G_w = 0$:

$$q_{wR} = \frac{\sigma_{R,50\%} {t_g}^2}{\beta_w b^2}. \tag{5.17}$$

If the actual subjected overtopping wave load q_{wS} is larger than q_{wR}, we expect this window to fail.

5.3.4. STEPS FOR VULNERABILITY ASSESSMENT

A summary of the procedure of assessing the vulnerability of buildings on the dike is given in Fig. 5.9. The approach consists three main steps: determination of hydraulic load conditions, calculation of the overtopping impact load and run-up height, and eval-

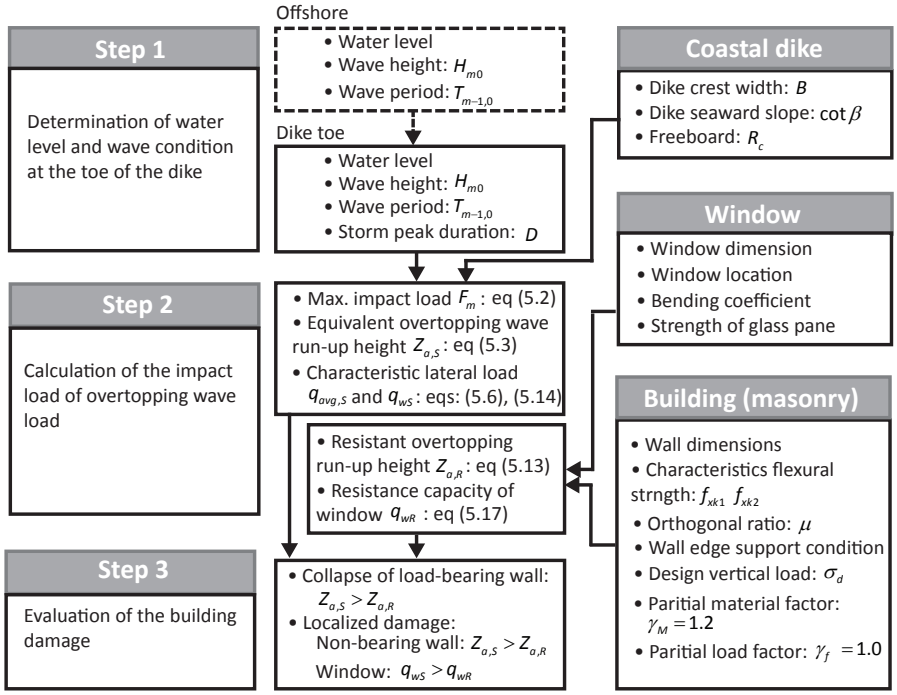

Figure 5.9: Flow chart for evaluation of the building damage.

uation of the structural vulnerability. In this study, only the water level, wave height and period at the toe of the dike in step 1 is used as input for step 2. If these conditions at the toe are not available, then extra calculation is needed by using offshore hydraulic condition in combination with either by numerical simulation or empirical determination (see dashed lines in Fig. 5.9). This extra calculation is not included in the present study.

5.4. CASE STUDY

In the previous sections, overtopping wave loads and the failure mechanisms of the building exposed to overtopping waves were introduced. Herein, a case study that uses the results from the previous sections is executed.

5.4.1. BELGIAN COASTAL DIKES

On coastal dikes in Belgium, many residential buildings are found. Most of the old buildings are masonry structures with two to three floors. The ground floors are always elevated and the entrances of the basements are closed by shutters (see Fig. 5.10). The most modern buildings are concrete reinforcement structures with concrete piles/columns as foundations. The walls are consisting of masonry or concrete. These buildings are normally 5 to 9 floors high. Some of the ground floors are elevated, and some are used as cafe, restaurant or store. The ground floors are equipped with large glass windows and

Figure 5.10: Typical old apartment buildings on the Belgian coastal dikes.

doors. A representative situation for Wenduine, a coastal town in Belgium, is used for the current case study. Fig. 5.11 shows the schematic sketch of a building placed on the top of the coastal dike in Wenduine[1]. The beach level is set at 6.5 m above TAW [2], which is chosen from the lowest toe position used in the study of Suzuki et al. (2016). The dike crest level is set at 8.5 m above TAW and the distance between the building to the seaward slope of the dike (B) is chosen as 10 m in this case study.

Two storm scenarios are considered for this case study, a storm with 1000 and 10000 years return periods. The storm surge levels are 7.22 m for 1000 year storm (S1) and 7.65 m for 10000 year storm (S2) based on Suzuki et al. (2016). For S1 and S2, the dike crest level (8.5 m above TAW) and beach level (6.5 m above TAW) are fixed, the corresponding water depth (h_{toe}) and freeboard (R_c) are determined. For S3, the same surge level with 10,000 years return period is used, but the toe of the dike is set as 4 m above TAW, as some cross sections have a relatively low toe position. The considered wave characteristics are $H_{m0,toe}$ and $T_{m-1,0}$, where H_{m0} is the mean spectrum significant wave height at the toe of the dike, and $T_{m-1,0}$ is the spectral wave period. The hydraulic conditions are shown in Table 5.1, and the detailed explanation of hydraulic conditions can be found in Appendix 5.B. The subjected overtopping wave load (run-up height along the wall) on the wall placed at 10 m away from the seaward slope of the dike is also shown in the same table.

[1] New storm walls have been installed recently in Wenduine. Therefore the case study in this paper is not applicable to the current situation in Wenduine. The original configuration of Wenduine dike before the new storm wall is used for case study.

[2] Tweede Algemene Waterpassing; Belgian standard datum level, situated near MLLWS

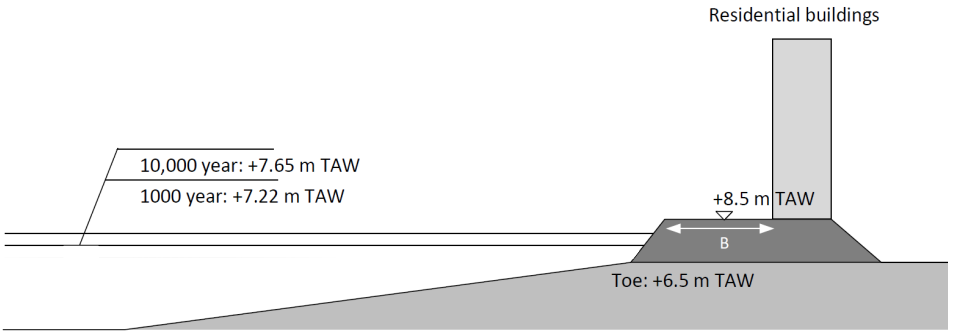

Figure 5.11: Schematic sketch of the building on the top of a coastal dike with different storm surges.

Table 5.1: Storms under different scenarios

	Return per. (year)	Dur. (hr.)	Surge (m+TAW)	Beach (m+TAW)	h_{toe} (m)	H_{m0} (m)	$T_{m-1,0}$ (s)	R_c (m)	$Z_{a,S}$ (m)
S1	1000	1	7.22	6.5	0.72	0.82	30.7	1.28	1.4
S2	10,000	1	7.65	6.5	1.15	1.03	33.3	0.85	2
S3	10,000	1	7.65	4	3.65	2.13	14.8	0.85	4.4

5.4.2. VULNERABILITY OF EXTERNAL MASONRY WALLS

REFERENCE MASONRY WALLS

The external wall of the ground floor is simply assumed as a section of the masonry wall, which is subjected to the overtopping wave load. If the external wall is a vertical load bearing wall or a stabilizing wall, the failure of this wall will cause the collapse of the whole building. If the external wall is a non-bearing wall, the failure of this wall is considered as localized damage.

The properties of plain masonry walls concerned in this case are selected from Eurocode 6, which are used as load bearing wall (LB) with the design vertical load is σ_d = 0.39 N/mm^2, and non-load bearing wall (NB) without considering the vertical load. This selection is expected to represent the typical masonry properties in Belgium. The construction materials are clay masonry unit Group 1 with mortar strength class M = 12 and water absorption ratio less than 7%. Since the aim of our study is to analyze the vulnerability of the existing buildings, the material factor γ_M is set as 1.2, and load factor γ_f is set as 1.0.

Due to the large influence of the edge supports on strength, four kinds of edge supports for the masonry wall panel are included in the analysis. Fig. 5.12 shows one non-load bearing wall (1-NB) with support condition A, and three sections of the load bearing masonry walls (1-LB) with σ_d = 0.39 N/mm^2 with different support conditions (E-I). The dimensions, support conditions, the resistance capacity of the characteristic equivalent static pressure $q_{avg,R}$ and equivalent overtopping run-up height $Z_{a,R}$ are shown in Table 5.2. The calculations of $q_{avg,R}$ and $Z_{a,R}$ of the masonry walls can be found in

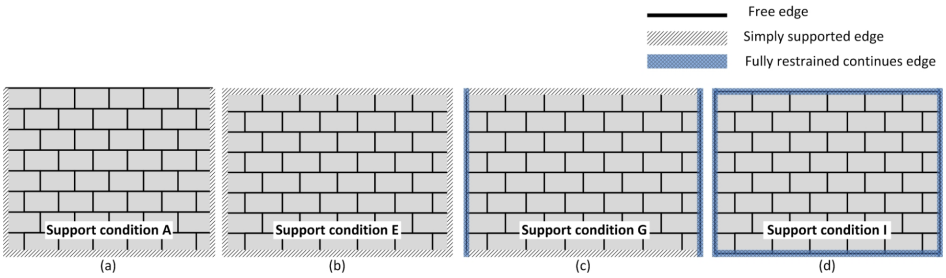

Figure 5.12: Wall panels for case studies. The name of the support condition of each wall panel is kept the same as that from Eurocode 6.

Table 5.2: Reference cases of the four sections of the plain wall 1 with support conditions A, E, G and I.

Plain wall	t_w (mm)	H_w (m)	l_w (m)	Area (m^2)	H/l	Support	$q_{w,avg}$ KN/m^2	$Z_{a,R}$ (m)
1-NB	220	2.9	5.8	16.82	0.5	A	6.24	1.92
1-LB	220	2.9	5.8	16.82	0.5	E	11.42	2.6
1-LB	220	2.9	5.8	16.82	0.5	G	15.98	3.07
1-LB	220	2.9	5.8	16.82	0.5	I	23.51	3.73

Appendix 5.E.

INFLUENCE OF THE INCIDENT WAVE HEIGHT

An example of the vulnerability of the four masonry walls (see Table 5.2) exposed to the maximum overtopping wave load under S1 (1000 year condition) with a peak duration of 1 hour (see Table. 5.1) is presented.

In Fig. 5.13, the x-axis indicates the mean spectrum wave height at the toe of the dike, and the y-axis is the equivalent overtopping run-up height Z_a. The four horizontal lines are the resistance capacity expressed by the equivalent overtopping run-up height $Z_{a,R}$ for the wall panels, indicating the limits of the different wall configurations. The three lines with different markers indicate the subjected overtopping wave run-up height $Z_{a,s}$ by using S1, S2 and S3 with varied wave heights rising from 0.8 meter to 2.5 meter. If the horizontal lines lie below the continuous lines then the building might collapse, and if the horizontal lines lie above the continuous lines then the masonry wall can withstand the impact load. For the 1000 year condition with expected wave height 0.82 m, no damage to the wall is expected. But for 10,000 year condition with the expected wave height of more than 2.1 m, building collapse might be expected for most typical wall configurations.

INFLUENCE OF THE BUILDING LOCATION

Widening the crest of a coastal dike can dissipate the kinetic energy of overtopping waves (Verwaest et al., 2010). Chen et al. (2016) proposed an empirical formula for the overtopping wave load that takes into account the variation of the locations of the building on

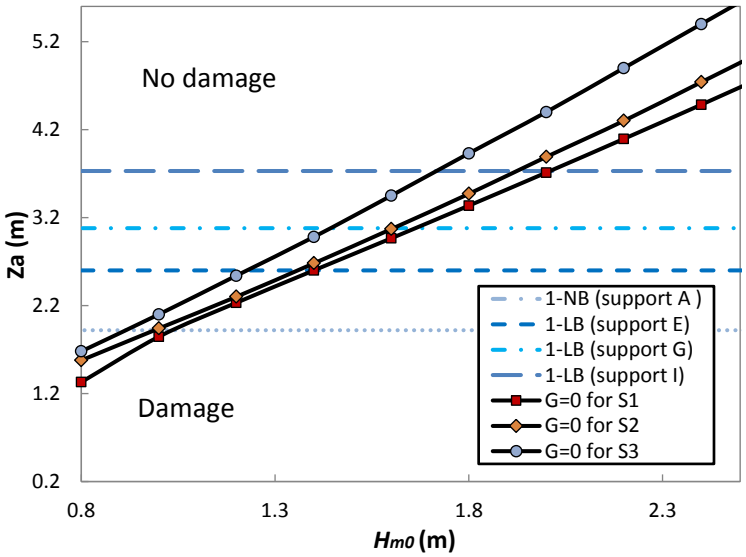

Figure 5.13: Damage curve for four plain masonry walls located at $B = 10$ m with varying wave height.

the dike. The vulnerability of the building located at different positions can be investigated using the formulas from Chen et al. (2016).

Fig. 5.14 shows the results of the vulnerability analysis of the four walls located at 3 to 33 meters away from the seaward dike slope. The four horizontal dashed lines are the resistance capacity of the equivalent overtopping run-up height $Z_{a,R}$ for the wall panels. The curved solid lines with markers indicate the equivalent overtopping run-up heights calculated based on the three scenarios shown in Table 5.2 with varying B. It can be seen that no wall failure is expected under condition S1 even if buildings are quite close to the coast. For condition S2, the overtopping wave load decreases significantly when B is larger than 28 meters. Only the non-load bearing wall (1-NB) is expected to break if it is located less than 20 meters on the dike. Then it is suggested that only the local damage of the building would occur, but no collapse.

For the condition of S3, the cross section of the dike is different from the other two conditions. The beach level at the toe is low (4 m +TAW) which resulting a greater water depth in front of the dike. Thus, the wave characteristics change. The wave breaking is not so severe as in shallower conditions; therefore the incident wave height at the toe of the structure is higher with consequent more overtopping discharge and larger waves will impact on the building. The overtopping wave impact load under condition S3 is serious as well. The damage caused by the wave load of S3 is expected for the most support conditions.

INFLUENCE OF THE WALL DIMENSIONS

The dimensions of the wall panels can influence the lateral resistance. Fig. 5.15 shows an example of the influence of the width of the wall panel (wall height is fixed at 2.9 m)

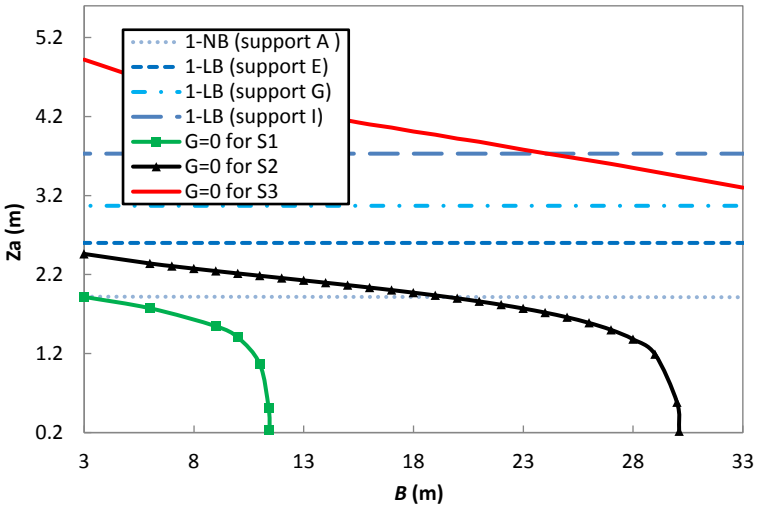

Figure 5.14: Damage curve for the four plain masonry walls with varying B

on the resistance capacity of the equivalent overtopping run-up height $Z_{a,R}$ according to eq. (5.13). It can be seen that $Z_{a,R}$ increases with decreasing the masonry wall width. It suggests that the lateral resistance can be increased by designing a smaller wall section.

Fig. 5.16 shows another example of the influence of the thickness of the wall panel. The thickness of wall 1 (see Table. 5.2) is varied. It can be seen that the resistance capacity of the equivalent overtopping run-up height $Z_{a,R}$ increases with increasing the wall thickness. It is suggested that the lateral resistance can be increased by designing a thick section wall.

5.4.3. DAMAGE OF WINDOWS

The windows are typically located 0 to 1 meter from the ground. The width of window glass pane is 1 to 3m, and the height is 0.5 to 2m. Double glazed window is the common type. The equivalent thickness of double glazed window is 8 mm. Four window glass panes (WD) with different sizes are analyzed, which are assumed as thin plates with four simply supported edges. The windows with large piece of glass pane are located at the ground floor ($d = 0$ m). The other one is the normal window located above the ground. Four pieces of window pane are analyzed, see Table 5.3. The meaning of each parameter can be found in Fig. 5.17. An example of the vulnerability of the glass window on an external wall under condition S1 (see Table 5.2) is provided. The building is located 10 meter behind the seawards dike crest ($B = 10$ m). In Fig. 5.18, the x-axis indicates the mean spectrum wave height at the toe of dike, and the y-axis is the equivalent lateral load q_{wS}, based on the calculated Z_a (Eq. 5.3) multiplied by factor 1.58, concerning the dynamic effect during the 1 hour storm peak. The damage of the window unit WD-1, WD-3 and WD-4 are analyzed. The three solid horizontal lines (q_{wR}) in Fig. 5.18 indicate the resistant capacity of each window calculated by using the maximum strength

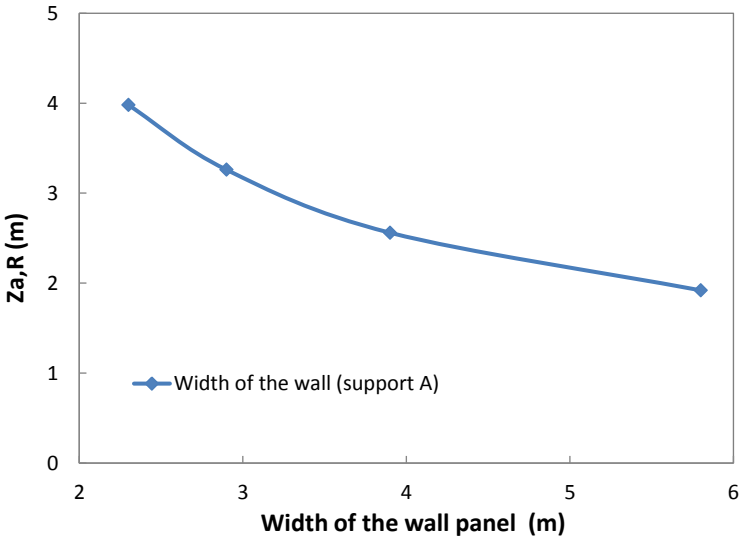

Figure 5.15: The influence of the size of the wall panel on the lateral resistance of the wall.

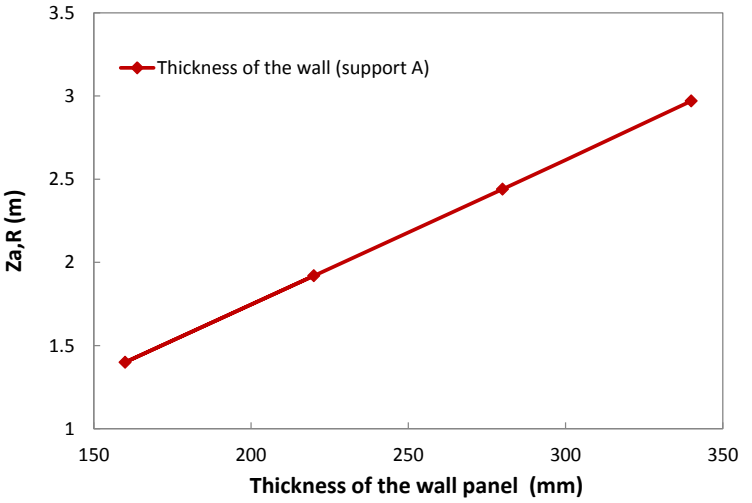

Figure 5.16: The influence of the wall panel thickness on the lateral resistance of the wall.

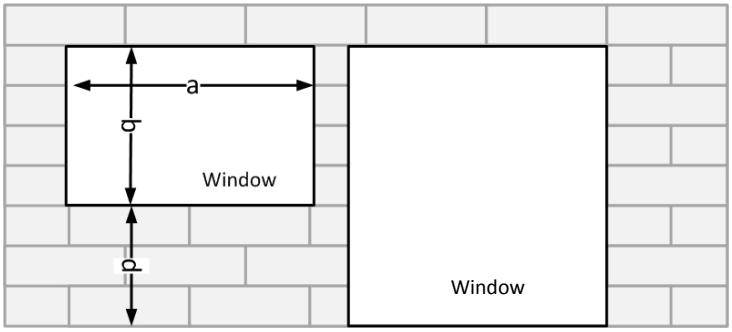

Figure 5.17: Dimensions and location of windows.

Table 5.3: Dimensions of windows

Window unit	d (m)	t_g (mm)	a (m)	b (m)	R (m^2)	a/b (m)	β_w (m)
WD-1	0	8	3	2	6	1.5	0.487
WD-2	0	8	2	2	4	1	0.286
WD-3	1	8	3	1	3	3	0.712
WD-4	1	8	1	0.5	0.5	2	0.609

$\sigma_{R,50\%}$ = 60 Mpa with a failure probability of 50%. The three solid line with markers (q_{wS}) indicate the subjected load on the window. For the window WD-1, its resistance capacity, q_{wR} (WD-1), is always below the subjected overtopping wave load, q_{wS} (WD-1). It means that the window WD-1 with the maximum strength of 60 MPa will fail during the considered storm conditions. Whereas for the window WD-4, its resistance capacity, q_{wR} (WD-4), is always above the subjected overtopping wave load, q_{wR} (WD-4) when H_{m0} is greater than about 1.3 m. It means that the window can survive during the considered storm conditions. Comparing the resistance of the two window WD-1 and WD-4, it suggests that the windows on the external wall would not survive during a 1000-year storm. If the size of the window is small, there is no threat from overtopping wave for the windows located at a certain distance above the ground.

5.5. CONCLUSION

The flood risk caused by the direct impact of wave overtopping on coastal buildings is regarded as a highly interesting but not yet sufficiently well-developed area of research Allsop et al. (2008). This paper investigated the vulnerability of buildings placed on a coastal dike and a case study for the Belgian coast.

A method has been developed that takes into account the hydraulic loads, overtopping process, equivalent overtopping wave run-up height at the vertical wall, and failure mechanisms and strength of the building. From the Belgian case study, the overall results indicate that windows of the ground floor will be broken under a storm with 1000

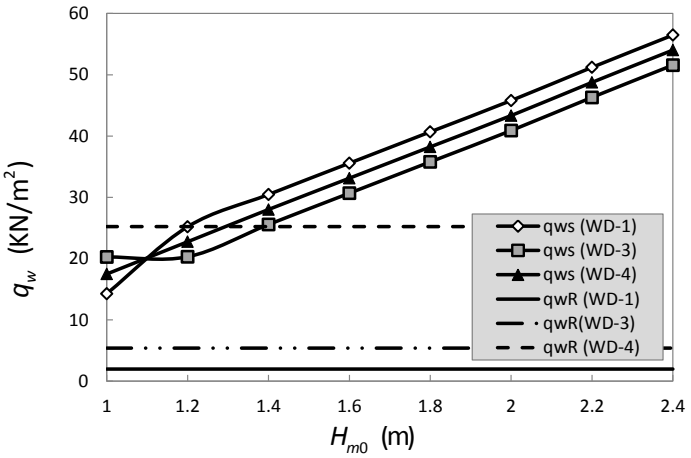

Figure 5.18: Failure of three windows located at B=10 m for storm condition of S1 with varying wave height.

years return period. If a 10,000 year storm occurs, the masonry buildings located at less than 20 meters away from the seafront will suffer from localized damage due to the failures of window breaking and non-load bearing wall failure. If a 10,000 year storm occurs but the beach level at the toe of the dike is lowered such as the condition S3, most of the load bearing external walls and stability walls are expected to fail when the buildings are located near the coast.

The location of the buildings on the dike is limited by the width of the dike crest. Thus, it is recommended to increase the strength of the external wall on the ground by providing extra supports, and to reinforce the windows when designing a building on the dike. If the beach level is lowered, the local waves conditions and expected overtopping wave loads will increase and this would lead to expected collapse of the building. Thus, beach nourishment is also important for protection of buildings. In the future, more effort should be put on the influence of beach profiles on wave overtopping.

It should be noted that this study has been primarily concerned with the existing masonry buildings with material factor $\gamma_M = 1.2$. The results can be used to provide suggestions when designing new masonry on the top of the dike but γ_M need to change. The approach can be extended with a strength model for other structure types such as concrete buildings.

The assessments in this study are based on semi-probabilistic analysis by using partial safety factors from the Eurocodes. However, since both resistance and strength will have a statistical variation, it is recommended to use a probabilistic approach to predict the likelihood of failure of buildings on the coast during their lifespan. The question which probability of collapse or localized damage is acceptable has to be answered by the various stakeholders such as the owner, the government and other people whose life is in some way influenced by a possible failures. Arguments can be social, economic or otherwise. Based on the findings of the case, it is suggested to further evaluate the risk of building collapse and associated risk for people living on the Belgian and Dutch coast.

APPENDIX

5.A. SUPPORT CONDITIONS OF THE WALL

Fig. 5.A1 shows 12 different wall support conditions used in Eurocode 6 (Robert and Brooker, 2007). Some of conditions were used for the case study.

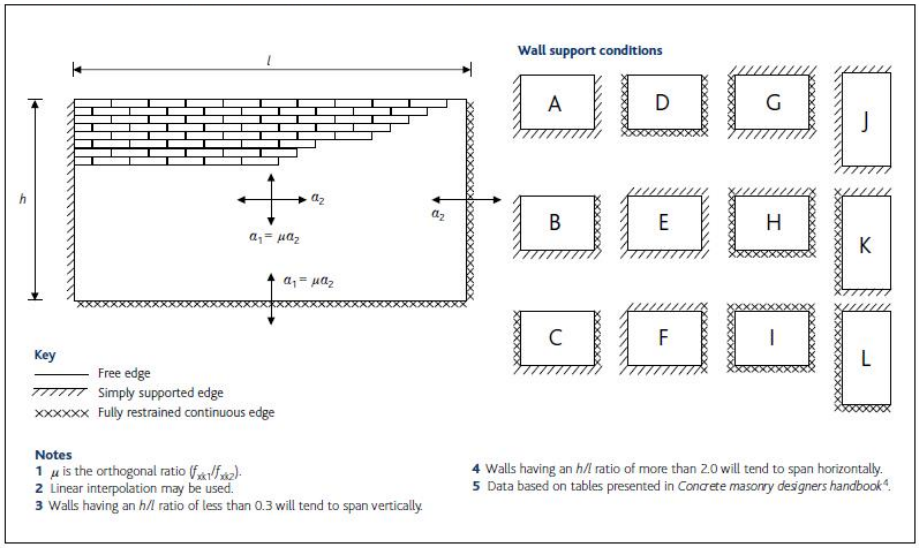

Figure 5.A1: Wall support conditions (Eurocode 6).

5.B. HYDRAULIC BOUNDARY CONDITIONS

The hydraulic boundary conditions of the considered storms shown in Table 5.1 are determined as follows.

1. Collection of offshore data
   The storm surges with a return period 1000 and 10,000 years are decided based on Peak-Over-Threshold (POT) analysis. The data observed from the offshore buoys are determined independently, including representative water level (1925-2014) and wave properties (1984-2014).

2. Numerical simulation
   The wave transformation from offshore to the toe of the dike is estimated by numerical simulations with two different numerical models: SWAN and SWASH.

- Offshore to nearshore
  The collected data from offshore are used as the input hydraulic boundary conditions of SWAN. The wave transformation from offshore to nearshore is calculated until 5 meter below the Belgian standard datum level (TAW).
- Nearshore to the toe of dike
  The transformation of waves from nearshore (-5 m TAW) is calculated till the toe of the dike. The output of SWAN is used for the input hydraulic boundary condition of SWASH. The outputs of SWASH which are used for the overtopping wave load calculation include: H_{m0} and $T_{m-1,0}$.

The work of estimation H_{m0} and $T_{m-1,0}$ for this case study was carried out by Dr. Tomohiro Suzuki from Flanders Hydraulic Research. Details of the calculation can be referred to Suzuki et al. (2016).

5.C. OVERTOPPING WAVE LOAD

5.C.1. EMPIRICAL GP DISTRIBUTION

This section briefly introduced the procedure of the application of empirical Generalized Pareto (GP) distribution proposed by Chen et al. (2016) to estimate the expected maximum overtopping wave load for a certain storm peak duration. Six key parameters need to calculated before F_m: overtopping wave impact probability P_{im}, maximum overtopping force exceedance probability P_{max}, characteristic force F_c, empirical threshold F_u, GP distribution scale parameter σ, and shape parameter k.

(1). Calculate the overtopping force impact probability P_{im}:

$$P_{im} = -0.06 \ln\left(\frac{B}{L_t}\frac{R_c}{H_{m0}}\right) - 0.09, \tag{5.C1}$$

(2). Calculate the expected maximum overtopping force exceedance probability:

$$P_{max} \approx T_{m-1,0}/D. \tag{5.C2}$$

(3). Calculate the characteristic force F_c:

$$F_c = \rho g \left[H_{m0}\left(1 - \frac{R_c}{R_{u,2\%}}\right)\right]^2 \tag{5.C3}$$

where R_u is the 2% wave run-up height, which is empirically calculated by using the formula proposed by Van Gent (2001) for shallow water environment.

(4). Calculate the empirical threshold F_u:

$$\frac{F_u}{\rho g H_{m0} R_c} = 0.84 \exp\left(0.36 \frac{F_c}{\rho g H_{m0} R_c}\right) \tag{5.C4}$$

(5). Calculate the empirical scale parameter σ:

$$\frac{\sigma}{\rho g H_{m0} R_c} = 0.37 \exp\left(0.37 \frac{F_c}{\rho g H_{m0} R_c}\right). \tag{5.C5}$$

(6). Calculate the empirical shape parameter k:

$$k = -0.59 \ln\left(\frac{\sigma}{\rho g {H_{m0,t}}^2}\right) - 0.34. \tag{5.C6}$$

(7). Calculate the expected maximum overtopping force F_m and its uncertainty range for a storm peak duration D:

$$\begin{cases} F_m = F_u + \frac{\sigma}{k}\left[\left(\frac{P_{im}}{P_{max}}\right)^k - 1\right], \ k \neq 0 \\ F_m = F_u + \sigma \ln\left(\frac{P_{im}}{P_{max}}\right), \ k = 0 \end{cases} \tag{5.C7}$$

The performance of the empirical GP distribution is evaluated by comparing the calculated F_m with the maximum overtopping force estimated by fitting a GP distribution to experimental data. Details can be found in Chen et al. (2016).

5.C.2. EXAMPLE OF OVERTOPPING WAVE FORCE

GIVEN:

1/10,000 storm with 1 hour is used as the design condition in this example to calculate the expected maximum overtopping wave load on a building located 10 meters away from the seaward slope of the dike respectively. The information of the dike geometry parameters and wave conditions are shown below:

Dike geometry parameters:

Dike crest level is 8.5 m above TAW (Belgium reference water level), seaward dike slope $\cot\beta$ is 3, beach slope in front of the dike is 1:50, B = 10 m.

Wave conditions at the toe of the dike:

H_{m0} = 1.03 m, $T_{m-1,0}$ = 33.3 s, surge=7.65 m, water depth at the toe h_{toe} = 1.15 m, freeboard R_c = 0.85 m

QUESTIONS:

Q1. Wave run-up height $R_{u,2\%}$

Q2. Maximum ovcertopping wave load F_m on the buildings during a 1 hour storm surge

Q3. Equivalent overtopping wave run-up height $Z_{a,S}$ along the building

SOLUTIONS:

A1. Van Gent (2001) investigated the wave run-up on the dikes with a shallow foreshore in the front. The results show that the wave period $T_{m-1,0}$ is the best characteristic period for the coastal processes like wave run-up and overtopping in

Table 5.C1: Coefficients in Eq. (5.C8) for wave run-up predictions. $c_2 = 0.25c_1^2/c_0$ and $p = 0.5c_1/c_0$, and σ_{std} are the correspondent standard deviations (Van Gent, 2001).

Wave energy spectra	Wave height	Wave period	c_0	c_1	σ_{std}
Total: long and short waves	H_{m0}	$T_{m-1,0}$	1.45	3.8	0.24
Total: long and short waves	H_s	$T_{m-1,0}$	1.35	4.7	0.37
Short waves only	H_{m0}	$T_{m-1,0}$	1.45	5.0	0.51
Short waves only	H_s	$T_{m-1,0}$	1.55	5.4	0.63

shallow water. The empirical formula for $R_{u,2\%}$ with shallow foreshore conditions is shown in Eq. (5.C8) for breaking wave ($\xi_{m-1,0} \leq p$) and non-breaking waves ($\xi_{m-1,0} > p$), and the correspondent coefficients in Eq. (5.C8) are shown in Table 5.C1. This equation is used in this study for the analysis of overtopping wave force in Chapter 4.

$$\begin{cases} R_{u2\%}/H_{m0} = c_0\xi_{m-1,0} & \text{for } \xi_{m-1,0} \leq p \\ R_{u2\%}/H_{m0} = c_1 - c_2/\xi_{m-1,0} & \text{for } \xi_{m-1,0} > p \end{cases} \tag{5.C8}$$

Determine c_2 and p:

In this study, total wave energy spectra including long and short waves is applied. Thus $c_0 = 1.45$ and $c_1 = 3.8$, see Table 5.C1. Then c_2 and p can be calculated as:

$c_2 = 0.25{c_1}^2/c_0 = 0.25 \times 3.8^2/1.45 = 2.49$

$p = 0.5c_1/c_0 = 0.5 \times 3.8/1.45 = 1.31$

Determine $\xi_{m-1,0}$:

$\xi_{m-1,0} = \frac{\tan\beta}{\sqrt{H_{m0}/1.56{T_{m-1,0}}^2}} = \frac{1/3}{\sqrt{1.03/(1.56\times 33.3^2)}} = 13.6 > 1.31$

Determine $R_{u2\%}$:

$R_{u2\%} = H_{m0}\left(c_1 - c_2/\xi_{m-1,0}\right) = 1.03 \times (3.8 - 2.49/13.6) = 3.72$ m

A2. F_m can be calculated by following the procedure shown in Section 5.C.1:

(1). Calculate the overtopping force impact probability P_{im}:

$P_{im} = -0.06\ln\left(\frac{B}{T_{m-1,0}\sqrt{gh_t}}\frac{R_c}{H_{m0}}\right) - 0.09 = -0.06 \times \ln\left(\frac{10}{33.3\sqrt{9.8\times 1.15}}\frac{0.85}{1.03}\right) - 0.09 = 0.072$

(2). Calculate the expected maximum overtopping force exceedance probability $P_{\max}$:

$P_{\max} \approx T_{m-1,0}/D = 33.3/3600 = 0.0092$

(3). Calculate the characteristic force F_c:

$F_c = \rho g\left[H_{m0}\left(1 - \frac{R_c}{R_u}\right)\right]^2 = 1000 \times 9.8 \times \left[1.03 \times \left(1 - \frac{0.85}{3.72}\right)\right]^2 = 6194$ N/m

(4). Calculate the empirical threshold F_u:

$F_u = \rho g H_{m0} R_c \cdot 0.84\exp\left(0.36\frac{F_c}{\rho g H_{m0} R_c}\right) = 9346$ N/m

(5). Calculate the empirical scale parameter σ:
$\sigma = \rho g H_{m0} R_c \cdot 0.37 \exp\left(0.37 \frac{F_c}{\rho g H_{m0} R_c}\right) = 4146$ N/m

(6). Calculate the empirical shape parameter k:
$k = -0.59 \ln\left(\frac{\sigma}{\rho g {H_{m0}}^2}\right) - 0.34 = 0.2$

(7). Calculate the expected maximum overtopping force F_m:
Since $k = 0.2 \neq 0$, F_m can be calculated as:
$F_m = F_u + \frac{\sigma}{k}\left[\left(\frac{P_{im}}{P_{\max}}\right)^k - 1\right] = 9346 + \frac{4146}{0.2}\left[\left(\frac{0.072}{0.0092}\right)^{0.2} - 1\right] = 19899$ N/m

A3. Equivalent overtopping wave run-up height Z_a can be calculated as:
$Z_{a,S} = \sqrt{\frac{2F_m}{\rho g}} = \sqrt{\frac{2 \times 19899}{1000 \times 9.8}} = 2$ m

5.D. PARTIAL SAFETY FACTORS

Partial factor method as described in the Eurocode both the load on and the resistance or strength of a structure are supposed to have a certain statistical variation. Therefore theoretically the collapse of a structure is not something that can be predicted with a 100% certainty. The only thing that can be predicted is a chance of collapse in the remaining life span. The question what chance of total or partial collapse is acceptable has to be answered by the various stakeholders such as the owner, the government and other people whose life is in some way influenced by a possible collapse. Arguments can be social, economic or otherwise and the content and the weight of each argument can differ in time.

In EN 1990, Annex A recommended values are given for partial safety factors for the design values of actions in the Ultimate Limit State (ULS). These can be used for the design verification of new buildings. Typical values are 1.1 for permanent loads and 1.5 for variable loads. The partial factors for loads for the ultimate limit states in the accidental design situations are given as 1.0. An accidental design situation is described as a design situation involving exceptional conditions of the structure or its exposure, including fire, explosion, impact or local failure. Recommended values for the material factors are specified in the various materials related parts of the Eurocode, e.g. EN 1996 for masonry.

Steenbergen and Vrouwenvelder (2010) have made recommendations for the partial safety factors for existing structures. They argue that it would be uneconomical to require all existing buildings to comply fully with the new codes and corresponding safety levels. They argue for load factors that are lower than those for loads on new buildings based on economic considerations and a shorter design life. The material factors remain unchanged.

What load factors γ_f and material factors γ_M are used in calculations depends on the type of building, the age, the consequences of collapse and, very important, the chance of occurrence of the load. According to Vrouwenvelder (2005), the difference between a normal variable load and an accidental load is that the variable load is often or nearly always present, although its value may be small for a substantial part of the time. A typical accidental load, on the other hand, will most probably not occur during the working

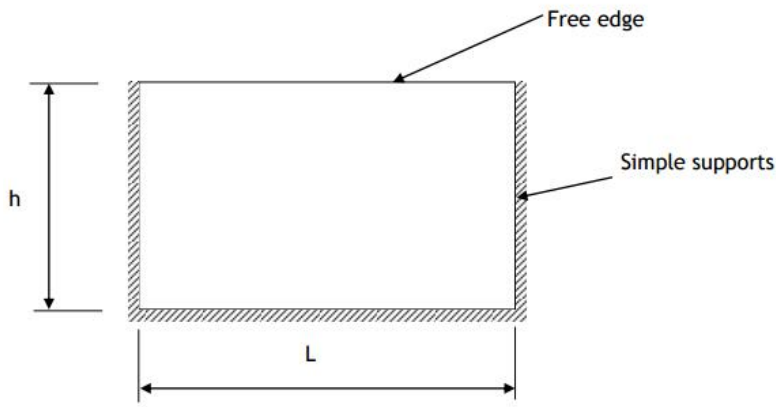

Figure 5.E1: Wall support conditions (Eurocode 6).

life of the structure. If the load is present, it normally will take only a short time, varying from a few seconds (explosions) to some days (floods). Accidental loads should have a probability of 0.98 per year or more to be zero.

The impact load from overtopping waves is assumed as an accidental loading. This is done under the additional assumption that the collapse of a coastal building does not influence the overall stability of the dike. The acceptability of this assumption will have to be assessed on a project-by-project basis. The partial load factor γ_f is taken as 1.0, and the material factor γ_M is taken as 1.2.

5.E. EXAMPLE OF THE WALL RESISTANCE

GIVEN:

The information of the target wall (in Table 5.E1) is shown in Fig. 5.E1 using the following criteria:

Construction materials:

Clay masonry unit Group 1, with mortar strength class M=12, water absorption ratio less than 7%.

Partial safety factor: $\gamma_M = 1.2$, $\gamma_f = 1$

Design vertical load: $\sigma_d = 0.39$ N/mm^2.

As comparison group, wall unit 1 with other three support conditions are also listed in Table 5.E1, the support conditions can refer to Fig. 5.A1.

SOLUTION:

The design bending moment per unit length of the wall depends on bending moment coefficient. The bending moment coefficient α_1 depends on:

- orthogonal ratio
- aspect ratio h/L

Table 5.E1: A Wall panel dimensions for analysis

Wall unit	t_w (mm)	h (m)	l (m)	Area (m^2)	h/l	support
1-NB	220	2.9	5.8	16.82	0.5	A
2-NB	220	2.9	3.9	11.21	0.75	A
3-NB	2.9	2.9	8.41	8.41	1.0	A
4-NB	220	2.9	2.3	6.73	1.25	A
5-NB	160	2.9	5.8	16.82	0.5	A
6-NB	280	2.9	5.8	16.82	0.5	A
7-NB	340	2.9	5.8	16.82	0.5	A
1-LB	220	2.9	5.8	16.82	0.5	E
1-LB	220	2.9	5.8	16.82	0.5	G
1-LB	220	2.9	5.8	16.82	0.5	I

Table 5.E2: bending coefficient of wall unit 1 to 4 for analysis

Wall unit	Support	h/l	μ	α	$\alpha_1 = \mu\alpha_2$
1-NB	A	0.5	0.35	0.064	0.022
2-NB	A	0.75	0.35	0.080	0.028
3-NB	A	1.0	0.35	0.089	0.031
4-NB	A	1.25	0.35	0.095	0.033
1-LB	E	0.5	0.35	0.035	0.012
1-LB	G	0.5	0.35	0.025	0.009
1-LB	I	0.5	0.35	0.017	0.006

- edge support conditions

a. For clay masonry unit Group 1, with mortar strength class M=12, water absorption ratio less than 7%

   Determine f_{xk1}:
   For clay masonry unit at 220 mm thick, $f_{xk1} = 0.7$

   Determine f_{xk2}:
   For clay masonry unit at 220 mm thick, $f_{xk2} = 2$

   Orthogonal ratio μ:
   $\mu = \frac{f_{xk1}}{f_{xk2}} = \frac{0.7}{2} = 0.35$

b. Aspect ratio=h/l, see Table 5.E1;

c. Support condition A, E, G, and I

   In appendix, different wall support condition and bending coefficient table are given. By interpolation, α_2 with different aspect ratio and correspondent α_1 are shown in Table 5.E2.

Table 5.E3: A Wall panel dimensions for analysis

Wall unit	t_w (mm)	H (m)	I (m)	Area (m^2)	H/l	Support	$q_{w,avg}$ (KN/m^2)	$Z_{a,R}$ (m)
1-NB	220	2.9	5.8	16.82	0.5	A	6.24	1.92
2-NB	220	2.9	3.9	11.21	0.75	A	11.04	2.56
3-NB	220	2.9	2.9	8.41	1.0	A	17.96	3.26
4-NB	220	2.9	2.3	6.73	1.25	A	26.75	3.97
5-NB	160	2.9	5.8	16.82	0.5	A	3.3	1.49
6-NB	280	2.9	5.8	16.82	0.5	A	10.08	2.44
7-NB	340	2.9	5.8	16.82	0.5	A	14.92	2.97
1-LB	220	2.9	5.8	16.82	0.5	E	11.42	2.6
1-LB	220	2.9	5.8	16.82	0.5	G	15.98	3.07
1-LB	220	2.9	5.8	16.82	0.5	I	23.51	3.73

d. Maximum resistant moment

Based on the previous given information and calculations, $f_{xk1} = 0.7\,N/mm^2$, t_w=220 mm, and the wall $\sigma_d = 0.39\,N/mm^2$. Then design moment can be calculated following Eq. 5.8: $M_s = \alpha_{1,2} q_{w,avg} l^2$

d-1 The design resistance moment of wall unit 1 parallel to the bed joints:

$M_1 = \left(\frac{0.7}{1} + 0.39\right) \times \frac{220^2 \times 10^{-3}}{6} = 8.79\ KN{\cdot}m/m$

d-2 The design resistance moment of wall unit 1 perpendicular to the bed joints:

$M_2 = \left(\frac{2}{1}\right) \times \frac{220^2 \times 10^{-3}}{6} = 16.13\ KN{\cdot}m/m$

d-3 Then the design equivalent load $q_{w,avg}$ of the correspondent M is:

When the plane of failure is parallel to the bed joints:
$q_{w,avg,1} = \frac{M_1}{\gamma_f \gamma_M \alpha_1 l^2} = \frac{8.79}{1.0 \times 1.2 \times 0.022 \times 5.8^2} = 9.89\ KN/m^2$

When the plane of failure is perpendicular to the bed joints:
$q_{w,avg,2} = \frac{M_2}{\gamma_f \gamma_M \alpha_2 l^2} = \frac{16.13}{1.0 \times 1.2 \times 0.064 \times 5.8^2} = 6.24\ KN/m^2$

d-4 The minimum pair of design failure loads is selected $q_{w,avg,2}$, which means the wall will failure in the direction perpendicular to the bed joints first.

e. Maximum overtopping wave run-up height

With the assumption of $q_{w,avg}$ uniformly distributed over the entire wall plate, the maximum overtopping wave run-up height $Z_{a,R}$ is:

$Z_a = \sqrt{\frac{6.24 \times 1000 \times 2 \times 2.9}{1000 \times 9.8}} = 1.92$ m.

The results of all wall units from Table 5.E1 are shown in Table 5.E3.

6

CONCLUSIONS AND RECOMMENDATIONS

In the present work, a prediction method for the impact loads resulting from wave overtopping was developed and an approach for assessing the vulnerability of buildings was provided. First, the overtopping wave in the context of understanding wave overtopping and its impact progress (Chapter 2) was investigated, with consideration of an effect of the interaction between two successive waves on the impact mechanism. Next, it was explored how the impact force of an overtopping wave is correlated to the incident wave characteristics and dike geometry parameters in shallow water, not only for a single overtopping wave but also for the prediction of the maximum wave during a storm peak through extreme value analysis (Chapters 3 and 4). Then the vulnerability of buildings on the top of the dike crest was assessed by applying the developed empirical formulas for the maximum overtopping wave force, taking into account the localized damage and collapse failure mechanisms of the building (Chapter 5). This chapter will summarize the main results and give some perspectives on future developments and applications.

6.1. CONCLUSIONS

The main goal of this dissertation was to study the overtopping wave impact for the situation of buildings on the top of coastal dikes where a shallow foreshore affects the wave overtopping, and to provide a method to assess the vulnerability of buildings on the top of coastal dikes due to the impact of wave overtopping. To fulfill this goal, this dissertation has provided answers to the research questions formulated in Chapter 1.

6.1.1. IMPACT MECHANISM OF OVERTOPPING WAVES

There is little literature about the impact process of an overtopping wave, which is a mixture of moving water and air. In order to develop practical approaches to design and assess structures, understanding physical force-generating mechanisms is necessary. In Chapter 2, the impact of overtopping waves was investigated.

The impact process and mechanism of a single overtopping wave were presented based on the observations from the physical model tests by using regular waves. For a single overtopping wave, the whole impact process can be summarized as four stages: pre-impact, initial impact, deflection, and reflection. Based on two different dominant physical mechanisms during the impact, the time series of the force has two distinct peaks. The first one named as the dynamic peak occurs with the transformation of the kinetic energy of the incident overtopping wave to the potential energy with a short duration. The other one named as the quasi-static peak occurs during the deflection and reflection stages when the gravity force is dominant. This peak is characterized by a quasi-static force with relatively long duration.

In comparison with observations in regular wave tests, different interaction patterns of successive waves in front of the wall were observed from the tests with bichromatic and irregular waves. The two basic patterns,"collision" and "catch-up", are similar to the swash motion in a shallow water environment. If the two waves interact in an opposite direction, a collision is expected. When this occurs near the wall, an air cavity may be formed which would result in a kind of impulsive breaking wave impact. If the two waves interact in the same direction, a catch-up is expected. The time lag between the interaction moment of the two waves and the time of the initial wave impact on the wall seems critical for the impact mechanism of the overtopping wave.

6.1.2. IMPACT FORCE CHARACTERIZATION

As an initial step toward establishing an empirical formula for overtopping wave forces on structures, the relationship between the overtopping wave force and the features of a single overtopping wave was investigated in Chapter 3.

The overtopping momentum flux is a function of the properties of the incoming waves and dike geometry characteristics, which is found particularly relevant to the overtopping wave impact force. An empirical formula was proposed for the resulting overtopping wave impact forces on a wall as a function of the overtopping momentum flux. A series of physical model tests with regular waves were conducted. The incident wave height and period at the position of the dike toe, overtopping wave layer thickness at the beginning of the seaward dike crest, and resulting impact force on a vertical wall at different locations on the dike were measured. The proposed empirical formula was verified by experimental data, demonstrating good performance. The measured forces were col-

lected by load cells, however, which do not resolve the dynamic impact force peak with a short-duration. Thus, the results from this study should only be used for the large structures on the dike crest with a low natural frequency. The interaction (e.g., catch-up and collision patterns) between overtopping waves was left out here for a basic understanding of the quasi-static peak of the overtopping wave impact load that provides large total force on large structures. The "extreme impact force" induced by the overtopping waves does does include these effects which is illustrated in the following subsection.

6.1.3. PREDICTION OF THE EXTREME OVERTOPPING WAVE FORCE DURING A KNOWN STORM PEAK

Wave overtopping is stochastic process. Thus, a statistical description of forces is needed in order to develop a practical approach to design and assess structures. Although there is plenty of work about the statistical characteristics of the overtopping volumes, overtopping flow thickness and velocities, few sources are related to the overtopping forces. As a continuation study of Chapter 3, the maximum overtopping force during a given storm was particularly determined in Chapter 4.

Statistical analysis of the overtopping forces on a vertical wall was conducted via a series of physical model tests with irregular waves. The General Pareto (GP) distribution was found a suitable fit among commonly used distributions for the extreme forces. The three parameters of the GP distribution were empirically determined by using incident wave characteristics and dike geometry parameters. An approach with a 7-step procedure for predicting the maximum force was proposed, which shows an overall satisfactory performance. The limitation of this work was the range of the physical model tests, which were conducted with one dike slope (1:3), one foreshore slope (1:35), and two dike crest widths: $B = 0.5$ m for most of the tests, and $B = 0.25$ m for only two tests. The influence of foreshore slope and dike slope on the wave dynamics and overtopping process were not considered in this study, but similar waves are expected for other gentle foreshore with similar depth at the toe.

6.1.4. VULNERABILITY OF BUILDINGS ON COASTAL DIKES

In chapter 5, two main simplified failure mechanisms of masonry buildings on a Belgian coastal dike were considered as a case study. One is the collapse of the structural wall like an external load-bearing wall or stability wall, and the other one is localized damage of non-structural components like non-load-bearing wall and glass windows.

The vulnerability of the masonry walls and glass windows against overtopping wave impact was assessed under three scenarios, including two storm surges with return periods of 1000 (S1) and 10,000 years (S2) and one 10,000 years storm surge with a low beach level (S3). The impact load was estimated by using the approach developed in Chapter 4. The overall results indicated that the chance of collapse of the masonry buildings on the dike is low under scenarios S1 and S2. But the non-structural external wall and glass windows are expected to break, which would lead to the inundation of the ground floor of the buildings. However, most of the key external structural walls are expected to fail when the buildings are located near the coast under scenario S3 (i.e. 10,000 year conditions with less shallow foreshores). Thus, it is recommended to increasing the strength of the external masonry wall on the ground, and reinforcing windows to avoid inundation.

This assessment approach was developed specifically for the masonry buildings on a coastal dike with shallow water conditions. The existing masonry design code and empirical overtopping wave load were applied to set the limit state function of bending failure. Thus the applicable range of the hydraulic conditions of the empirical overtopping wave load formula needs to be checked.

6.2. RECOMMENDATIONS

This section gives a few recommendations and outlook.

6.2.1. IMPACT MECHANISMS

For future studies, a detailed classification of the impact mechanisms due to different interaction patterns of overtopping waves is suggested, which will help to predict the occurrences of the impulsive wave impact. In order to achieve this goal, a physical model experiment with a highly repeatable wave generation method to simulate the interaction is recommended. Moreover, a detailed estimation of the fraction of the overtopping waves that contribute to the impact force is suggested, which will connect the numerous research work of overtopping volumes to the overtopping wave impact forces. It is suggested to investigate the pressure distribution and its influence on the building elements located at high elevation and overturning moments are suggested to be investigated in detail.

6.2.2. IMPACT FORCE OF A SINGLE OVERTOPPING WAVE

In order to interpret the overtopping process of the incident wave from dike toe up to the front of a wall on a dike, it is recommended to investigate long waves and their effect on overtopping.

6.2.3. PREDICTION OF THE EXTREME OVERTOPPING WAVE FORCE

It is suggested to widen the range of the wave conditions and the dike crest width. Numerical modeling is recommended to be carried out to investigate the influence of the foreshore slope and dike slope on wave dynamics and overtopping in a shallow water environment.

6.2.4. VULNERABILITY OF BUILDINGS

The collapse of a building is not something that can be predicted with a 100% certainty. It is recommended to apply a probabilistic approach to predict the probability of failure of buidlings on coastal dikes during their life span. Moreover, it is recommended to derive criteria for acceptable risk for these types of situations. The question which chance of collapse or localized damage is acceptable has to be answered by the various stakeholders such as the owner, the government and other people whose life is in some way influenced by a possible failures. Arguments can be social, economic or otherwise. For buildings that appear to be in dangerous conditions, it is recommended to increase the strength of the external wall on the ground by providing extra supports, and reinforce the windows when designing a building on the dike. It appeared that the elevation of the beach and foreshore in front of the dike are important determinants of the loads on

the building. Thus more effort should be put on the influence of beach profiles on wave overtopping in the future. Beach nourishments can be considered in areas where risks are high. The approach presented in this study can be extended with a strength model for other structure types, such as concrete buildings. Based on the findings of the case, it is suggested to evaluate the risk of building collapse and associated risk for people living in the Belgian and Dutch coast.

6.2.5. OUTLOOK

The work documented in this thesis has resulted in understanding of the impact force generation mechanism of overtopping waves in order to develop a practical approach to assessing the vulnerability of buildings on a coastal dike. Data from physical model experiments by using different types of waves were used, including regular waves, bichromatic waves, and irregular waves. Problems that are typical for physical model tests, such as scale effect and model effect, were addressed. Limitations of the application of the proposed empirical formulas were also stated.

There are some expectations about the physical model experiments for future studies. Large scale model tests are always recommended to deal with scale effect. However it is very costly (but possible) to conduct wave overtopping tests for a long duration in a large scale facility. Thus, a highly repeatable test which can generate the correct overtopping wave is more recommended for the full scale study of overtopping wave impact. Besides the challenge of wave generation, low spatial resolution of pressure sensors limits the measurement of the wave impact load. With the development of visualization technique, non-instrumental 2-D and 3-D velocity field measurement for turbulent flow (e.g., Song et al., 2015) is highly suggested for the instantaneous spatial pressure distribution measurement in the future (e.g., Liu and Katz, 2006; Knopp et al., 2015; Schneiders et al., 2016) at large scale experiments.

For the purpose of developing formulae for overtopping impact loads on structures, using small scale model experiments and numerical model simulations are recommended in the future study. The usage of small scale model experiments should provide a detailed measurement of water surface elevations, overtopping layer thickness, velocity field of the overtopping flow and more parameters, in order to validate numerical models. A non-hydrostatic model such as SWASH (which has reached a rather mature state to include low-frequency wave breaking in a shallow water environment, see Rijnsdorp et al., 2014) is recommended to extend the current work by widening the test range, such as changing the foreshore slope. Details about the outlook of non-hydrostatic models can be found in Smit (2014).

Currently, the widely used design approaches for coastal structures dealing with wave impact choose the impact load as the design criterion. Structures with different eigenfrequencies would react differently when subjected to an impulsive impact load. Sometimes this different structural response would create a gap between a coastal engineer who will provide wave load data and structural engineer who will design a structure. Thus, the impulse is recommended to replace the impulsive impact load into a new design formula, which is relatively constant, containing the information of the impact load magnitude and impact duration (Peregrine, 2003). Then, when the impulse induced by the wave impact and the natural frequency of a specific structure are known, the desired

impact load can be estimated.

As one of the projects of the MFFD program, this study is associated with the task of hydraulic impact of overtopping waves on a multifunctional dike with a specific case of a building on the top. Only the wave impact load, and the vulnerability of the existing buildings due to the impact were investigated. The question what chance of collapse or localized damage of a building on a MFFD is acceptable has to be answered by the various stakeholders such as the owner, the government and other people whose life is in some way influenced by a possible failures. Arguments can be social, economic or otherwise and the content and the weight of each argument can differ in time.

NOMENCLATURE

Acronyms

AIC	Akaike Information Criteria	
BIC	Bayesian Information Criteria	
BIV	Bubble Image Velocimetry	
FOV	Field of view	
GEV	Generalised Extreme Value	
GP	Generalized Pareto	
ML	Maximum Likelihood	
RMSE	Square root of the variance of the residuals	

Greek Symbols

β	Seaward dike slope	°
Δp_{max}	Maximum pressure difference	N/m^2
Δt	Wave impact duration	s
$\eta(x)$	Sea surface elevation at location x	m
$\eta(x)$	Sea surface elevation at location x	m
γ, γ_s	Specific weight of water and slab	KN/m^3
γ_f	Safety factor for load (load factor)	-
γ_M	Safety factor for material (material factor)	-
μ	Fraction of a wave impact zone	-
Ω	Dimensionless reduction factor	-
ρ	Fluid density	kg/m^3
σ	Scale parameter of a Generalized Pareto distribution	N/m
θ	An angle between the run-up water surface and the still water level	°

θ_0	Incident water wedge angle	°
ξ_0	Iribarren number	-

Roman Symbols

B	Boulevard width or the distance between the wall and the dike transition line	m
C_F	Empirical force coefficient	-
C_p	Pressure coefficient, which equals to $\Delta p_{max}/(\gamma \cdot V_j^2/2g)$	-
D	Duration of a storm peak (test duration)	s
d_0	Maximum initial overtopping wave depth at x_{tr}	m
d_x	Maximum overtopping wave depth at a specific location x along the dike crest	m
d_{A0}	Unobstructed overtopping flow depth near x_{tr} at the dike crest	m
d_{B0}	Obstructed overtopping flow depth near x_{tr} at the dike crest	m
F_h	Wave impact horizontal force peak	N/m
F_{dy}	Dynamic force peak	N/m
F_{pdy}	Dynamic impact force obtained from the integration of pressure records along the wall	N/m
F_{pqs+}	Maximum hydro quasi-static force obtained from the integration of pressure records	N/m
F_{qs+}	Quasi-static force peak	N/m
F_u	Threshold of a Generalized Pareto distribution	N/m
H	Distance from the sea bed to the wave crest	m
h	Water level at the wall location	m
h_r	Measured maximum run-up height	m
h_t	Water depth at the toe of the dike	m
$H_{m0,o}$	Offshore wave height	m
$H_{m0,t}$, $H_{m0,toe}$	Incident spectrum wave height at the toe of the dike	m

H_{m0}	spectrum wave heigh	m
k	Shape parameter of a Generalized Pareto distribution	-
L_t	Calculated wave length in a shallow water condition by $T_{m-1,0,t}\sqrt{gh_t}$	m
M_R	Lateral resistance capacity	KN m/m
M_S	Design moment of the lateral load	KN m/m
M_F	Maximum depth-integrated wave momentum flux per unit of width at a specific moment	N/m
N_{toe}	Representative incident wave number at the toe	-
p_d	Instantaneous wave force (or dynamic pressure) on the wall	N/m^2
P_i	Overtopping impact probability	-
P_z	Pressure-impulse	N/m^{2}s
P_{im}	Overtopping impact probability for the extreme large impacts (10% of P_i)	-
P_{max}	Probability of the maximum overtopping wave impact load	-
p_{pk}	Impact pressure	N/m^2
q_k	Characteristic uniform distributed load	KN/m^2
q_{avg}	Averaged hydro-static pressure	KN/m^2
$q_{w,max}$	Maximum hydro-static pressure	KN/m^2
$q_{w,min}$	Minimum hydro-static pressure	KN/m^2
R_c	Distance between the dike crest level to still water level (or freeboard)	m
R_u	Fictitious maximum wave run-up height	m
s	Equivalent slab thickness	m
T	Wave period at the toe of the dike	s
$T_{m-1,0,t}$	Incident spectrum wave period at the toe of the dike	s
$T_{m-1,0}$	spectrum wave period	s

u	Incoming flow velocity	m/s
U_0	Wave impact velocity	m/s
V_j	Vertical jet velocity	m/s
x	Horizontal coordinate	m
x_{tr}	Transition line between the seaward slope and the dike crest	m
z	Vertical coordinate	m
Z_a	Equivalent overtopping run-up height	m
c	circle of confusion	m
f	focal length	mm
N	focal length number	-

BIBLIOGRAPHY

Aerts, J.C.J.H., Botzen, W.J.W., 2011. Flood-resilient waterfront development in New York City: bridging flood insurance, building codes, and flood zoning. Annals of the New York Academy of Sciences 1227, 1–82.

Akaike, H., 1973. Information theory and an extension of the maximum likelihood principle, in: 2nd International Symposium on Information Theory, Budapest. pp. 167–281.

Allsop, W., Bruce, T., Pullen, T., Van der Meer, J., 2008. Direct hazards from wave overtopping - the forgotten aspect of coastal flood risk assessment?, in: 43rd Defra Flood and Coastal Management Conference.

Allsop, W., Franco, L., Bellotti, G., Bruce, T., Geeraerts, J., 2005. Hazards to people and property from wave overtopping at coastal structures, in: Allsop, W. (Ed.), Coastlines, Structures and Breakwaters 2005, Thomas Telford, London. pp. 153–165.

Altomare, C., Crespo, A., Rogers, B., Dominguez, J., Gironella, X., Gómez-Gesteira, M., 2014. Numerical modelling of armour block sea breakwater with smoothed particle hydrodynamics. Computers & Structures 130, 34–45.

Anvarifara, F., Zevenbergen, C., Thissen, W., Islam, T., 2016. Understanding flexibility for multifunctional flood defences: a conceptual framework. Journal of Water and Climate Change , jwc2016064

Archetti, R., Brocchini, M., 2002. An integral swash zone model with friction: an experimental and numerical investigation. Coastal Engineering 45, 89–110.

Arikawa, T., 2008. Behaviors Of Concrete Walls Under Impulsive Tsunami Load. AGU Fall Meeting Abstracts -1, 1331.

Ariyarathne, K., Chang, K.A., Mercier, R., 2012. Green water impact pressure on a three-dimensional model structure. Experiments in Fluids 53, 1879–1894.

Arnason, H., 2005. Interactions between an Incident Bore and A Free-Standing Coastal Structure. Ph.D. thesis. University of Washington.

Arnason, H., Petroff, C., Yeh, H., 2009. Tsunami Bore Impingement onto a Vertical Column. Journal of Disaster Research 4.

Battjes, J., 1974. Surf similarity, in: Coastal Engineering Proceedings.

Bollaert, E.F.R., Schleiss, A.J., 2005. Physically Based Model for Evaluation of Rock Scour due to High-Velocity Jet Impact. Journal of Hydraulic Engineering 131, 153–165.

British Standards Institution, 1996. BS EN 1996: Eurocode 6- Design of masonry structures.

Brodtkorb, P.A., Johannesson, P., Lindgren, G., Rychlik, I., Rydén, J., Sjö, E., 2000. WAFO-a Matlab Toolbox for the Analysis of Random Waves and Loads, in: Proc. 10'th Int. Offshore and Polar Eng. Conf., ISOPE, Seattle, USA, pp. 343–350.

Bullock, G., Crawford, A., Hewson, P., Walkden, M., Bird, P., 2001. The influence of air and scale on wave impact pressures. Coastal Engineering 42, 291–312.

Caires, S., van Gent, M.R.A., 2008. Extreme Wave Loads, in: Volume 2: Structures, Safety and Reliability, ASME. pp. 945–953.

Cam, L.L., Yang, G.L., 2000. Asymptotics in Statistics: Some Basic Concepts. Springer Science & Business Media.

Chan, E.S., Melville, W.K., 1988. Deep-Water Plunging Wave Pressures on a Vertical Plane Wall. Proceedings of the Royal Society A: Mathematical, Physical and Engineering Sciences 417, 95–131.

Chen, X., Hassan, W., Uijttewaal, W., Verwaest, T., Verhagen, H.J., Suzuki, T., Jonkman, S.N., 2012. Hydrodynamic load on the building caused by overtopping waves. Coastal Engineering Proceedings 1, structures.59.

Chen, X., Hofland, B., Altomare, C., Suzuki, T., Uijttewaal, W., 2014. Experimental study on overtopping flow loads, in: Coastal Engineering Proceedings, pp. 1(34), structures.4.

Chen, X., Hofland, B., Altomare, C., Suzuki, T., Uijttewaal, W., 2015. Forces on a vertical wall on a dike crest due to overtopping flow. Coastal Engineering 95, 94–104.

Chen, X., Hofland, B., Uijttewaal, W., 2016. Maximum overtopping forces on a dike-mounted wall with a shallow foreshore. Coastal Engineering 116, 89–102.

Chock, G., Robertson, I., Carden, L., Yu, G., 2012. Tohoku tsunami-induced building damage analysis including the contribution of earthquake resistant design to tsunami resilience of multi-story buildings. Proceedings of the International Symposium on Engineering Lessons Learned from the 2011 Great East Japan Earthquake, 492–503.

Coles, S., 2001. An Introduction to Statistical Modeling of Extreme Values. Springer Science & Business Media.

Cooker, M., Peregrine, D., 1990. A model for breaking wave impact pressures, in: Coastal Engineering Proceedings.

Cooker, M.J., Peregrine, D.H., 1995. Pressure-impulse theory for liquid impact problems. Journal of Fluid Mechanics 297, 193.

Cox, J.C., Machemehl, J., 1986. Overload Bore Propagation Due to an Overtopping Wave. Journal of Waterway, Port, Coastal and Ocean Engineering 112, 161–163.

Cross, R., 1967. Tsunami surge forces. Journal of the Waterways and Harbors Division .

Cumberbatch, E., 1960. The impact of a water wedge on a wall. Journal of Fluid Mechanics 7, 353– 374.

Cuomo, G., Allsop, W., Bruce, T., Pearson, J., 2010a. Breaking wave loads at vertical seawalls and breakwaters. Coastal Engineering 57, 424–439.

Cuomo, G., Allsop, W., Takahashi, S., 2010b. Scaling wave impact pressures on vertical walls. Coastal Engineering 57, 604–609.

Cuomo, G., Piscopia, R., Allsop, W., 2011. Evaluation of wave impact loads on caisson breakwaters based on joint probability of impact maxima and rise times. Coastal Engineering 58, 9–27.

De Rouck, J., Van Doorslaer, K., Versluys, T., Ramachandran, K., Schimmels, S., Kudella, M., Trouw, K., 2012. Full scale impact tests of an overtopping bore on a vertical wall in the large wave flume (GWK) in Hannover, in: Coastal Engineering Proceedings, p. structures.62.

De Sortis, A., Antonacci, E., Vestroni, F., 2005. Dynamic identification of a masonry building using forced vibration tests. Engineering Structures 27, 155–165.

Duell, M., Thomas, E., 2014. Aren't they listening? Thrill-seekers risk their lives to take pictures of high tides and crashing waves despite police pleas to stay away from the seafront.

Erikson, L., Larson, M., Hanson, H., 2005. Prediction of swash motion and run-up including the effects of swash interaction. Coastal Engineering 52, 285–302.

FEMA P-55, 2011. Coastal Construction Manual: Principles aand Practices of Planning, Siting, Designing, Constructing, and Maintaining Residential Buildings in Coastal Areas (FEMA P-55). 4th ed., FEMA.

Ferrario, F., Beck, M.W., Storlazzi, C.D., Micheli, F., Shepard, C.C., Airoldi, L., 2014. The effectiveness of coral reefs for coastal hazard risk reduction and adaptation. Nature communications 5, 3794.

Fiorotto, V., Rinaldo, A., 1992. Fluctuating Uplift and Lining Design in Spillway Stilling Basins. Journal of Hydraulic Engineering 118, 578–596.

Fuchs, H., 2013. Solitary Impulse Wave Run-up and Overland Flow. Ph.D. thesis. ETH Zürich.

Goda, Y., 2010. Random Seas and Design of Maritime Structures.

Hamdi, Y., Bardet, L., Duluc, C.M., Rebour, V., 2013. Extreme storm surges: a comparative study of frequency analysis approaches. Natural Hazards and Earth System Sciences Discussions 1, 6619–6658.

Hamilton, D.G., Hall, K.R., 1992. Preliminary analysis of the stability of rubble mound breakwater crown walls, in: Coastal Engineering Proceedings.

Hatzikyriakou, A., Lin, N., Gong, J., Xian, S., Hu, X., Kennedy, A., 2015. Component-Based Vulnerability Analysis for Residential Structures Subjected to Storm Surge Impact from Hurricane Sandy. Natural Hazards Review , 05015005

Hughes, S., Nadal, N., 2009. Laboratory study of combined wave overtopping and storm surge overflow of a levee. Coastal Engineering 56, 244–259.

Hughes, S.a., 2004a. Estimation of wave run-up on smooth, impermeable slopes using the wave momentum flux parameter. Coastal Engineering 51, 1085–1104.

Hughes, S.a., 2004b. Wave momentum flux parameter: a descriptor for nearshore waves. Coastal Engineering 51, 1067–1084.

Hughes, S.A., Thornton, C.I., Van der Meer, J.W., Scholl, B.N., 2012. Improvements in describing wave overtopping processes. Coastal Engineering Proceedings 1, waves.35.

Hunt, I., 1959. Design of seawalls and breakwaters. Journal of Waterways and Harbours Division 85, 123 – 152.

Kamikubo, K., Yamamoto, Y., Sugawara, K., Kimura, K., Shimizu, T., 2009. Experimental Study on Damage to Wave Splash Barrier for a Coastal Road. Journal of Japan Society of Civil Engineers, Ser. B 2(Coastal Engineering) 65, 821–825.

Kelman, I., 2002. Physical Flood Vulnerability of Residential Properties in Coastal , Eastern England. Ph.D. thesis. University of Cambridge.

Kelman, I., Spence, R., 2004. An overview of flood actions on buildings. Engineering Geology 73, 297–309.

Kisacik, D., Troch, P., Van Bogaert, P., 2012. Experimental study of violent wave impact on a vertical structure with an overhanging horizontal cantilever slab. Ocean Engineering 49, 1–15.

Knopp, T., Buchmann, N., Schanz, D., Eisfeld, B., Cierpka, C., Hain, R., Schröder, A., Kähler, C., 2015. Investigation of scaling laws in a turbulent boundary layer flow with adverse pressure gradient using PIV. Journal of Turbulence .

Kortenhaus, A., Oumeraci, H., 1998. Classification of wave loading on monolithic coastal structures, in: Coastal Engineering Proceedings.

Ligtvoet, W., Knoop, J., Strengers, B., Bouwman, A., 2009. Flood protection in the Netherlands: framing long-term challenges and options for a climate-resilient delta. Technical Report. Policy studies, Netherlands Environmental Assessment Agency. Dordrecht.

Lin, C., Hsieh, S.C., Lin, I.J., Chang, K.A., Raikar, R.V., 2012. Flow property and self-similarity in steady hydraulic jumps. Experiments in Fluids 53, 1591–1616.

Liu, X., Katz, J., 2006. Instantaneous pressure and material acceleration measurements using a four-exposure PIV system. Experiments in Fluids 41, 227–240.

van Loon-Steensma, J.M., Vellinga, P., 2014. Robust, multifunctional flood defenses in the Dutch rural riverine area. Natural Hazards and Earth System Science 14, 1085–1098.

Lugni, C., Brocchini, M., Faltinsen, O.M., 2006. Wave impact loads: The role of the flip-through. Physics of Fluids 18, 122101.

Martin, F.L., Losada, M.a., Medina, R., 1999. Wave loads on rubble mound breakwater crown walls. Coastal Engineering 37, 149–174.

Matsutomi, H., Okamoto, K., 2010. Inundation flow velocity of tsunami on land. Island Arc 19, 443–457.

Mazas, F., Hamm, L., 2011. A multi-distribution approach to POT methods for determining extreme wave heights. Coastal Engineering 58, 385–394.

McGranahan, G., Balk, D., Anderson, B., 2007. The rising tide: assessing the risks of climate change and human settlements in low elevation coastal zones. Environment and Urbanization 19, 17–37.

Méndez, F.J., Menéndez, M., Luceño, A., Losada, I.J., 2006. Estimation of the long-term variability of extreme significant wave height using a time-dependent Peak Over Threshold (POT) model. Journal of Geophysical Research 111, C07024.

Moore, J., 2008. Manual for the Design of Plain Masonry in Building Structures to Eurocode 6. Institution of Structural Engineers.

Nicholls, R.J., 2004. Coastal flooding and wetland loss in the 21st century: changes under the SRES climate and socio-economic scenarios. Global Environmental Change 14, 69–86.

Nistor, I., Palermo, D., Nouri, Y., Murty, T., 2009. Tsunami-Induced Forces on Structures .

Nørgaard, J.Q.H., Andersen, T.L., 2014. Distribution of wave loads for design of crown walls in deep and shallow water, in: Coastal Engineering Proceedings, p. 47.

Nørgaard, J.Q.H., Andersen, T.L., Burcharth, H.F., 2013. Wave loads on rubble mound breakwater crown walls in deep and shallow water wave conditions. Coastal Engineering 80, 137–147.

Nørgaard, J.Q.H., Lykke Andersen, T., Burcharth, H.F., 2014. Distribution of individual wave overtopping volumes in shallow water wave conditions. Coastal Engineering 83, 15–23.

Nouri, Y., Nistor, I., Palermo, D., Cornett, A., 2010. Experimental Investigation of Tsunami Impact on Free Standing Structures. Coastal Engineering Journal 52, 43–70.

Ottesen-Hansen, N., Sand, S.E., Lundgren, H., Sorensen, T., Gravesen, H., 1980. Correct reproduction of group-induced long waves, in: Coastal Engineering Proceedings.

Oumeraci, H., Klammer, P., Partenscky, H., 1993. Classification of breaking wave loads on vertical structures. Journal of Waterway, Port, Coastal, and Ocean Engineering 119, 381–397.

Oumeraci, H., Kortenhaus, A., Allsop, W., de Groot, M., Crouch, R., Vrijling, H., Voortman, H., 2001. Probabilistic Design Tools for Vertical Breakwaters.

Pan, Y., Kuang, C., Li, L., Amini, F., 2015. Full-scale laboratory study on distribution of individual wave overtopping volumes over a levee under negative freeboard. Coastal Engineering 97, 11–20.

Pedersen, J., 1996. Wave Forces and Overtopping on Crown Walls of Rubble Mound Breakwaters. Ph.D. thesis. Aalborg University, Denmark.

Pedrozo-Acuña, A., de Alegría-Arzaburu, A.R., Torres-Freyermuth, A., Mendoza, E., Silva, R., 2011. Laboratory investigation of pressure gradients induced by plunging breakers. Coastal Engineering 58, 722–738.

Peregrine, D.H., 2003. Water-wave impact on walls. Annual Review of Fluid Mechanics 35, 23–43.

Peregrine, D.H., Williams, S.M., 2001. Swash overtopping a truncated plane beach. Journal of Fluid Mechanics 440, 391–399.

Pickands III, J., 1975. Statistical Inference Using Extreme Order Statistics. The Annals of Statistics 3, 119–131.

Pistrika, A.K., Jonkman, S.N., 2010. Damage to residential buildings due to flooding of New Orleans after hurricane Katrina. Natural Hazards 54, 413–434.

Pullen, T., Allsop, N., Bruce, T., 2007. EurOtop Wave Overtopping of Sea Defences and Related Structures .

Quataert, E., Storlazzi, C., van Rooijen, A., Cheriton, O., van Dongeren, A., 2015. The influence of coral reefs and climate change on wave-driven flooding of tropical coastlines. Geophysical Research Letters , n/a–n/a

Ramachandran, K., Genzalez, R.R., Oumeraci, H., Schimmels, S., Kudella, M., Van Doorslaer, K., De Rouck, J., Versluys, T., Trouw, K., 2012. Loading of vertical walls by overtopping bores using pressure and force sensors - a large scale model study, in: Coastal Engineering Proceedings, p. currents.44.

Ramsden, J.D., 1996. Forces on a Vertical Wall due to Long Waves, Bores, and Dry-Bed Surges. J. Waterway, Port, Coastal, Ocean Eng 122, 134–141.

Rijnsdorp, D.P., Smit, P.B., Zijlema, M., 2014. Non-hydrostatic modelling of infragravity waves under laboratory conditions. Coastal Engineering 85, 30–42.

Robert, J., Brooker, O., 2007. How to design masonry structures to Eurocode 6: Lateral resistance. MPA The Concrete Centre.

Robertson, I.N., 2011. Tsunami bore forces on walls, in: International conference on ocean, offshore and artic engineering (OMAE), Rotterdan. pp. 1–9.

Roeber, V., Bricker, J.D., 2015. Destructive tsunami-like wave generated by surf beat over a coral reef during Typhoon Haiyan. Nature communications 6, 7854.

Romano, A., Bellotti, G., Briganti, R., Franco, L., 2015. Uncertainties in the physical modelling of the wave overtopping over a rubble mound breakwater: The role of the seeding number and of the test duration. Coastal Engineering 103, 15–21.

Ryu, Y., Chang, K.A., Lim, H.J., 2005. Use of bubble image velocimetry for measurement of plunging wave impinging on structure and associated greenwater. Measurement Science and Technology 16, 1945–1953.

Ryu, Y., Chang, K.A., Mercier, R., 2007. Application of dam-break flow to green water prediction. Applied Ocean Research 29, 128–136.

Saville, T., 1962. An approximation of the wave run-up frequency distribution, in: Coastal Engineering Proceedings, p. 4.

Schneiders, J., Caridi, G.C.A., Sciacchitano, A., Scarano, F., 2016. Instantaneous Pressure Measurements from Large-Scale Tomo-PTV with HFSB Tracers past a Surface-Mounted Finite Cylinder, in: 54th AIAA Aerospace Sciences Meeting, p. 1048.

Schüttrumpf, H., 2001. Wellenüberlaufströmung bei Seedeichen-Experimentelle und theoretische Untersuchungen. Dissertation. Technischen Universität Braunschweig.

Schüttrumpf, H., Oumeraci, H., 2005. Layer thicknesses and velocities of wave overtopping flow at seadikes. Coastal Engineering 52, 473–495.

Schwarz, G., 1978. Estimating the Dimension of a Model. The Annals of Statistics 6, pp. 461–464.

Shah, A.M., Kamphuis, J.W., 1996. The swash zone: a focus on low frequency motion, in: Coastal Engineering Proceedings.

Shimozono, T., Tajima, Y., Kennedy, A.B., Nobuoka, H., Sasaki, J., Sato, S., 2015. Combined infragravity wave and sea-swell runup over fringing reefs by super typhoon Haiyan. Journal of Geophysical Research: Oceans 120, n/a–n/a.

Smit, P., 2014. Deterministic and Stochastic Modelling of Ocean Surface Waves.

Solari, S., Losada, M.Á., 2012. Unified distribution models for met-ocean variables: Application to series of significant wave height. Coastal Engineering 68, 67–77.

Song, Y.K., Chang, K.A., Ariyarathne, K., Mercier, R., 2015. Surface velocity and impact pressure of green water flow on a fixed model structure in a large wave basin. Ocean Engineering 104, 40–51.

Song, Y.K., Chang, K.A., Ryu, Y., Kwon, S.H., 2013. Experimental study on flow kinematics and impact pressure in liquid sloshing. Experiments in Fluids 54, 1592.

Stalenberg, B., 2010. Design of floodproof urban riverfronts. Ph.D. thesis. Delft University of Technology.

Steenbergen, R., Vrouwenvelder, A., 2010. Safety philosophy for existing structures and partial factors for traffic loads on bridges. Heron, Oktober, 2, 55, 18 .

Suzuki, T., De Roo, S., Altomare, C., Zhao, G., Kolokythas, G., Willems, M., Verwaest, T., Mostaert, F., 2015. Toetsing kustveiligheid-2015 - Methodologie: Toetsingsmethodologie voor dijken en duinen (Version 6.0). Technical Report. Waterbouwkundig Laboratorium & Afdeling Kust. Antwerpen, België.

Suzuki, T., Verwaest, T., Veale, W., Trouw, K., Zijlema, M., 2012. A numerical study on the effect of beach nourishment on wave overtopping in shallow foreshores, in: Coastal Engineering Proceedings, p. waves.50.

Thielicke, W., Stamhuis, E.J., 2014. PIVlab – Towards User-friendly, Affordable and Accurate Digital Particle Image Velocimetry in MATLAB. Journal of Open Research Software 2.

Van der Meer, J.W., Hardeman, B., Steendam, G.J., Schuttrumpf, H., Verheij, H., 2010. Flow depths and velocities at crest and landward slope of a dike, in theory and with the wave overtopping simulator. Coastal Engineering Proceedings 1, structures.10.

Van der Meer, J.W., Janssen, W., 1995. Wave run-up and wave overtopping at dikes, in: Kabayashi, Demirbilek (Eds.), Wave forces on inclined and vertical wall structures. American Society of Civil Engineers, pp. 1–27.

Van Dongeren, A., Battjes, J., Janssen, T., van Noorloos, J., Steenhauer, K., Steenbergen, G., Reniers, A., 2007. Shoaling and shoreline dissipation of low-frequency waves. Journal of Geophysical Research 112, C02011.

Van Doorslaer, K., De Rouck, J., Audenaert, S., Duquet, V., 2015. Crest modifications to reduce wave overtopping of non-breaking waves over a smooth dike slope. Coastal Engineering

Van Doorslaer, K., De Rouck, J., Trouw, K., van der Meer, J., Schimmels, S., 2012. Wave forces on storm walls, small and large scale experiments.

Van Gent, M., 1999. Physical model investigations on coastal structures with shallow foreshores: 2D model tests with single and double-peaked wave energy spectra. Technical Report. Deltares.

Van Gent, M.R., 2002. Wave overtopping events at dikes, in: Coastal Engineering Proceedings.

Van Gent, M.R.A., 2001. Wave Runup on Dikes with Shallow Foreshores. Journal of Waterway, Port, Coastal, and Ocean Engineering 127, 254–262.

Verwaest, T., Vanpoucke, P., Willems, M., De Mulder, T., 2010. Waves overtopping a wide-crested dike, in: Coastal Engineering Proceedings, p. 7.

Victor, L., van der Meer, J., Troch, P., 2012. Probability distribution of individual wave overtopping volumes for smooth impermeable steep slopes with low crest freeboards. Coastal Engineering 64, 87–101.

Vrouwenvelder, A., 2005. Eurocode 1, part 1.7 Accidental Actions, Background Document.

Yamamoto, Y., Horikawa, K., 1992. New methods to evaluate wave run-up height and wave overtopping rate, in: Coastal Engineering Proceedings.

Zanuttigh, B., Van der Meer, J.W., Bruce, T., Hughes, S.A., 2013. Statistical characterisation of extreme overtopping wave volumes, in: Coasts, Marine Structures and Breakwaters, Edinburgh.

ACKNOWLEDGEMENTS

After spending six years at the Delft University of Technology, the time has finally come to finalise my studies. While writing these acknowledgements, I can't help looking back in time, which has made me realise that I have really enjoyed these last four years of research. During this period, I have shared my time with a great deal of people that in many ways have contributed to this thesis and my life in general. Without their kind support and help, this thesis wouldn't have been possible.

Naturally, this thesis would not have been completed without the aid and support of my supervisors: Wim Uijttewaal, Bas Jonkman, and Bas Hofland. First of all, Wim, thank you for initiating the STW project and granting me the opportunity to start my academic endeavours. I am grateful to you for trusting me with the freedom to find my own way in the world of physical model experiments. Ever since I started modelling wave impacts on buildings as a part of my MSc thesis, Bas Jonkman has been there. Thank you for supporting and pushing me always that one step further over these years. Without any doubt, Bas Hofland is the person who contributed most to this thesis. At the beginning you were only involved in my work as an adviser from Deltares, but I am so grateful that you could be one of the official supervisors of my PhD work at the end. Thanks for your guidance, encouragement and support which have been most valuable and unforgettable. I feel that the students of Hydraulic Engineering are so lucky to have you because of your inspiring passion for engineering and research at TU Delft.

Besides my supervisors, I have had the honour of collaborating with Dr. Tomohiro Suzuki and Dr. Corrado Altomare. Your suggestions and work have contributed a lot to the papers that we have written together and which comprise of much of this thesis. Also thanks to my co-author Sander Pasterkamp for help with Chapter 5. I greatly appreciate the support of the staff of the Fluid Mechanics section and the laboratory of Flanders Hydraulic Research Institute. Furthermore, I am grateful for the assistance and help of the supporting staff, especially Otti and Mariette.

I also like to take the opportunity to thank my colleagues. I have enjoyed all the lunches, coffee breaks, drinks and the dinners that we have shared together; be it either in Delft or away on a conference. First of all, the people from the 2nd floor deserve some special attention. Adam, Dirk, James, Marion, Melike, Nils, Sotiria, Steffie and Sabine, thanks for being such great colleagues. Thanks also, Astrid, Andres, Cynthia, Victor, and all others that have crossed my path. Thank you all for the great times that we have shared at our department.

Besides all the people at university, a lot of others have helped me in one way or another to finish this piece of work. They provided a great distraction from the daily realms of work. Thanks Tomo, Corrado, Tim, Sebastian, Yair, and your families. I have quite enjoyed our traditional group birthday parties in Belgium over the past six years. I would like to also thank Huifei, Jinglang, Wei, Yao and Ying for your support in my Ph.D. life. Xiaoyan, without you, I would never know how strong a girl should be. Thanks

for the company and tolerance my emotional flooding in front of you during my tough times.

Finally, I would like to give my deepest gratitude to my parents for all their love, support and unwavering belief in me during all the time I have been living far away from them.

Xuexue Chen
Delft, September 2016

LIST OF PUBLICATIONS

Chen, X., Hofland, B., Uijttewaal, W., 2016. Maximum overtopping forces on a dike-mounted wall with a shallow foreshore. *Coastal Engineering*, 116, 89-102.

Chen, X., Jonkman, S.N., Pasterkamp, S., Suzuki, T., Altomare, C., 2016. Vulnerability of coastal buildings due to wave overtopping. *Journal of Waterway, Port, Coastal, and Ocean Engineering* (submitted).

Chen, X., Hofland, B., Altomare, C., Suzuki, T., Uijttewaal, W., 2015. Forces on a vertical wall on a dike crest due to overtopping flow. *Coastal Engineering*, 95, 94–104.

Altomare, C., Suzuki, T., **Chen, X.**, Verwaest, T., Kortenhaus, A., 2016. Wave overtopping of sea dikes with very shallow foreshores, *Coastal Engineering*, 116, 236-257.

Hofland, B., **Chen, X.**, Altomare, C., Oosterlo, P., 2016. Prediction formula for the spectral wave period Tm-1,0 on mild-sloping shallow foreshores. *Coastal Engineering* (submitted).

Chen, X., Hofland, B., Altomare, C., Uijttewaal, W., 2014. Overtopping flow impact on a vertical wall on a dike crest. *Proceedings of 34th International Conference on Coastal Engineering*, Seoul, Korea, 2014.

Chen, X., Uijttewaal, W., Jonkman, SN., Verwaest, T., 2012. Hydrodynamic load on buildings caused by overtopping wave. *Coastlab 2012*, Ghent, Belgium.

Chen, X., Hassan, W., Uijttewaal, W., Verwaest, T., Verhagen, HJ., Suzuki, T., Jonkman, SN., 2012. Hydrodynamic loads on buildings caused by overtopping wave. *Proceedings of 33th International Conference on Coastal Engineering*, Santander, Spain, 2012.

Curriculum Vitæ

Xuexue Chen was born on 14 January 1985. She graduated in 2004 at the Jinzhou middle school in Jinzhou. After that she started her academic education in Civil Engineering in Sichuan University. In 2009, she moved to Europe for her master courses in Coastal and Marine Engineering and Management (CoMEM) with an Erasmus Mundus scholarship. Following the completion of her MSc study, she started as a PhD student at the section of Environmental Fluid Mechanics of the Delft University of Technology in November 2011. After finishing her doctoral study in 2016, she is working as a post-doctoral researcher at the section of Hydraulic Structures and Flood Risk in the same university.